Study of Time-dependent CP Violation in $B^0 \to J/\psi\pi^0$ Decays

Sachiko U. Kataoka
Nara Women's University
November 2004

Abstract

We present a measurement of CP asymmetry parameters in the decay $B^0(\overline{B}^0) \to J/\psi\pi^0$, which is governed by the $b \to c\bar{c}d$ transition. The analysis is based on a 140 fb^{-1} data sample accumulated at the $\Upsilon(4S)$ resonance by the Belle detector at the KEKB asymmetric-energy e^+e^- collider. We fully reconstruct one neutral B meson in the $J/\psi\pi^0$ final state, and the accompanying B meson flavor is identified by its decay products. Using 91 candidate events, we perform an unbinned maximum likelihood fit to the distribution of the time intervals between the two B meson decay points. We obtain the following CP-violating parameters:

$$\begin{aligned} \mathcal{S}_{J/\psi\pi^0} &= -0.72 \pm 0.42(\text{stat}) \pm 0.09(\text{syst}) \\ \mathcal{A}_{J/\psi\pi^0} &= -0.01 \pm 0.29(\text{stat}) \pm 0.03(\text{syst}). \end{aligned}$$

Contents

Introduction 1

1 CP Violation in the B Meson System **3**

1.1 Definitions of P, C and T Operators 3

1.2 CP Violation in K Meson System 4

1.3 Kobayashi-Maskawa Model 6

1.4 CP Violation in B Decays 7

1.4.1 B^0-$\overline{B}^0$ Mixing 7

1.4.2 B Meson Decays into CP Eigenstates 10

1.4.3 CP Violation in $B^0 \to J/\psi K_S$ Decays 11

1.4.4 CP Violation in $B^0 \to J/\psi \pi^0$ Decays 12

1.5 Principle of the Measurement 14

2 Experimental Apparatus **17**

2.1 KEKB accelerator 17

2.1.1 Asymmetric energy collider 17

2.1.2 High luminosity 18

2.2 The Belle Detector 18

2.2.1 Beam Pipe 20

2.2.2 Silicon Vertex Detector(SVD) 23

2.2.3 Central Drift Chamber(CDC) 25

2.2.4 Aerogel Čherenkov Counter(ACC) 27

2.2.5 Time of Flight Counter(TOF) 30

2.2.6 Electromagnetic Calorimeter(ECL) 32

2.2.7 Solenoid Magnet 37

2.2.8 K_L and Muon Detector(KLM) 37

2.2.9 Trigger and Data acquisition 38

2.2.10 Offline Software and Computing 41

2.3 Particle Reconstruction 42

2.3.1 Charged particle reconstruction 42

2.3.2 Photon reconstruction 43

2.4 Particle Identification . . . 44
2.4.1 $K^{\pm}/\pi^{\pm}$ Identification . . . 44
2.4.2 Electron Identification . . . 44
2.4.3 Muon Identification . . . 48

3 Event Selection and Reconstruction 50
3.1 Data Sample . . . 50
3.2 Hadronic Event Selection . . . 50
3.3 $B^0 \to J/\psi\pi^0$ Reconstruction . . . 52
3.3.1 Reconstruction of J/ψ . . . 52
3.3.2 Reconstruction of π^0 . . . 54
3.3.3 Reconstruction of B^0 . . . 54
3.4 Inclusive J/ψ Background . . . 55
3.5 Flavor Tagging . . . 58
3.5.1 Introduction of Flavor Tagging . . . 58
3.5.2 Flavor tagging Method . . . 58
3.5.3 Wrong tag fraction . . . 60
3.6 Reconstruction of Proper Time Difference . . . 61
3.6.1 Vertex Reconstruction of B_{CP} . . . 62
3.6.2 Vertex Reconstruction of $B_{\rm tag}$ . . . 63

4 Determination of CP Asymmetry 64
4.1 Maximum-likelihood fit Method . . . 64
4.2 Probability Density Function . . . 64
4.2.1 PDF for Signal . . . 65
4.2.2 Background Shape . . . 69
4.3 Signal and Background Probabilities . . . 71
4.4 Results of Fit to the Δt Distribution . . . 76
4.5 Systematic Uncertainties . . . 79
4.6 Validity Check . . . 79
4.6.1 Lifetime Fit . . . 80
4.6.2 Toy Monte Carlo study . . . 80
4.6.3 Goodness of Fit . . . 81

5 Conclusion 84

List of Figures

1.1 Results of the C, P and CP operations on neutrino states. 4
1.2 $K^0 - \bar{K^0}$ mixing 5
1.3 The unitarity triangle. 8
1.4 The box diagrams responsible for $B^0 - \overline{B}^0$ mixing 9
1.5 $J/\psi K_S$ decays 11
1.6 Tree diagram for $B^0 \to J/\psi\pi^0$ decays 13
1.7 Penguin diagram for $B^0 \to J/\psi\pi^0$ decays 13
1.8 The schematic picture of the experiment. 15

2.1 Configuration of the KEKB collider. 20
2.2 Configuration of the Belle detector system. 21
2.3 Side view of the Belle detector. 21
2.4 Definition of the coordinate system. 23
2.5 The cross secton of the beryllium beam pipe at the interaction point. . . . 23
2.6 Detector configuration of SVD 24
2.7 Schematic drawing of the DSSD. 25
2.8 SVD-CDC track matching efficiency as a function of the date of data taking. 26
2.9 Impact parameter resolution of charged tracks with associated SVD hits. . 26
2.10 Overview of the CDC structure. 27
2.11 Cell structure of CDC. 28
2.12 The p_t resolution is a function of p_t itself. 28
2.13 The measured dE/dx versus momentum observed in collision data. 29
2.14 Distribution of $(dE/dx)/(dE/dx_{exp})$ for pions from K^0_S decays 29
2.15 The arrangement of ACC 30
2.16 Pulse-height spectra in units of photoelectrons observed by barrel ACC for electrons and kaons. 31
2.17 Dimensions of a TOF/TSC module. 32
2.18 Time resolution for μ-pair events. 33
2.19 Mass distribution from TOF measurement for particle momenta below 1.2GeV/c. 33
2.20 Configuration of ECL. 34

2.21 The CsI(Tl) crystal shape. 35
2.22 The mechanical assembly of the CsI(Tl) counter. 35
2.23 Block diagram of the CsI(Tl) readout electronics. 36
2.24 The energy resolution and the position resolution of ECL as a function of incident photon energy. 37
2.25 An outlook of the solenoid and the cross-sectional view of the coil. 38
2.26 Barrel part of the iron yoke. 39
2.27 Cross section of a KLM super-layer. 39
2.28 Muon identification efficiency versus momentum in KLM and fake rate for charged pions versus momentum in KLM. 40
2.29 The Level-1 trigger system for the Belle detector. 40
2.30 Belle DAQ system overview. 41
2.31 The cluster of 5×5 crystals. 43
2.32 K efficiency and π fake rate as a function of momentum. 44
2.33 $\Delta\phi$, $\Delta\theta$ and the matching χ^2 distributions. 45
2.34 E/p distribution and momentum dependence distribution of E/p. 46
2.35 $E9/E25$ distribution 47
2.36 dE/dx distribution and momentum dependence distribution of dE/dx . . . 47
2.37 Electron identification efficiency (circles) and fake rate for charged pions (squares). 48
2.38 Muon identification efficiency versus momentum in KLM and fake rate for charged pions versus momentum in KLM. 49

3.1 The invariant mass distribution of $M_{e^+e^-}$. 53
3.2 The invariant mass distribution of $M_{\mu^+\mu^-}$. 54
3.3 The invariant mass distribution of photon pairs. 55
3.4 The distribution of ΔE versus $M_{\rm bc}$ for $B^0 \to J/\psi\ \pi^0$ candidates in data. . 56
3.5 $B \to J/\psi X$ background study. 57
3.6 The schematic view of the flavor tagging algorithm. 60

4.1 $\tau_{\rm bkg}^{\rm J/\psi X}$ is detrmined by fit to Δt distribution for inclusive J/ψ Monte carlo sample. 70
4.2 The fit results on $M_{\rm bc}$ distribution of the signal Monte Carlo for $-0.10{\rm GeV} < \Delta E < 0.05{\rm GeV}$. 72
4.3 The fit results on ΔE distribution of the signal Monte Carlo for $5.27{\rm GeV}/c^2 < M_{\rm bc} < 5.29{\rm GeV}/c^2$. 73
4.4 ΔE distribution for events in the $M_{\rm bc}$ signal region and $M_{\rm bc}$ distribution for events in the ΔE signal region, for $B^0 \to J/\psi\pi^0$ candidates. 75

4.5 The Δt distributions for $\overline{B}^0 \to J/\psi\pi^0$ ($q = +1$) and $B^0 \to J/\psi\pi^0$ ($q = -1$) candidates. 77
4.6 The asymmetry, A, in each Δt bin for $B^0 \to J/\psi\ \pi^0$ candidates. 78
4.7 Lifetime fit 80
4.8 Pull distribution for $\mathcal{S}_{J/\psi\pi^0}$ and $\mathcal{A}_{J/\psi\pi^0}$ 81
4.9 Result of toy Monte carlo for $\mathcal{S}_{J/\psi\pi^0}$ and $\mathcal{A}_{J/\psi\pi^0}$. 82
4.10 Linearity test : Mean value of fit result vs. each input value for $\mathcal{S}_{J/\psi\pi^0}$ and $\mathcal{A}_{J/\psi\pi^0}$. 83

5.1 Comparison of the measurements for $\mathcal{S}_{J/\psi\pi^0}$ and $\mathcal{C}_{J/\psi\pi^0} = -\mathcal{A}_{J/\psi\pi^0}$ between Belle and BaBar experiments. 85
5.2 Comparison of the various measurements of $-\eta_f S_f$. 86

List of Tables

1.1 Behavior of various basic observables under C, P and T operations. 4

2.1 Main parameters of KEKB. 19
2.2 Performance parameters expected (or achieved) for the Belle detectror. . . 22

3.1 Branching fractions for each decay modes related to this analysis. 50
3.2 Cross sections for each processes in e^+e^- collisions at the center of mass energy of $\sqrt{s} = 10.58$ GeV. 51
3.3 Breakdown of decays in the signal box from 15.4 M events for neutral B inclusive J/ψ Monte Carlo, and from 11.1 M events charged B inclusive J/ψ Monte Carlo sample 57
3.4 The list of detector resolution function parameters. 58
3.5 Wrong tag fraction parameters. 62

4.1 The list of detector resolution function parameters. 67
4.2 List of $R_{\rm np}$ parameters determined with the Monte Carlo simulation. . . . 68
4.3 Combinatorial background PDF and resolution function parameters. 71
4.4 Parameters obtained from fit to $M_{\rm bc}$ and ΔE distribution of the signal Monte Carlo. 74
4.5 Parameters obtained from fit to $M_{\rm bc}$ and ΔE distribution of $B \to J/\psi X$ Monte Carlo. 74
4.6 Parameters obtained from fit to $M_{\rm bc}$ and ΔE distribution of the real data. 75
4.7 Functions for unbinned-maximum likelihood fit to ΔE - $M_{\rm bc}$. 75
4.8 Signal fraction : Result of fit to $M_{\rm bc}$ - ΔE distribution. 76
4.9 Systematic uncertainties. 80

Introduction

If we believe that there were the same amount of matter and antimatter at the beginning of the universe and allmost all the laws of nature are symmetric between matter and antimatter, it is the puzzle how is the current Universe, which is composed entirely matter, evolved from the Big Bang. The CP violation, *i.e.* matter-antimatter asymmetry is a key of understanding this puzzle.

CP asymmetry was first observed in neutral K meson system by J. Christenson *et al* in 1964 [1]. This discovery initiated many theoretical efforts to understand the CP violation phenomenon. In 1973, Kobayashi and Maskawa found that CP violation is caused by one or more irreducible complex phase in the quark-flavor mixing matrix when at least six quarks exist [2]. At that time, however, only three types of quark, up (u), down (d) and strange (s) were known. Subsequently, the fourth and fifth quarks, charm (c) and bottom (b) , were discovered in 1970s, and the observation of sixth quark, *i.e.* top (t) quark in 1995 established the Kobayashi-Maskawa model (KM model) as an essential part of the Standard Model.

In 1980, I. Sanda, I. Bigi and A. Carter pointed out that sizable CP asymmetry can be observed in B meson system [3]. The subsequent observation of a long b quark lifetime [4] and a large amount of mixing in the neutral B meson system [5] indicated that it would be feasible to carry out decisive tests of the KM model by studying B meson decay. And it would be important milestone, that is the first successful demonstration of a CP-violating effect outside of the K meson system. Therefore, the study of B meson is one of most important subjects in the field of particle physics, and the two experiments, Belle and BaBar, were constructed in Japan and USA, respectively.

The Belle experiment has started since 1994 at KEK, employing KEKB accelerator [6] and Belle detector [7]. KEKB accelerator is an asymmetric-energy e^+e^- (3.5 GeV on 8.0 GeV) collider operated on the $\Upsilon(4S)$ resonance and it produces a huge number of B meson with clean final states. To measure CP violation, it requires precise determination of the proper-time difference (Δt) between the two neutral B mesons, where one decays to CP eigenstate (B_{CP}) and the other decays to anything ($B_{\rm tag}$). Thanks to asymmetric energy collision, produced B mesons are boosted. Therefore, the time dependent decay rate can be measured using the information of the flight lengths of B meson decays,

and we can obtain CP violation. The Belle detector is designed to determine the decay positions of B mesons precisely, identify the flavor of B meson with the good particle-identification capability, to measure final state particles' energies and momenta with high resolution. We started data taking from June 1999, and recorded 140 fb^{-1} data by July 2003 (corresponding to 15.2×10^7 $B\overline{B}$ pairs) with the Belle detector.

Among the neutral B meson decays, one of the most promising modes to observe CP violation is $B^0 \to J/\psi K_S$ decay, from which we extract CP-violating parameter "$\sin 2\phi_1$". Recent measurements of $\sin 2\phi_1$ by the Belle [8] and BaBar [9] experiments established the CP violation in the neutral B meson system, as predicted by the KM model.

Now B physics is in the next stage to deal with precise determination and test of the KM model, relating CP violation using neutral B decays other than $B^0 \to J/\psi K_S$ decays.

Study of the CP violation in $B^0 \to J/\psi\pi^0$ decays is one of the important issues to test KM model. $B^0 \to J/\psi\pi^0$ decays is governed by the $b \to c\bar{c}d$ transition. For tree diagrams in $B^0 \to J/\psi\pi^0$, the KM model predicts CP-violating parameter is given by $-\sin 2\phi_1$, where minus sign corresponds opposite CP eigenvalues between $B^0 \to J/\psi K_S$ (-1) and $B^0 \to J/\psi\pi^0$ $(+1)$. In contrast to the $B^0 \to J/\psi K_S$ case, however, tree and penguin amplitudes contribute to $b \to c\bar{c}d$ to the same order in the sine of the Cabibbo angle. Therefore, if penguin or other contributions are substantial, a precision measurement of the time-dependent CP asymmetry in $B^0 \to J/\psi\pi^0$ decays may reveal values of CP-violating parameter that differ from the values for $B^0 \to J/\psi K_S$ decays. A study of CP asymmetry in $B^0 \to J/\psi\pi^0$ decays has been reported by the BaBar collaboration [10] based on 81 fb^{-1}.

The goal of this thesis is measurement of CP asymmetries in $B^0 \to J/\psi\pi^0$ decays at the Belle experiment using higher statistics of 140 fb^{-1} data sample, as one of the important issues to test. The outline of the thesis is as follows: Theoretical description of CP violation and the principle of measurement of the CP violation in the neutral B meson-system are provided in Chapter 1. Experimental apparatus and relevant software used in this study are described in Chapter 2. The reconstruction procedure of the candidates for $B^0 \to J/\psi\pi^0$ decays, determination of proper-time difference Δt, and the method of flavor tagging are described in Chapter 3. The procedure to determine the CP violation parameter is explained in Chapter 4, . Finally, the conclusion is given in Chapter 5.

Chapter 1

CP Violation in the B Meson System

1.1 Definitions of P, C and T Operators

The parity operator, P produces the operation of spatial inversion of coordinates

$$(x, y, z) \implies (-x, -y, -z).$$

Let us define a spin and momentum of particle f as $\vec{\sigma}$ and $\vec{p}$, respectively.
The state of $|f; \vec{\sigma}\ \vec{p}>$ is transformed by the operator P as

$$P|f; \vec{\sigma}\ \vec{p}>= \eta_P|f; \vec{\sigma}\ \vec{p}>,$$

where η_P is a phase of parity transformation. Since P^2 is an identical operator, ${\eta_P}^2$ is 1, and thus $\eta_P = \pm 1$.

The Charge conjugation operator, C changes the sign of internal charges such as electric charge, baryon number and so on. This operation replaces particle f with thier antiparticles $\bar{f}$ (and vice versa) as

$$C|f; \vec{\sigma}\ \vec{p}>= \eta_C|\bar{f}; \vec{\sigma}\ \vec{p}>,$$

where η_C is a phase.

The third fundamental operator, T is a time reversal transformation which inverse the time coordinates:

$$T|f; \vec{\sigma}\ \vec{p}>= \eta_T|\bar{f}; -\vec{\sigma}\ -\vec{p}>,$$

where η_T is a phase. Table 1.1 is shown the effects of P, C and T transformation on each parameter.

According to the CPT theorem, the combined operation CPT is invariant in relativistic field theory.

Until the early 1950's, one believed that all are conserved under each of these transformation, C, P and T. In 1956, however, T. Lee and C. Yang pointed out the violation of the parity conservation [11], and the subsequent experiments by C. Wu *et al.* and by

		C	P	T
r	(spatial coordinates)	r	r	r
p	(momentum)	p	$-p$	$-p$
J	(angular momentum)	J	J	J
σ	(spin)	σ	σ	$-\sigma$
E	(electric field)	E	$-E$	E
B	(magnetic field)	B	B	B
$\sigma \cdot p$	(helicity)	$\sigma \cdot p$	$-\sigma \cdot p$	$\sigma \cdot p$

Table 1.1: *Behavior of various basic observables under C, P and T operations.*

R. Garwin *et al.* in 1957 independently demonstrated that weak interactions violate C-invariance just as they violate P-invariance in weak decays of nuclei and of muons [12][13]. This violation is visualized by the longitudinal polarization of neutrinos and antineutrinos. Neutrino has helicity of -1 (left-handed), and antineutrino has a helicity $+1$. As illustrated in Figure 1.1, left-handed neutrino applied P or C operation is not observed experimentally. However, the combine operation CP, which transforms a left-handed neutrino into right-handed neutrino, is not forbidden.

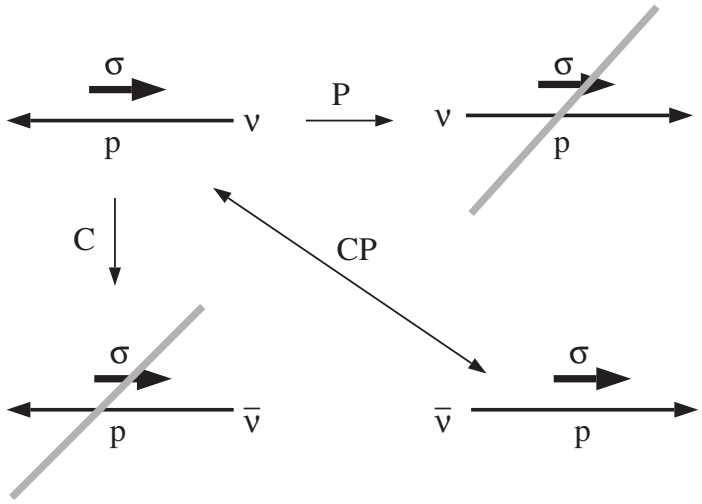

Figure 1.1: *Results of the C, P and CP operations on neutrino states. Only left-handed neutrino (left-top), and right-handed neutrino which is result of appliying CP operation to left-handed neutrino (right-bottom), are observed in nature.*

1.2 CP Violation in K Meson System

Following the discovery of parity violation in weak decay processes in 1957, it was believed that the weak interactions were at least invariant under the CP operation. However, L. H. Christenson, J. W. Cronin, V. L. Fitch, and R. Turlay discovered the violation of the CP system in K^0 meson decays [1]. There are two neutral strange mesons, K^0 and $\overline{K}^0$. The

quark contents of them are

$$K^0(\bar{s}d) \ , \quad \bar{K^0}(s\bar{d}).$$

As shown in Figure 1.2. K^0 and $\overline{K}^0$ can mix via exchange of W bosons, which is called "box diagrams".

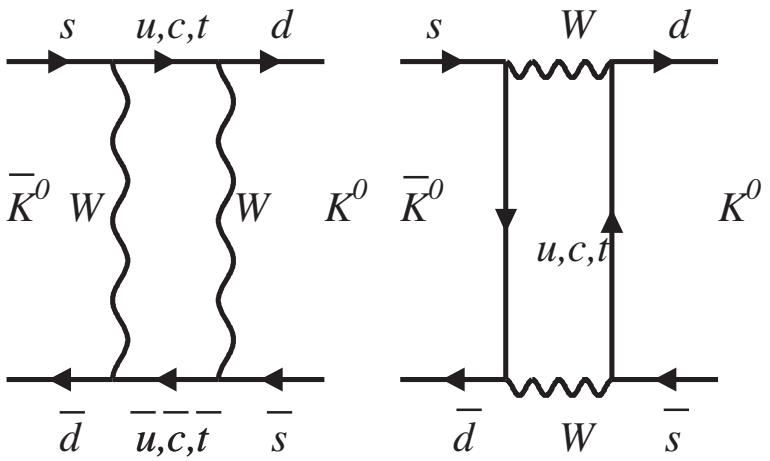

Figure 1.2: $K^0 - \bar{K^0}$ *mixing*

We define that operation of CP on the states K^0 and $\overline{K}^0$ gives $CP|K^0>=|\overline{K}^0>$ and $CP|\overline{K}^0>=|K^0>$. We can form the linear combinations of K^0 and $\overline{K}^0$ as a CP eigenstate of neutral K mesons:

$$\begin{aligned} |K_1> &= \frac{1}{\sqrt{2}}(|K^0> + |\bar{K^0}>) \\ |K_2> &= \frac{1}{\sqrt{2}}(|K^0> - |\bar{K^0}>) \end{aligned}$$

where

$$\begin{aligned} CP|K_1> &= +|K_1> \qquad (CP=+1) \\ CP|K_2> &= -|K_2> \qquad (CP=-1) \end{aligned}$$

Experimentally, it was observed that there are two lifetime of neutral K mesons, where the shorter lived was named K_S, and the longer lived was named K_L. Since it was measured that K_S decays into two-pions of which CP eigenvalue is $+1$, and K_L decays three-pions of which CP eigenvalue is -1, it was considered that K_S and K_L correspond to the K_1 and K_2 respectively, at that time. The longer life of K_L is due to limited phase space. Under the CP conservation, $K_L \to \pi^+ \pi^-$ is forbidden. However, L. H. Christenson

et al. group discovered the small fraction decay of $K_L \to \pi^+\pi^-$. The branching fraction was order of $\sim 10^{-3}$. Thus, K_L should be rewritten as

$$|K_L> \;=\; \frac{1}{\sqrt{(2(1+|\epsilon|^2)}}((1+\epsilon)|K^0> -(1-\epsilon)|\bar{K^0}>)$$

It means there is CP violation with ϵ between K^0 and $\bar{K^0}$. Charged asymmetries in $K_L \to \pi^\pm e^\mp \nu$ [14] and $K_L \to \pi^\pm \mu^\mp \nu$ [15] also confirmed the CP violation in neutral K meson system. The theoretical explanation within the Standard Model for the origin of the CP violation was proposed by Kobayashi and Maskawa in 1973 [2], which is described in the next section.

1.3 Kobayashi-Maskawa Model

In 1973, M. Kobayashi and T. Maskawa proposed that the existence of at least three quark generations, six quarks, can explain the CP violation, even though only three quarks had been observed, at that time. After that, c, b, and t quark were discovered in 1974, 1977 and 1995, respectively, and thus Kobayashi-Maskawa mechanism becomes a essential part of the Standard Model.

In the Standard Model, six quarks form the three doublets that are called as three quark generations:

$$\begin{pmatrix} u \\ d \end{pmatrix} \qquad \begin{pmatrix} c \\ s \end{pmatrix} \qquad \begin{pmatrix} t \\ b \end{pmatrix}$$

in terms of mass eigenstates. The Lagrangian of charged-current weak interaction is expressed as

$$\mathcal{L} = \frac{g}{\sqrt{2}} \left\{ (\bar{u}, \bar{c}, \bar{t})_L \gamma^\mu W_\mu^+ V_{KM} \begin{pmatrix} d \\ s \\ b \end{pmatrix}_L + (\bar{d}, \bar{s}, \bar{b})_L \gamma^\mu W_\mu^- V_{KM}^\dagger \begin{pmatrix} u \\ c \\ t \end{pmatrix}_L \right\}$$

where,

$$\begin{aligned} g &: \text{coupling constant} \\ \gamma^\mu &: \gamma \text{ matrix} \\ W^\pm &: W \text{ bosons} \\ \begin{pmatrix} d \\ s \\ b \end{pmatrix}_L \text{ or } \begin{pmatrix} u \\ c \\ t \end{pmatrix}_L &: \text{left} - \text{handed quark} \end{aligned}$$

and V_{KM} is mixing matrix named Kobayashi-Maskawa matrix.

$$V_{KM} \;=\; \begin{pmatrix} V_{ud} & V_{us} & V_{ub} \\ V_{cd} & V_{cs} & V_{cb} \\ V_{td} & V_{ts} & V_{tb} \end{pmatrix} \tag{1.1}$$

Since V_{KM} is unitary matrix, it satisfy:

$$V_{KM}^{\dagger} V_{KM} = \begin{pmatrix} V_{ud}^* & V_{cd}^* & V_{td}^* \\ V_{us}^* & V_{cs}^* & V_{ts}^* \\ V_{ub}^* & V_{cb}^* & V_{tb}^* \end{pmatrix} \begin{pmatrix} V_{ud} & V_{us} & V_{ub} \\ V_{cd} & V_{cs} & V_{cb} \\ V_{td} & V_{ts} & V_{tb} \end{pmatrix} = I \tag{1.2}$$

Thus,

$$\sum_{i=u,c,t} V_{ij}^* V_{ik} \quad = \delta_{jk} \quad (j,k = d,s,b) \tag{1.3}$$

The matrix elements are parametrized by three real parameters and a complex phase. The complex phase introduces CP violation. It is convenient to write the matrix in Wolfenstein parametrization[16] which is an expansion in powers of sine of Cabibbo angle, $\lambda \equiv \sin\theta_c \simeq 0.22$:

$$V_{KM} = \begin{pmatrix} 1-\lambda^2/2 & \lambda & A\lambda^3(\rho - i\eta) \\ -\lambda & 1-\lambda^2/2 & A\lambda^2 \\ A\lambda^3(1-\rho-i\eta) & -A\lambda^2 & 1 \end{pmatrix} + \mathcal{O}(\lambda^4)$$

Among Equation (1.2), the relation involving V_{td} and V_{ub}, which relate B meson decays, results in

$$V_{ud}V_{ub}^* + V_{cd}V_{cb}^* + V_{td}V_{tb}^* = 0$$

Each term is expressed in Wolfenstein parametrization

$$\begin{aligned} V_{ud}V_{ub}^* &\simeq A\lambda^3(\rho + i\eta) \\ V_{cd}V_{cb}^* &\simeq -A\lambda^3 \\ V_{td}V_{tb}^* &\simeq A\lambda^3(1-\rho-i\eta) \end{aligned}$$

The three terms form a closed triangle in the complex plane, which is called "unitarity triangle", as shown in Figure 1.3. The three angle of the triangles are defined as

$$\phi_1 \equiv \arg\left(\frac{V_{cd}V_{cb}^*}{V_{td}V_{tb}^*}\right),\ \phi_2 \equiv \arg\left(\frac{V_{ud}V_{ub}^*}{V_{td}V_{tb}^*}\right),\ \phi_3 \equiv \arg\left(\frac{V_{cd}V_{cb}^*}{V_{ud}V_{ub}^*}\right)$$

Since the length of all three sides are the same order of $\mathcal{O}(\lambda^3)$, we can expect large CP violation such as $\mathcal{O}(0.1) \sim \mathcal{O}(1)$ in the B meson systems.

1.4 CP Violation in B Decays

1.4.1 B^0-$\overline{B}^0$ Mixing

As same as K^0 meson system, B^0 and $\overline{B}^0$ can mix through second order weak interactions via box diagrams shown in Figure 1.4. Due to mixing, arbitrary neutral B meson state is written as linear combination of B^0 and $\overline{B}^0$

$$|B(t)\ > = \ \alpha(t)\ |B^0\ > \ + \beta(t)\ |\bar{B}^0\ > \tag{1.4}$$

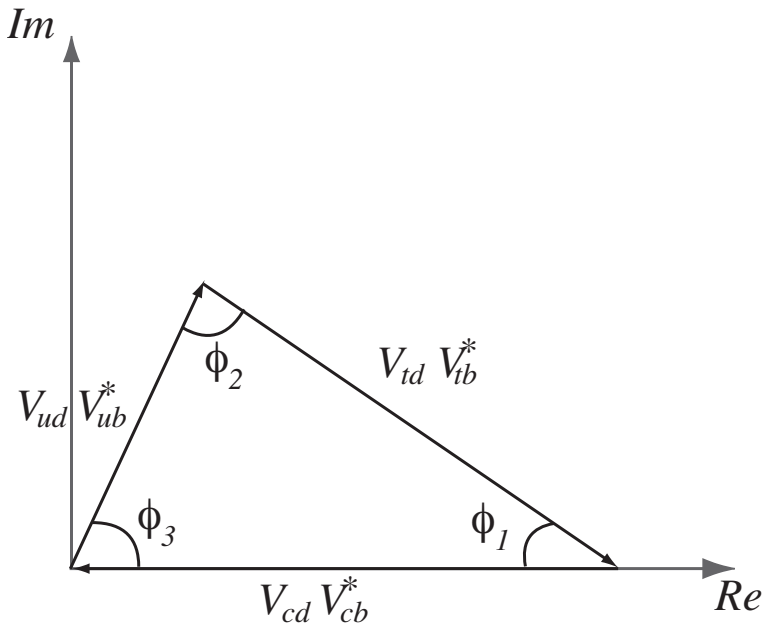

Figure 1.3: *The unitarity triangle.*

The time-dependent Schrödinger equation of $|B(t)>$ with the Hamiltonian of $\mathcal{H}$ is

$$i\frac{\partial}{\partial t}|B(t)> \;=\; \mathcal{H}\,|B(t)> \tag{1.5}$$

$\mathcal{H}$ is defined as

$$\mathcal{H} = \mathbf{M} - \frac{i}{2}\Gamma = \begin{pmatrix} M_{11} - \frac{i}{2}\Gamma_{11} & M_{12} - \frac{i}{2}\Gamma_{12} \\ M_{12} - \frac{i}{2}\Gamma_{12} & M_{22} - \frac{i}{2}\Gamma_{22} \end{pmatrix} \tag{1.6}$$

where, $\mathbf{M}$ and Γ are Hermitian matrices, which are called the mass and decay matrices, respectively. M_{11} and M_{22} are the B^0 and $\bar{B}^0$ mass, and Γ_{11} and Γ_{22} are the decay width of the flavor eigenstates, B^0 and $\bar{B}^0$, respectively. $M_{12}(M_{21})$ and $\Gamma_{12}(\Gamma_{21})$ represent transition amplitude from B^0 to $\overline{B}^0$ (from $\overline{B}^0$ to B^0).

Since CPT invariance requires $M_{11} = M_{22} \equiv M_0$ and $\Gamma_{11} = \Gamma_{22} \equiv \Gamma_0$, eigenvalues $\mu_\pm$ of Schrödinger equation of (1.5) can be written as

$$\begin{aligned} \mu_{H,L} &= m_{H,L} - \frac{i}{2}\Gamma_{H,L} \\ &= \left(M_0 - \frac{i}{2}\Gamma_0\right) \pm \left[\left(M_{12} - \frac{i}{2}\Gamma_{12}\right)\left(M_{12}^* - \frac{i}{2}\Gamma_{12}^*\right)\right]^{\frac{1}{2}} \end{aligned} \tag{1.7}$$

which correspond to eigenvectors $|B_{H,L}>$ that are given as

$$|B_{H,L}> \;=\; p|B^0> \,\pm\, q|\bar{B}^0>\,, \tag{1.8}$$

$$\frac{q}{p} \;=\; \left(\frac{M_{12}^* - \frac{i}{2}\Gamma_{12}^*}{M_{12} - \frac{i}{2}\Gamma_{12}}\right)^{\frac{1}{2}} \tag{1.9}$$

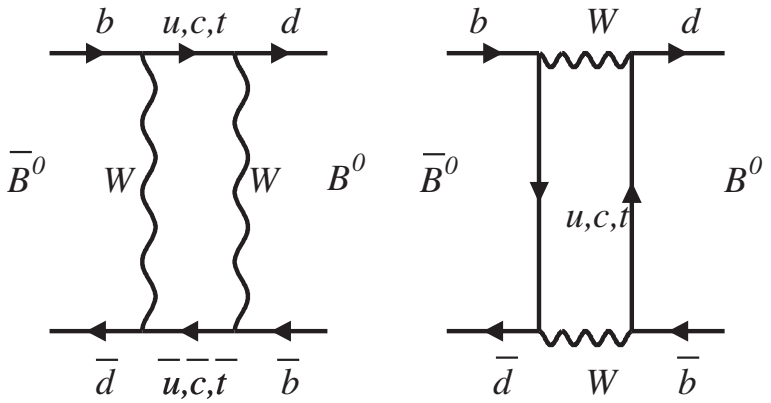

Figure 1.4: *The box diagrams responsible for* $B^0 - \overline{B}^0$ *mixing*

where p and q are normalized as $|p^2| + |q^2| = 1$. H, L represents "light" mass eigenstate of $|B_L>$ and "heavy" mass eigenstate of $|B_H>$, and we defined mass and width of $B_{H,L}$ as $m_{H,L}$ and $\Gamma_{H,L}$, respectively. Using Equation (1.7), time evolutions of $|B_H>$ and $|B_L>$ are given by

$$|B_H(t)> \;=\; (p|B^0> \,+\, q|\bar{B}^0>)e^{-i\mu_H t} \tag{1.10}$$

$$|B_L(t)> \;=\; (p|B^0> \,-\, q|\bar{B}^0>)e^{-i\mu_L t} \tag{1.11}$$

From Equation (1.8), flavor eigenstates, B^0 and $\bar{B}^0$ are expressed as

$$|B^0> = \frac{1}{2p}(|B_H> \,+\, |B_L>)\ ,\ |\bar{B}^0> = \frac{1}{2q}(|B_H> \,-\, |B_L>). \tag{1.12}$$

Thus, time evolutions of B^0 and $\overline{B}^0$ are given by

$$|B^0(t)> \;=\; g_+(t)|B^0> + \frac{q}{p}g_-(t)|\bar{B}^0> \tag{1.13}$$

$$|\bar{B}^0(t)> \;=\; \frac{p}{q}g_-(t)|B^0> + g_+(t)|\bar{B}^0> \tag{1.14}$$

where

$$g_\pm = \frac{1}{2}(e^{-i\mu_H t} \pm e^{-i\mu_L t}), \tag{1.15}$$

and Δm $\Delta\Gamma$ are the difference of mass and width of the two mass eigenstates as

$$\begin{aligned}
\Delta m &= m_H - m_L \\
&= 2Re\sqrt{\left(M_{12} - \frac{i}{2}\Gamma_{12}\right)\left(M_{12}^* - \frac{i}{2}\Gamma_{12}^*\right)} \\
\Delta\Gamma &= \Gamma_H - \Gamma_L \\
&= -4Im\sqrt{\left(M_{12} - \frac{i}{2}\Gamma_{12}\right)\left(M_{12}^* - \frac{i}{2}\Gamma_{12}^*\right)}
\end{aligned}$$

In the B meson system, the neutral B meson mass is heavy enough to reduce such an effect to a level of $(\Gamma_H - \Gamma_L)/\Gamma \sim \mathcal{O}(10^{-3})$. Therefore, we set $\Gamma_H = \Gamma_L = \Gamma$. Thus, are represented with $\Delta\Gamma = 0$ as

$$g_\pm = \frac{1}{2}\exp\left\{\left(-iM - \frac{\Gamma}{2}\right)t\right\}(1 \pm \exp(-i\Delta mt)) \tag{1.16}$$

1.4.2 B Meson Decays into CP Eigenstates

In this subsection, we consider time evolution of neutral B mesons decays into a CP eigenstate, f_{CP} that is possible for both B^0 and $\overline{B}^0$ decays. we dedine the amplitudes of these processes as

$$A(f_{CP}) \equiv < f_{CP}|\mathcal{H}|B^0 > \ , \ \bar{A}(f_{CP}) \equiv < f_{CP}|\mathcal{H}|\bar{B}^0 >$$

Using Equations (1.13) and (1.14), the time-dependent decay rates for initially pure B^0 or $\bar{B}^0$ states decaying into f_{CP} are given by

$$\begin{aligned}
\Gamma(B^0(t) \to f_{CP}) = e^{-\Gamma t}|A|^2 &\left[\frac{1+\cos\Delta mt}{2} + \left|\frac{q}{p}\right|^2 |\bar{\rho}(f_{CP})|^2 \frac{1-\cos\Delta mt}{2}\right. \\
&\left. - \left[\left(\frac{q}{p}\right)\bar{\rho}(f_{CP})\right]\sin\Delta mt\right] \\
\Gamma(\bar{B}^0(t) \to f_{CP}) = e^{-\Gamma t}|\bar{A}|^2 &\left[\frac{1+\cos\Delta mt}{2} + \left|\frac{p}{q}\right|^2 |\rho(f_{CP})|^2 \frac{1-\cos\Delta mt}{2}\right. \\
&\left. - \left[\left(\frac{p}{q}\right)\rho(f_{CP})\right]\sin\Delta mt\right]
\end{aligned} \tag{1.17}$$

where,

$$\begin{aligned}
\bar{\rho}(f_{CP}) &\equiv \frac{\bar{A}(f_{CP})}{A(f_{CP})}, \\
\rho(f_{CP}) &\equiv \frac{A(f_{CP})}{\bar{A}(f_{CP})}.
\end{aligned} \tag{1.18}$$

Let λ_{CP} define as

$$\lambda_{CP} \equiv \frac{q}{p}\bar{\rho}(f_{CP}), \tag{1.19}$$

The decay rates are written as

$$\begin{aligned}\Gamma(B^0(t) \to f_{CP}) &= e^{-\Gamma t}|A|^2 \left[1 - \frac{|\lambda_{CP}|^2 - 1}{|\lambda_{CP}|^2 + 1}\cos\Delta mt - \frac{2\lambda_{CP}}{|\lambda_{CP}|^2 + 1}\sin\Delta mt\right] \\ \Gamma(\bar{B}^0(t) \to f_{CP}) &= e^{-\Gamma t}|A|^2 \left[1 + \frac{|\lambda_{CP}|^2 - 1}{|\lambda_{CP}|^2 + 1}\cos\Delta mt + \frac{2\lambda_{CP}}{|\lambda_{CP}|^2 + 1}\sin\Delta mt\right]\end{aligned} \tag{1.20}$$

Thus, the time-dependent CP asymmetry is defined as the normalized decay rate difference:

$$\begin{aligned}a_{f_{CP}} \equiv& \frac{\Gamma(\bar{B}^0(t) \to f_{CP}) - \Gamma(B^0(t) \to f_{CP})}{\Gamma(\bar{B}^0(t) \to f_{CP}) + \Gamma(B^0(t) \to f_{CP})} \\ =& \frac{(|\lambda_{CP}|^2 - 1)\cos\Delta mt + 2\lambda_{CP}\sin\Delta mt}{|\lambda_{CP}|^2 + 1},\end{aligned} \tag{1.21}$$

1.4.3 CP Violation in $B^0 \to J/\psi K_S$ Decays

$B^0 \to J/\psi K_S$, which is governed by the $b \to c\bar{c}s$ transition, is promissing decay mode to extract ϕ_1 experimentally. This decay mode is so-called "golden mode", because of relatively large branching fractions with small backgrounds. In addition, the final state has only negligible theoretical uncertainty in ϕ_1 measurement. In the following, we describe time-dependent CP violation in $B^0 \to J/\psi K_S$ decays briefly.Therefore, we can neglect the contribution from the weak phase in other than As for the tree diagram for $B^0 \to J/\psi K_S$ as shown in Figure 1.5,

$$\frac{\bar{A}(\bar{B}^0 \to J/\psi K_S)}{A(B^0 \to J/\psi K_S)} = \frac{V_{cb}V_{cs}^*}{V_{cb}^*V_{cs}} = 1. \tag{1.22}$$

The dominant penguin contribution has the same weak phase as the tree. Therefore, we can neglect the contribution from the weak phases other than the tree diagram.

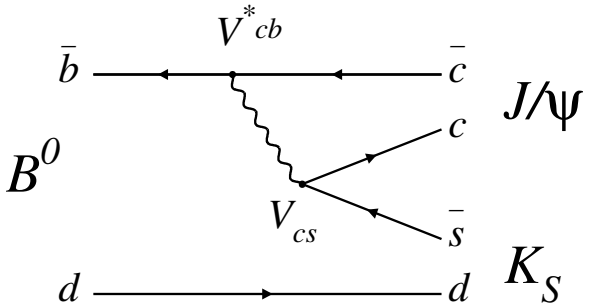

Figure 1.5: $J/\psi K_S$ *decays*

Here, we calculate q/p. The main contribution to the box diagrams of B^0-$\bar{B}^0$ mixing in Figure 1.4 is the top quark because of its heavy mass, and the CKM matrix elements contributing to the mixing are $V_{tb}V_{td}^*$ on the vertices of the box diagrams. Theoretical

calculations [17]-[20] on M_{12}, Γ_{12} and their ratio yield:

$$\begin{aligned} M_{12} &\propto (V_{tb}V_{td}^*)^2 m_t^2, \\ \Gamma_{12} &\propto (V_{tb}V_{td}^*)^2 m_b^2, \\ \left|\frac{\Gamma_{12}}{M_{12}}\right| &\simeq \frac{m_b^2}{m_t^2} \simeq 10^{-3}, \end{aligned} \tag{1.23}$$

where m_b is the bottom quark mass and m_t is the top quark mass. Using (1.9) and (1.23), the q/p becomes

$$\begin{aligned} \frac{q}{p} &= \sqrt{\frac{M_{12}^*}{M_{12}}} + \mathcal{O}\left(\frac{\Gamma_{12}}{M_{12}}\right) \\ &\simeq \frac{V_{tb}^* V_{td}}{V_{tb} V_{td}^*} = e^{-2i\phi_1} \end{aligned} \tag{1.24}$$

Therefore , $\lambda_{J/\psi K_S}$ which corresponds to Equation (1.19) by replacing $f_{CP} = J/\psi K_S$, becomes

$$\begin{aligned} \lambda_{J/\psi K_S} &\propto -\frac{\bar{A}(\bar{B}^0 \to J/\psi K_S)}{A(B^0 \to J/\psi K_S)} \cdot \left(\frac{q}{p}\right) \\ &\simeq -\frac{V_{cb}V_{cs}^*}{V_{cb}^* V_{cs}} \cdot \frac{V_{tb}^* V_{td}}{V_{tb} V_{td}^*} \\ &= -e^{-2i\phi_1}. \end{aligned}$$

The minus sign in front of Equation 1.4.3 corresponds to the state of $|J/\psi K_S>$ being CP odd. Because of $|B^0 \to J/\psi K_S| = |\bar{B}^0 \to J/\psi K_S|$ and $|q/p| = 1$, $|\lambda_{J/\psi K_S}| = 1$ holds, As a result, Equation (1.20) becomes:

$$\begin{aligned} \Gamma(B^0(t) \to f_{CP}) &= e^{-\Gamma t}|A|^2(1 - \sin 2\phi_1 \cdot \sin \Delta m t), \\ \Gamma(\bar{B}^0(t) \to f_{CP}) &= e^{-\Gamma t}|A|^2(1 + \sin 2\phi_1 \cdot \sin \Delta m t), \end{aligned} \tag{1.25}$$

and time-dependent asymmetry for $B^0 \to J/\psi K_S$ decays is given by

$$a_{J/\psi K_S} = \sin 2\phi_1 \cdot \sin \Delta m t. \tag{1.26}$$

CP violation in these decays involving the $b \to c\bar{c}s$ transition has been established by the Belle [8] and BaBar [9] collaborations. The measured results are in good agreement with the Standard Model expectation. Therefore, we can regard the CP-violating parameter $\sin 2\phi_1$ measured in $B^0 \to J/\psi K_S$ decays as the value for the Standard Model.

1.4.4 CP Violation in $B^0 \to J/\psi\pi^0$ Decays

The decay of $B^0 \to J/\psi\pi^0$ is induced by $b \to c\bar{c}d$. The tree and penguin diagram for $B^0 \to J/\psi\pi^0$ decays are shown in Figure 1.6 and 1.7. The decay amplitudes of the tree diagram, $A_{\rm T}(B^0 \to J/\psi\pi^0)$ and the penguin diagram $A_{\rm P}(B^0 \to J/\psi\pi^0)$ are written as

$$A_{\rm T}(B^0 \to J/\psi\pi^0) \equiv < J/\psi\pi^0|\mathcal{H}_{\rm tree}|B^0 > = V_{cb}^* V_{cd} A_{\rm tree} \tag{1.27}$$

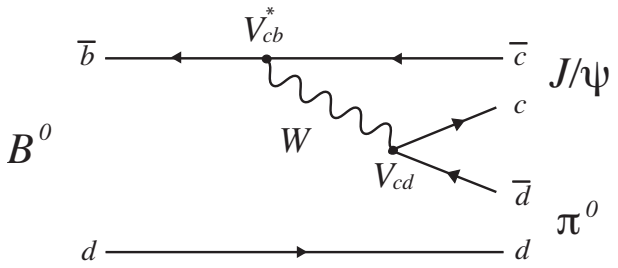

Figure 1.6: *Tree diagram for $B^0 \to J/\psi\pi^0$ decays*

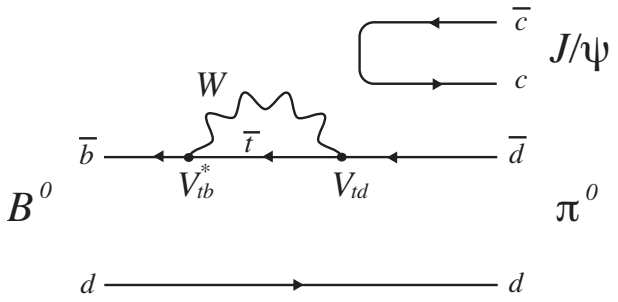

Figure 1.7: *Penguin diagram for $B^0 \to J/\psi\pi^0$ decays*

and

$$\begin{aligned} A_{\rm P}(B^0 \to J/\psi\pi^0) &\equiv < J/\psi\pi^0|\mathcal{H}_{\rm penguin}|B^0 > \\ &= V_{tb}^* V_{td} A^t_{\rm penguin} + V_{cb}^* V_{cd} A^c_{\rm penguin} + V_{ub}^* V_{ud} A^u_{\rm penguin} \end{aligned} \tag{1.28}$$

where $A_{\rm tree}$ and $A^i_{\rm penguin}$ $(i = u, c, t)$ are the amplitudes apart from the explicitly shown CKM factors. The amplitude $\bar{A}$ is given by the complex conjugate CKM matrix elements and the same $A_{\rm tree}$ and $A^i_{\rm penguin}$ terms. As for $A_{\rm T}$, $V_{cb}^* V_{cd}$ is the oreder of $\mathcal{O}(\lambda^3)$ according to Wolfenstein parameterization. If we could consider only tree contribution, the decay amplitude A and $\bar{A}$ are given by

$$\begin{aligned} A(B^0 \to J/\psi\pi^0) &= V_{cb}^* V_{cd} A_{\rm tree} \\ \bar{A}(B^0 \to J/\psi\pi^0) &= V_{cb}^* V_{cd} A_{\rm tree} \end{aligned} \tag{1.29}$$

because the state of $|J/\psi\pi^0 >$ is CP-even. Then we obtain $\lambda_{J/\psi\pi^0}$ defined in Equation 1.19 as

$$\begin{aligned} \lambda_{J/\psi\pi^0} &= + \frac{\bar{A}(\bar{B}^0 \to J/\psi\pi^0)}{A(B^0 \to J/\psi\pi^0)} \cdot \left(\frac{q}{p}\right) \\ &\simeq - \frac{V_{cb}V_{cd}^*}{V_{cb}^*V_{cd}} \cdot \frac{V_{tb}^*V_{td}}{V_{tb}V_{td}^*} = e^{-2i\phi_1}. \end{aligned} \tag{1.30}$$

Thus, time dependent CP asymmetry is given by

$$a_{J/\psi\pi^0} = -\sin 2\phi_1 \cdot \sin \Delta m t, \tag{1.31}$$

as same as for $B^0 \to J/\psi K_S$ decays, where opposite sign of $a_{J/\psi\pi^0}$ and $a_{J/\psi K_S}$ is due to opposite CP eigenvalue.

On the other hand, as for the penguin contributions, using the unitarity of the CKM matrix, $\sum_{q=u,c,t} V_{qb}^* V_{qd} = 0$, the $A_{\rm P}(B^0 \to J/\psi\pi^0)$ becomes

$$A_{penguin}(B^0 \to J/\psi\pi^0) = V_{tb}^* V_{td}(A^t_{\rm penguin} - A^c_{\rm penguin}) + V_{ub}^* V_{ud}(A^u_{\rm penguin} - A^c_{\rm penguin}). \quad (1.32)$$

In contrast with the $b \to c\bar{c}s$ case, the contribution from the penguin diagrams is not negligible, because both $V_{tb}^* V_{td}$ and $V_{ub}^* V_{ud}$ are approximately the same order in the sine of the Cabibbo angle as contribution of tree amplitude. In this case, time dependent CP asymmetry is given in general formula,

$$a_{J/\psi\pi^0} = \mathcal{S}_{J/\psi\pi^0} \sin\Delta m t + \mathcal{A}_{J/\psi\pi^0} \cos\Delta m t, \quad (1.33)$$

where $\mathcal{S}_{J/\psi\pi^0}$ and $\mathcal{A}_{J/\psi\pi^0}$ are defined as

$$\mathcal{A}_{J/\psi\pi^0} \equiv \frac{|\lambda_{J/\psi\pi^0}|^2 - 1}{|\lambda_{J/\psi\pi^0}|^2 + 1}, \quad (1.34)$$

$$\mathcal{S}_{J/\psi\pi^0} \equiv \frac{2{\rm Im}(\lambda_{J/\psi\pi^0})}{|\lambda_{J/\psi\pi^0}|^2 + 1}, \quad (1.35)$$

respectively.

Therefore, if penguin or other contributions are substantial, a precision measurement of the time-dependent CP asymmetry in $b \to c\bar{c}d$ may reveal values for $\mathcal{S}_{J/\psi\pi^0}$ and $\mathcal{A}_{J/\psi\pi^0}$ that differ from the values for $b \to c\bar{c}s$. Measurements of CP asymmetries in $b \to c\bar{c}d$ transition-induced B decays such as $B^0 \to J/\psi\pi^0$ thus play an important role in probing these non-tree diagrams.

1.5 Principle of the Measurement

At the Belle experiment, B mesons are produced through the $e^+e^- \to \Upsilon(4S) \to B\bar{B}$ process. The mass of $\Upsilon(4S)$, which is a bound state of a b quark and a $\bar{b}$ quark, is 10.58 GeV/c^2. The value is just above the B meson pair production threshold 5.28GeV/$c^2 \times 2 =$ 10.56GeV/c^2. Thus the $\Upsilon(4S)$ meson decays nearly 100% into $B^0\bar{B}^0$ or B^+B^- with almost the same branching fraction. In the Belle experiment, the $B^0\bar{B}^0$ pair is produced with the Lorentz boost of $\beta\gamma = 0.425$ by an asymmetric collision of a positron and an electron with energy of 3.5 GeV and 8 GeV, respectively. Because, to measure time-dependent CP asymmetry parameters, we need to determine the initial flavor of B meson and the decay time. The boosted $B^0\bar{B}^0$ pair has a characteristic feature suitable for these measurement.Because,

A $B^0\bar{B}^0$ pair from $\Upsilon(4S)$ is produced as a C-odd state. Although $B^0 - \bar{B}^0$ oscillation then starts, the state preserves the C-odd configuration and is not allowed to be B^0B^0 or $\bar{B}^0\bar{B}^0$. The time evolution of the pair is given by

$$\begin{aligned} |\Psi(t)\rangle &= e^{-t/\tau_{B^0}}|\Psi(t=0)\rangle, \\ |\Psi(t=0)\rangle &= \frac{1}{\sqrt{2}}[|B^0(\vec{k})\bar{B}^0(-\vec{k})\rangle - |B^0(-\vec{k})\bar{B}^0(\vec{k})\rangle], \end{aligned} \quad (1.36)$$

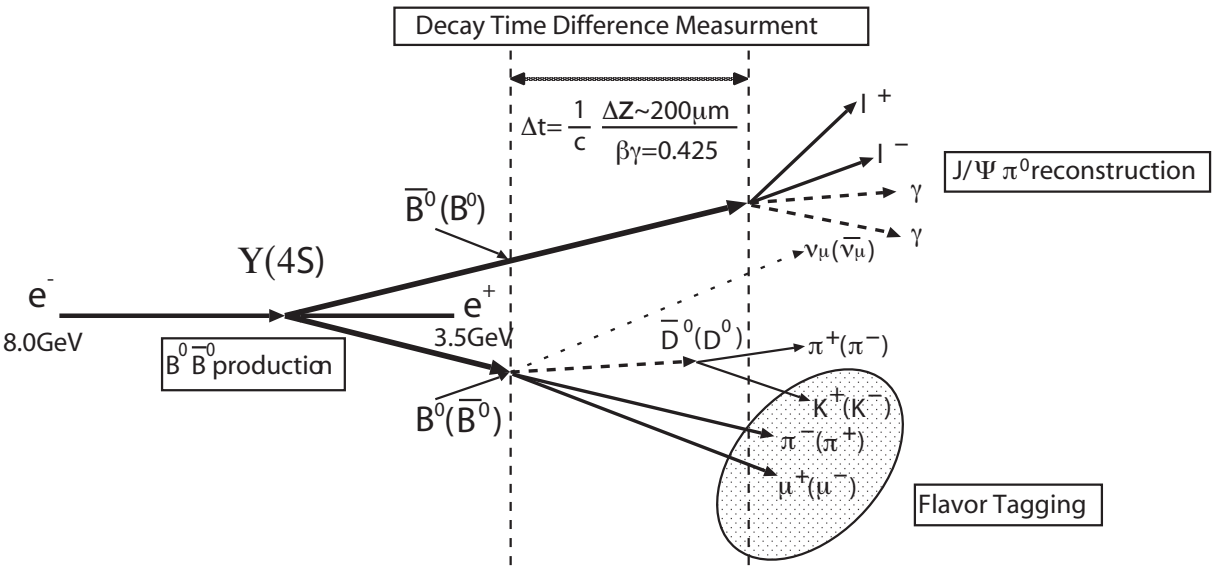

Figure 1.8: *The schematic picture of the experiment.*

where τ_{B^0} is the lifetime of the neutral B meson, and $\vec{k}$ and $-\vec{k}$ are the B mesons' momenta in the $\Upsilon(4S)$ center of mass system. This coherence is preserved until one B meson decays. Hence, if we detect a decay of one of the B meson pair, which we call B_{tag}, and tag its flavor from the decay product at the time t_{tag}, we can determine the flavor of the other B meson, which we call B_{CP}, to be the opposite flavor of B_{tag} at t_{tag}. We then detect B_{CP} decay into $J/\psi\pi^0$ at the time t_{CP} by a probability given by

$$\mathcal{P}(q, \Delta t; \mathcal{A}_{J/\psi\pi^0}, \mathcal{S}_{J/\psi\pi^0}) = \frac{e^{-\frac{|\Delta t|}{\tau_{B^0}}}}{4\tau_{B^0}} \left[1 + q(\mathcal{A}_{J/\psi\pi^0} \cos\Delta m\Delta t + \mathcal{S}_{J/\psi\pi^0} \sin\Delta m\Delta t)\right], \quad (1.37)$$

where $\Delta t \equiv t_{CP} - t_{tag}$ and q denotes the flavor of B_{tag}: $q = +1$ corresponds to $B_{tag} = B^0$ and $q = -1$ corresponds to $B_{tag} = \bar{B}^0$. The CP asymmetry becomes

$$\begin{aligned} a_{J/\psi\pi^0} &= \frac{\mathcal{P}(q=1, \Delta t; \mathcal{A}_{J/\psi\pi^0}, \mathcal{S}_{J/\psi\pi^0}) - \mathcal{P}(q=-1, \Delta t; \mathcal{A}_{J/\psi\pi^0}, \mathcal{S}_{J/\psi\pi^0})}{\mathcal{P}(q=1, \Delta t; \mathcal{A}_{J/\psi\pi^0}, \mathcal{S}_{J/\psi\pi^0}) + \mathcal{P}(q=-1, \Delta t); \mathcal{A}_{J/\psi\pi^0}, \mathcal{S}_{J/\psi\pi^0}} \\ &= \mathcal{A}_{J/\psi\pi^0} \cos\Delta m\Delta t + \mathcal{S}_{J/\psi\pi^0} \sin\Delta m\Delta t. \end{aligned} \quad (1.38)$$

The probability equation (1.37) is normalized in $-\infty < \Delta t < +\infty$.

Considering the discussion above, we have to carry out the following major items:

- Reconstruction of B_{CP} decays into $J/\psi\pi^0$,
- Measurement of decay time difference Δt between B_{CP} and B_{tag},
- Flavor tagging of B_{tag}.

These are shown schematically in Figure 1.8. Since B mesons are nearly at rest in the $\Upsilon(4S)$ center of mass system, they fly along the electron beam direction thanks to the

boost and make decay vertices with an average distance of $\beta\gamma c\tau_{B^0} \sim 200\mu$m. The Δt is determined from the distance to be

$$\Delta t \simeq \frac{z_{CP} - z_{tag}}{\beta\gamma c} \tag{1.39}$$

where the z axis is defined to be anti-parallel to the positron beam direction, z_{CP} is the z position of the B_{CP} decay vertex and z_{tag} is the z position of the B_{tag} decay vertex. We can measure the Δz by using micro-strip silicon detectors with a spatial resolution better than 200μm.

The remaining two items, reconstruction of B_{CP} decays into $J/\psi\pi^0$ and flavor tagging, are described in Chapter 3.

Chapter 2

Experimental Apparatus

The Belle experiment is in operation employing the KEKB accelerator and the Belle detector at the High Energy Accelerator Research Organization (KEK), Tsukuba, Japan. The main physics goal is to test the Kobayashi-Maskawa mechanism of CP violation in B decays. The experiment has started data taking in June, 1999 and has achieved many physics results until now [21]. In this chapter, we briefly describe the KEKB e^+e^- collider and the Belle detector.

2.1 KEKB accelerator

The KEKBis an asymmetric energy e^+e^- collider with the energy of electrons and positrons are 8 GeV and 3.5 GeV, respectively. The center of mass energy is 10.58 GeV, which corresponds to the mass of the $\Upsilon(4S)$ that is the fourth resonance of b and $\bar{b}$ quarks. The $\Upsilon(4S)$ decays nearly 100% into a $B\bar{B}$ meson pair. Figure 2.1 illustrates the configuration of the KEKB. The electrons (positrons) are accelerated to their full energies by the linear accelerator (Linac) and are injected into the HER (LER) of about 3 km circumference. These rings are built side by side in a tunnel 11 m below the ground level. The KEKB has only one interaction point (IP) in the Tsukuba experimental hall, where the electron and positron beams collide at a finite angle of ± 11 mrad to avoid parasitic collisions. To measure CP asymmetry in B decays, KEKB is designed with following special characteristics,

- Asymmetric energy collider
- High luminosity

In the following, we describe these items.

2.1.1 Asymmetric energy collider

KEKB consists of two strage rings for 8 GeV electron and 3.5 GeV positron. To measure CP asymmetry, we have to determine the decay time difference of B^0 and $\overline{B}^0$, Δt, as described in Section 1.5. However, B meson lifetime (~ 1.6 ps) is too short to determine Δt directly.

If electron and positron collide with the same energy, B meson which is decayed from $\Upsilon(4S)$ is almost at rest and its flight length is only 20 μm. While, the produced B meson

is boosted due to the asymmetric energy with a Lorentz factor $\beta\gamma \simeq 0.425$ and fly about 200 μm on average along the electron beam direction. Thus, Δt can be determined with enough resulution.

2.1.2 High luminosity

Luminosity $\mathcal{L}$ represents beam intensity parameter defined as $R = \mathcal{L}\sigma$, where σ and R is cross section and interaction frequency. The branching fractions of B decays used for CP asymmetry measurements are order $10^{-4} \sim 10^{-6}$. Thus, KEKB is designed to achieve high luminosity, $10 \times 10^{33}\mathrm{cm}^{-2}\mathrm{s}^{-1}$ which corresponds to 10^8 $B\bar{B}$ pairs a year.

The $\mathcal{L}$ can be expressed as

$$\mathcal{L} = 2.2 \times 10^{34} \xi (1 + r) \left(\frac{E \cdot I}{\beta_y^*} \right)_{\pm} \tag{2.1}$$

E	:	beam energy [GeV]
I	:	circulating current [A]
ξ	:	beam-beam tune shift parameter (this parameter reflects the strength of the beam-beam collision)
r	:	aspect ratio of the beam shape (1 for a round and 0 for a flat beam)
β_y^*	:	vertical beta function at interaction point [cm]

where - and + sign represent electron and positron case, respectively. Each ring can store at most 5000 bunches, which are clusters of a few hundred billion electrons (positrons). The main parameters of the KEKB are summarized in Table 2.1. Until July 2003, the KEKB has achieved the world recored peak luminosity of $10.567 \times 10^{33}\mathrm{cm}^{-2}\mathrm{s}^{-1}$ and data recorded by the Belle detector correspond to the integrated luminosity of 140 fb^{-1}.

2.2 The Belle Detector

The Belle detector surrounds the IP to catch particles produced by the e^+e^- collisions. To measure time-dependent CP asymmetry, it is required that we fully reconstrut CP eigenstate decays efficiently, determine decay time difference and identify charged particle ($e^{\pm}, \mu^{\pm}, \pi^{\pm}$ and $K^{\pm}$) for the flavor tagging. The Belle detector is designed to satisfy those requirements.

Figure 2.2 and 2.3 shows the detector configuration. The B meson vertices are measured by the silicon vertex detector (SVD) situated just outside of a cylindrical beryllium beam pipe. Charged particle tracking is performed by the central drift chamber. Particle identification is provided by dE/dx measurements in CDC, aerogel Čherencov counter (ACC), and time-of-flight counter (TOF) placed radially outside of CDC. Electromagnetic showers, which are used to identify photons and electrons, are detected in an array of CsI(Tl) crystals (ECL) located inside the solenoid coil. The super-conducting solenoid provide a magnetic field of 1.5 T for momentum measurement of charged particles by CDC. Muons and K_L mesons are identified by arrays of resistive plate counters interspersed in the iron yoke (KLM). In addition to these sub-detectors, the Belle detector

Table 2.1: *Main parameters of KEKB.*

Ring		LER	HER	
Energy	E	3.5	8.0	GeV
Circumference	C	3016.26		m
Luminosity	$\mathcal{L}$	1×10^{34}		$\mathrm{cm}^{-2}\mathrm{s}^{-1}$
Crossing angle	θ_x	± 11		mrad
Tune shifts	ξ_x/ξ_y	0.039/0.052		
Beta function at IP	β_x^*/β_y^*	0.33/0.01		m
Beam current	I	2.6	1.1	A
Natural bunch length	σ_z	0.4		cm
Energy spread	σ_ε	7.1×10^{-4}	6.7×10^{-4}	
Bunch spacing	s_b	0.59		m
Particle/bunch	N	3.3×10^{10}	1.4×10^{10}	
Emittance	$\varepsilon_x/\varepsilon_y$	$1.8 \times 10^{-8}/3.6 \times 10^{-10}$		m
Synchrotron tune	ν_s	$0.01 \sim 0.02$		
Betatron tune	ν_x/ν_y	45.52/45.08	47.52/43.08	
Momentum compaction factor	α_p	$1 \times 10^{-4} \sim 2 \times 10^{-4}$		
Energy loss/turn	U_o	0.81†/1.5‡	3.5	MeV
RF voltage	V_c	$5 \sim 10$	$10 \sim 20$	MV
RF frequency	f_{RF}	508.887		MHz
Harmonic number	h	5120		
Longitudinal damping time	τ_ε	43†/23‡	23	ms
Total beam power	P_b	2.7†/4.5‡	4.0	MW
Radiation power	P_{SR}	2.1†/4.0‡	3.8	MW
HOM power	P_{HOM}	0.57	0.15	MW
Bending radius	ρ	16.3	104.5	m
Length of bending magnet	ℓ_B	0.915	5.86	m

†: without wigglers, ‡: with wigglers

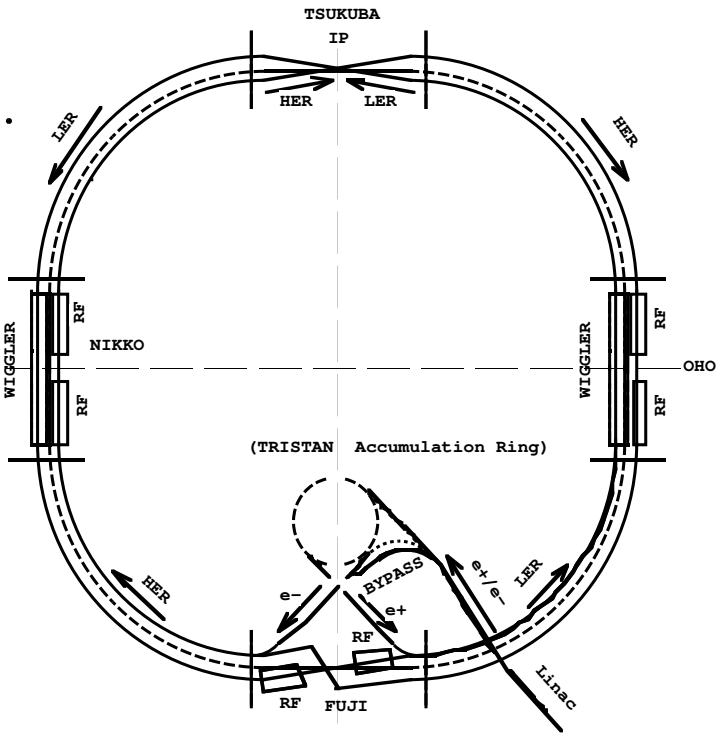

Figure 2.1: *Configuration of the KEKB collider.*

has extreme forward calorimeter (EFC) to improve the experimental sensitivity to some physics processes such as $B \to \tau\nu$. The detector performance is summarized in Table 2.2.

Figure 2.4 illustrates the Belle coordinate system which is defined as:

- x: horizontal, outward to the KEKB ring,
- y: vertical, upward,
- z: opposite of the positron beam direction,
- r: $\sqrt{x^2 + y^2}$,
- θ: the polar angle from z axis,
- and ϕ: the azimuth angle around z axis.

The detailed description of the Belle detector is found in the reference[22]. We give the brief description of the major detector subsystems.software relevant to the measurement of CP asymmetry parameters.

2.2.1 Beam Pipe

The beam pipe is designed to minimize its thickness to reduce multiple coulomb scattering which deteoriate the vertex resolution. Figure 2.5 shows the cross section of the beryllium beam pipe at the interaction region. The beam pipe consists of two cylinders with different radii, the inner is 20.0 mm and the outer is 23.0 mm. Each cylinder have 0.5 mm thickness.

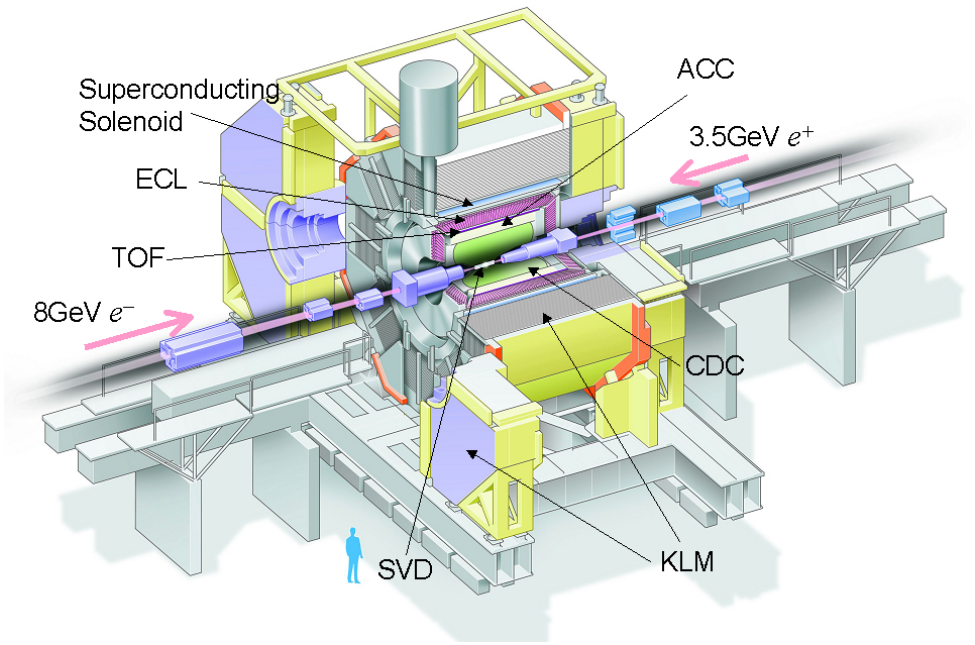

Figure 2.2: *Configuration of the Belle detector system.*

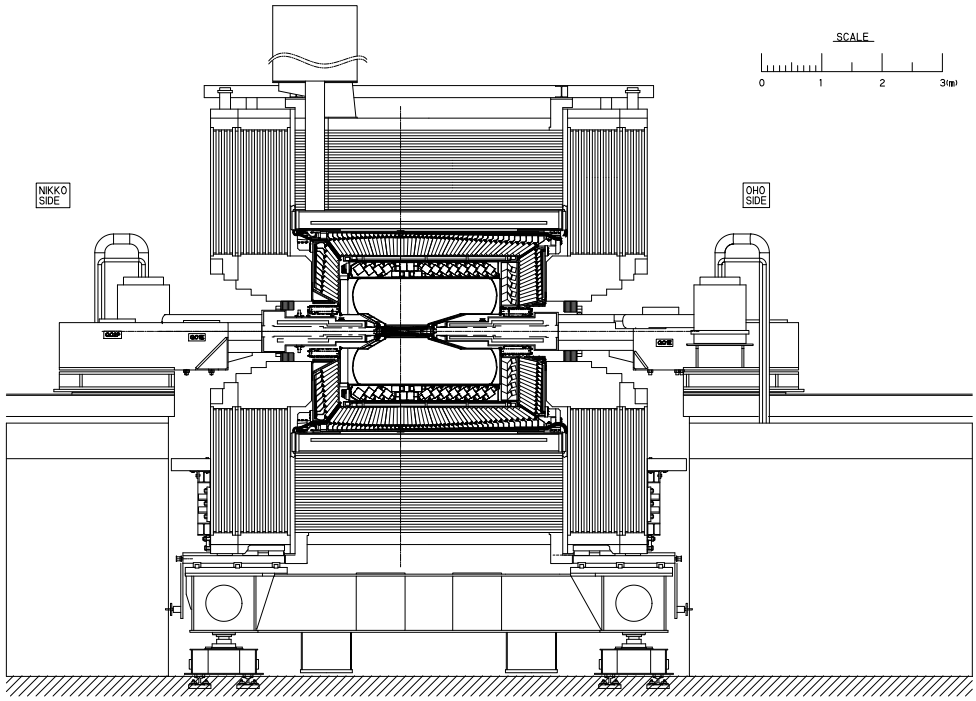

Figure 2.3: *Side view of the Belle detector.*

Detector	Type	Configuration	Readout	Performance
	Beryllium	Cylindrical, r=2.0 cm		He gas cooled
Beam pipe	double-wall	0.5/2.5/0.5(mm)=Be/He/Be		
	Double	300 μm-thick, 3 layers	ϕ : 40.96k	$\sigma_{\Delta z}$ ~200 μm
SVD	sided	r = 3.0 - 6.05 cm	z : 40.96k	
	Si strip	Length = 22 - 34 cm		
	Small cell	Anode: 50 layers	A: 8.4 K	$\sigma_{r\phi} = 130$ μm
CDC	drift	Cathode: 3 layers	C: 1.5 K	$\sigma_z \lesssim 200 \sim 1,400 \mu$m
	chamber	r = 8.3 - 86.3 cm		$\sigma_{p_t}/p_t = 0.3\% \sqrt{p_t^2 + 1}$
		-77$\leq z \leq$ 160 cm		$\sigma_{dE/dx} = 6\%$
	n : 1.01	~12×12×12 cm^3 blocks		$N_{p.e.} \geq 6$
ACC	$\sim$ 1.03	960 barrel		K/π separtation :
	Silica	/ 228 endcap		1.2<p<3.5GeV/c
	aerogel	FM-PMT readout	1,788	
TOF	Scintillator	128 ϕ segmentation	128×2	$\sigma_t = 100$ ps
		r = 120 cm, 3 m-long		K/π separation :
TSC		64 ϕ segmentation	64	up to 1.2GeV/c
	CsI	Barrel : r = 125 - 162 cm	6,624	σ_E/E= 1.3 %/$\sqrt{E}$
ECL	(Towered-	End-cap : z =	1152 (F)	$\sigma_{pos} = 0.5$ cm/$\sqrt{E}$
	structure)	-102 cm and +196 cm	960 (B)	
Magnet	Super	inner radious = 170 cm		B = 1.5 T
	conducting			
	Resistive	14 layers	θ:16 K	$\Delta\phi$=$\Delta\theta$=30 mrad
KLM	plate	(5cm Fe+4cm gap)	ϕ:16 K	for K_L
	counters	2 RPCs in each gap		$\sim$ 1 % hadron fake
EFC	BGO	2×1.5×12 cm^3	θ:5	σ_E/E=
			ϕ:32	$(0.3 \sim 1)\%/\sqrt{E}$

Table 2.2: *Performance parameters expected (or achieved) for the Belle detectror (p_t in* GeV/c*, E in GeV).*

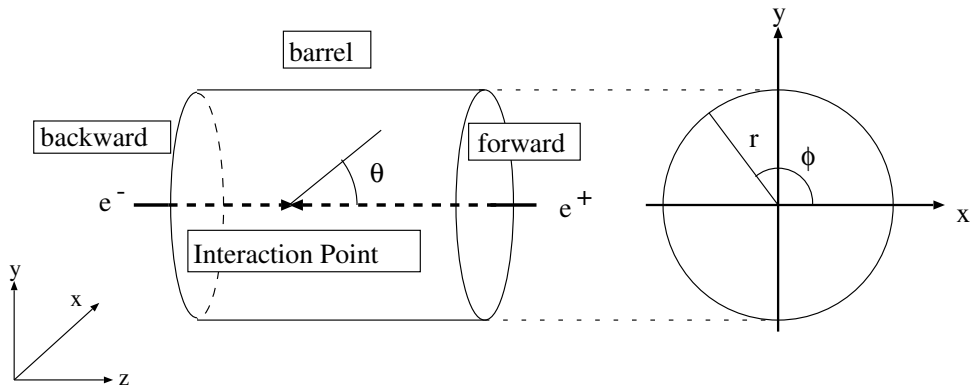

Figure 2.4: *Definition of the coordinate system.*

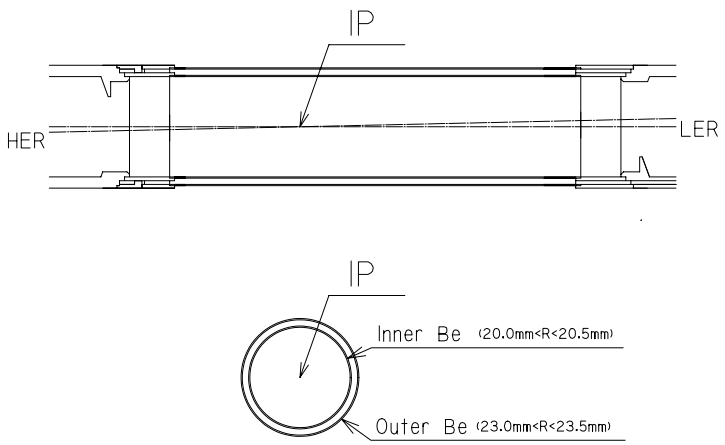

Figure 2.5: *The cross secton of the beryllium beam pipe at the interaction point.*

A 2.5 mm gap between the cylinders provides a channel for cooling a beam-induced heating. Helium gas is used as a coolant in order to minimize the material in the beam pipe. Outside the outer beryllium cylinder, a 20 μm thick gold sheet is attached in order to reduce the low energy photon background from the HER. The total thickness of the beam pipe corresponds to 0.9% of a radiation length.

2.2.2 Silicon Vertex Detector(SVD)

SVD detect the B meson vertex position which is essential for the measurement of time-dependent CP asymmetry parameters.

Figure 2.6 shows the geometrical configuration of SVD. SVD consists of three concentric cylindrical layers of silicon sensors and covers a polar angle $23^\circ < \theta < 139^\circ$. This corresponds to 86% of the full solid angle in the $\Upsilon(4S)$ rest frame. The radii of the three layers are 30, 45.5 and 60.5 mm. The three layers are constructed from 8, 10 and 14 ladders. Each ladder is made up of two long or short half ladders that are mechani-

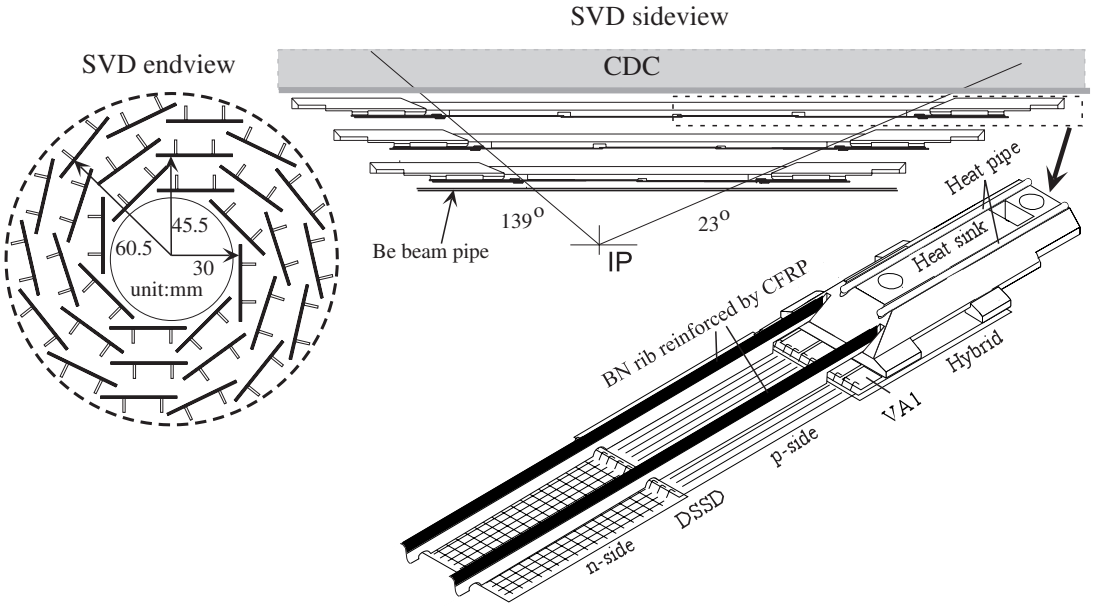

Figure 2.6: *Detector configuration of SVD.*

cally jointed by a support structure but electrically independent of each other. Each long half-ladder contains two double-sided silicon strip detectors (DSSDs) and a hybrid unit. Each short half-ladder contains a DSSD and a hybrid unit. The innermost layer ladder consists of two short half-ladders. The middle layer ladder consists of a short and a long half-ladder. The outermost layer ladder consists of two long half-ladders.

We use S6936 DSSDs fabricated by Hamamatsu Photonics, which were originally developed for the DELPHI[23]. The size of DSSD is 57.5×33.5 mm^2 with thickness of 300 μm. The schematic view of DSSD is shown in Figure 2.7. One side (n-side) of DSSD has n^+ strips oriented perpendicular to the beam direction to measure the z coordinate. The other side (p-side) with longitudinal p^+ strips allows the ϕ coordinate measurement. The n^+-strips are interleaved by p^+ implants, which are called p stops, to separate the consecutive strips electrically. The bias voltage of 75V is supplied to the n-side, while p-side is grounded. A charged particle passing through the depletion region of the n bulk silicon generates pairs of electron and hole. The electrons and holes drift to each strip and make two dimensional hit signals. The strip pitch is 25 μm for p-side and 42 μm for n-side. On the n-side, adjacent strips are read out by a single channel. This gives an effective strip pitch of 84 μm. On the p-side, every other strip is connected to a readout channel. Charge collected by the floating strips in between is read from adjacent strips by means of capacitive charge division. The signal of DSSDs are read out by VA1 chips[24, 25]. The VA1 chip is a 128 channel CMOS integrated circuit fabricated in the Austrian Micro Systems (AMS). Five VA1 chips are on both side of each hybrid unit. A total number of readout channels is 81,920.

The performance of SVD is parameterized by the SVD-CDC track matching efficiency and the impact parameter resolution of tracks with associated SVD hits. The SVD-CDC track matching efficiency is defined as the probability that a CDC track within the SVD acceptance has associated SVD hits in at least two layers, and in at least one layer with both the r-ϕ and r-z information. Figure 2.8 shows the SVD-CDC track matching

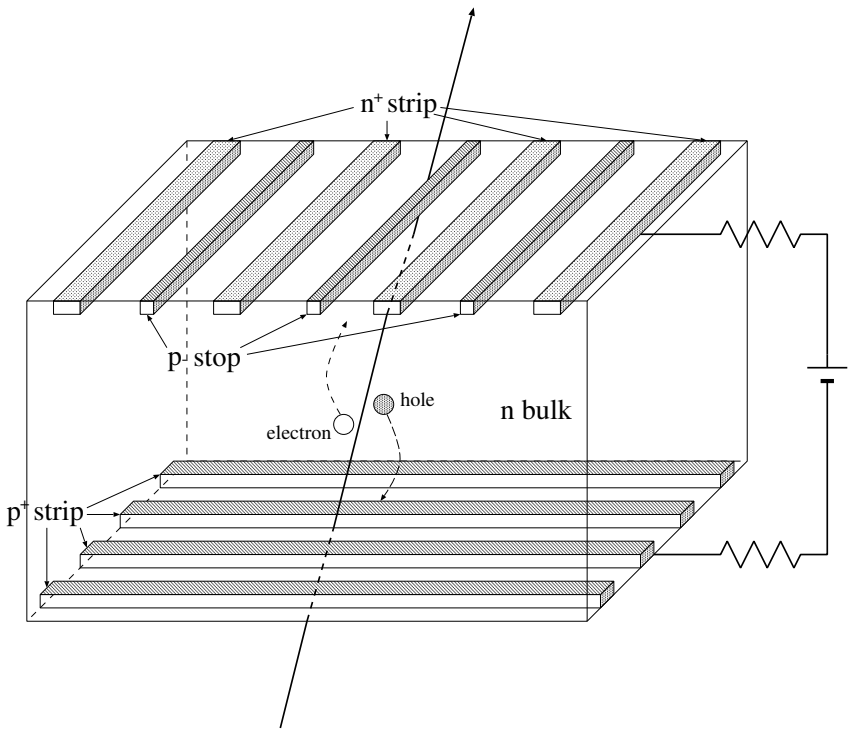

Figure 2.7: *Schematic drawing of the DSSD.*

efficiency for hadronic events as a function of time. The average matching efficiency is better than 98.7%, although we observe slight degradation after one year operation as a result of the gain loss of VA1 from radiation damage[26]. The momentum and angular dependence of the impact prameter resolution are shown in Figure 2.9. They are well represented by the following formula: $\sigma_{xy} = 19 \oplus 50/(p\beta \sin^{3/2}\theta)$ μm and $\sigma_z = 36 \oplus 42/(p\beta \sin^{5/2}\theta)$ μm, where "$\oplus$" indicates a quadratic sum.

2.2.3 Central Drift Chamber(CDC)

The main role of Central Drift Chamber(CDC) is detection of charged particle tracks and reconstruction of their momenta from their curvature in the magnetic field of 1.5 T provided by the superconducting solenoid. CDC also provides particle identification information in the form of dE/dx measurements for charged particles.

The structure of CDC is shown in Figure 2.10. The length is 2,400 mm, and the inner and outer radii are 83 and 874 mm, respectively. The polar angle coverage is $17° \leq \theta \leq 150°$. CDC is a small cell drift chamber containing a total of 50 anode sense wire layers (32 axial wire layers and 18 stereo wire layers) and 3 cathode strip layers. The axial wires are configured to be parallel to z axis, while the stereo wires are slanted by approximately ± 50 mrad. The three dimensional information is provided by this wire configuration. Eight field wires surround a sense wire to provide drift electric field, and the field wires and a sense wire form a drift cell. The cell structure is shown in Figure 2.11. CDC has 8,400 drift cells. A mixture of helium (50%) and ethane (50%) gas is filled in the chamber with atmospheric pressure. A charged particle passing through CDC ionizes the gas. The electrons, liberated from the ionized gas, drift to a sense wire with a specific

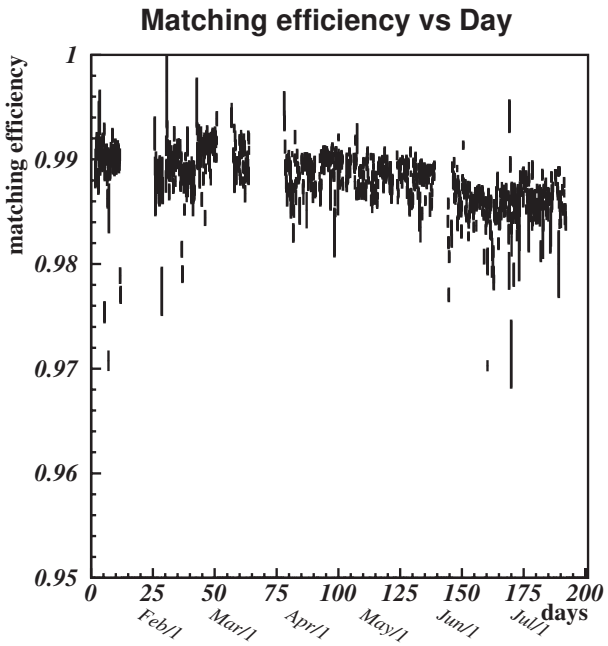

Figure 2.8: *SVD-CDC track matching efficiency as a function of the date of data taking.*

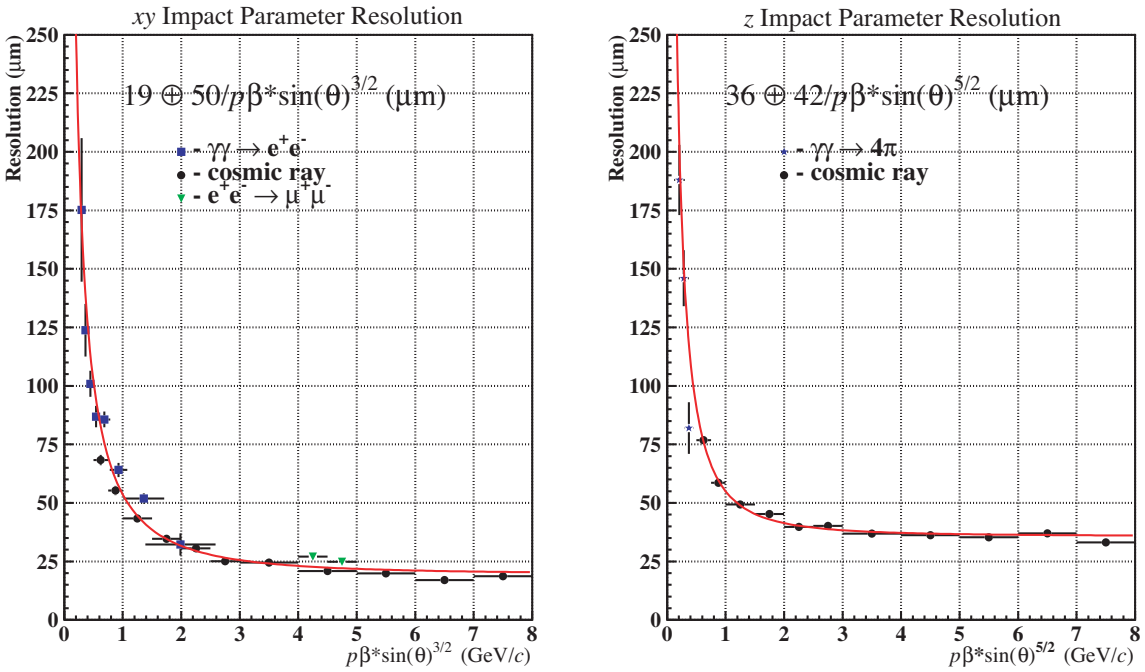

Figure 2.9: *Impact parameter resolution of charged tracks with associated SVD hits.*

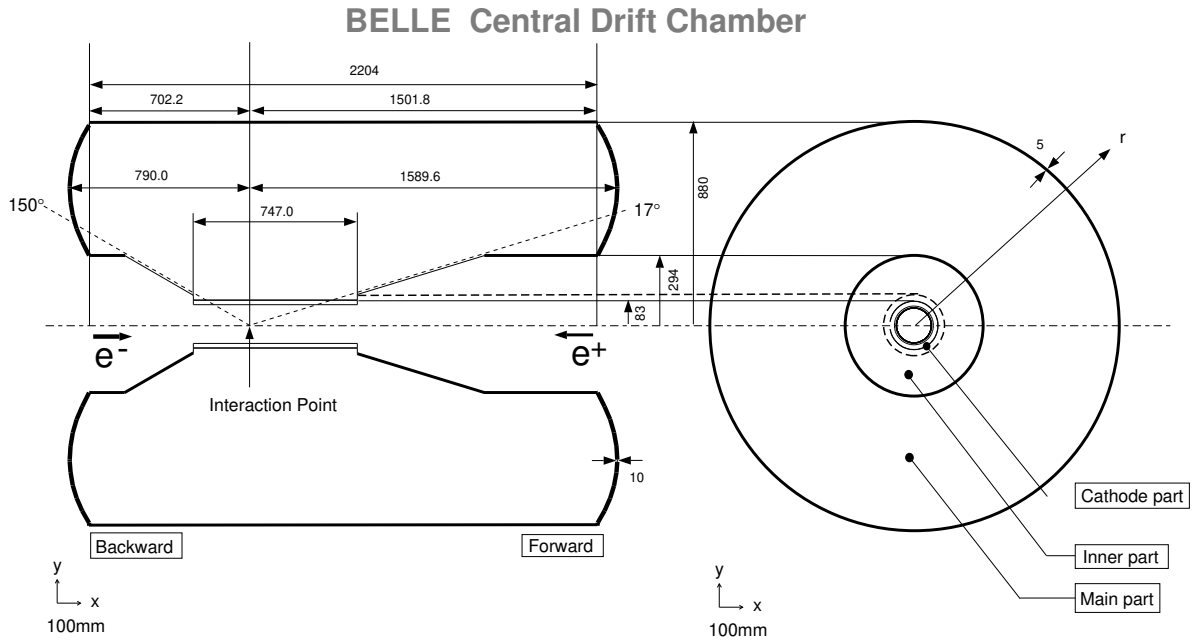

Figure 2.10: *Overview of the CDC structure. The lengths in the figure are in units of mm.*

drift velocity and cause charge avalanches, then the measured signal height and the drift time provides information of the energy deposit and the distance from the sense wire. In the innermost radii, the three cathode strip layers are installed to provide the z position measurements of tracks for the trigger system. The number of readout channel is 8,400 for anode sence wires and 1,792 for cathode strips.

Figure 2.12 shows the transverse momentum resolution (p_t) resolution as a function of p_t. The p_t resolution is $(0.20p_t \oplus 0.29)\%$, where p_t is in unit of GeV/c. Figure 2.13 shows a scatter plot of measured dE/dx and particle momentum. Populations of pions, kaons, protons and electrons are clearly seen. Figure 2.14 shows the distribution of dE/dx for minimum ionizing particles measured with pions from K_S decays. The dE/dx resolution is measured to be 7.8%

2.2.4 Aerogel Čherenkov Counter(ACC)

The aerogel Čherenkov counter (ACC) provides separation between $K^{\pm}$ and $\pi^{\pm}$ with momentum ranged from 1.2 GeV/c to 3.5 GeV/c.

ACC detects if the particle emit Čherenkov light or not and distinguishes particle species. A charged particle passing through a matter emit Čherenkov light if its velocity is larger than the light velocity in the matter. The condition to emit Čhrenkov light is written as

$$m < p\sqrt{n^2 - 1}, \tag{2.2}$$

where m and p are the particle mass and the momentum and n is the refractive index of the matter.

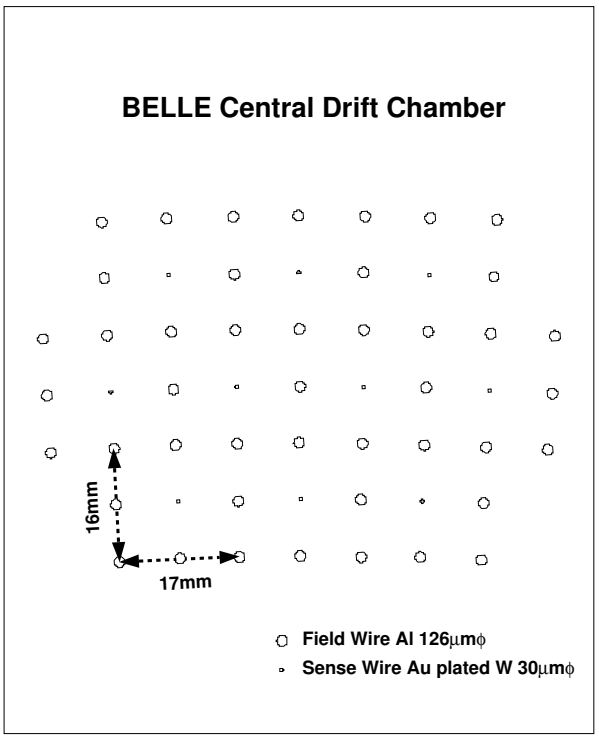

Figure 2.11: *Cell structure of CDC.*

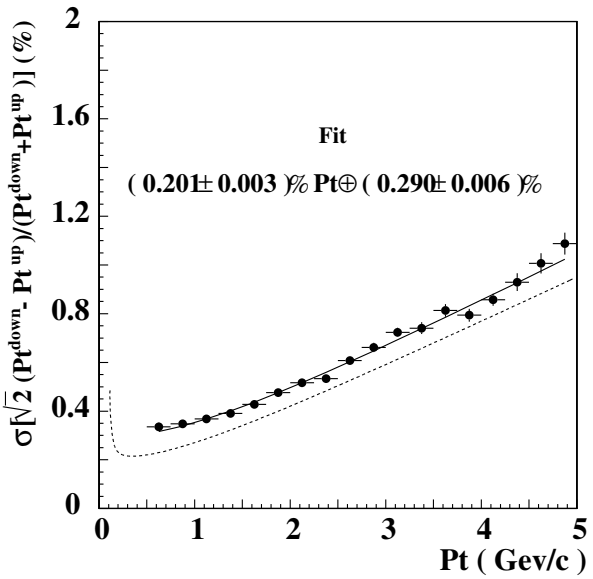

Figure 2.12: *The p_t resolution is a function of p_t itself. The solid curve shows the fitted result ($0.201\%p_t \oplus 0.290\%/\beta$) and the dotted curve shows the ideal expectation for $\beta = 1$ particles.*

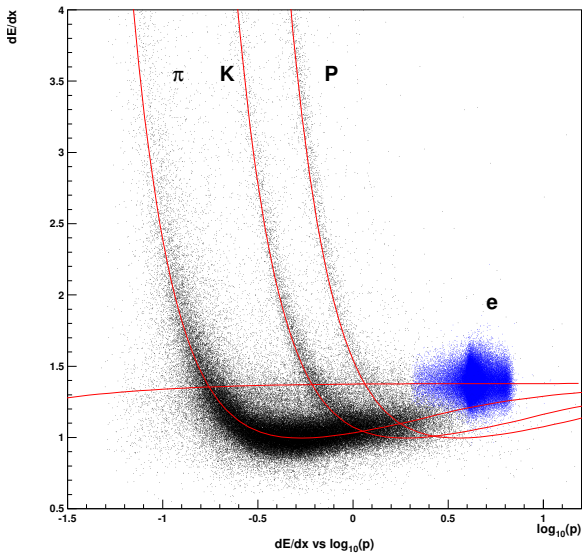

Figure 2.13: *The measured dE/dx versus momentum observed in collision data.*

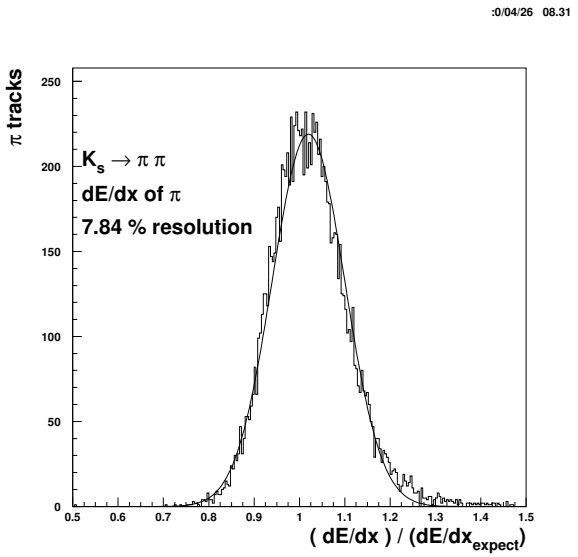

Figure 2.14: *Distribution of $(dE/dx)/(dE/dx_{exp})$ for pions from K^0_S decays,where (dE/dx) is the measured specific ionization and (dE/dx_{exp}) is the expectation by Bethe-Bloch formula.*

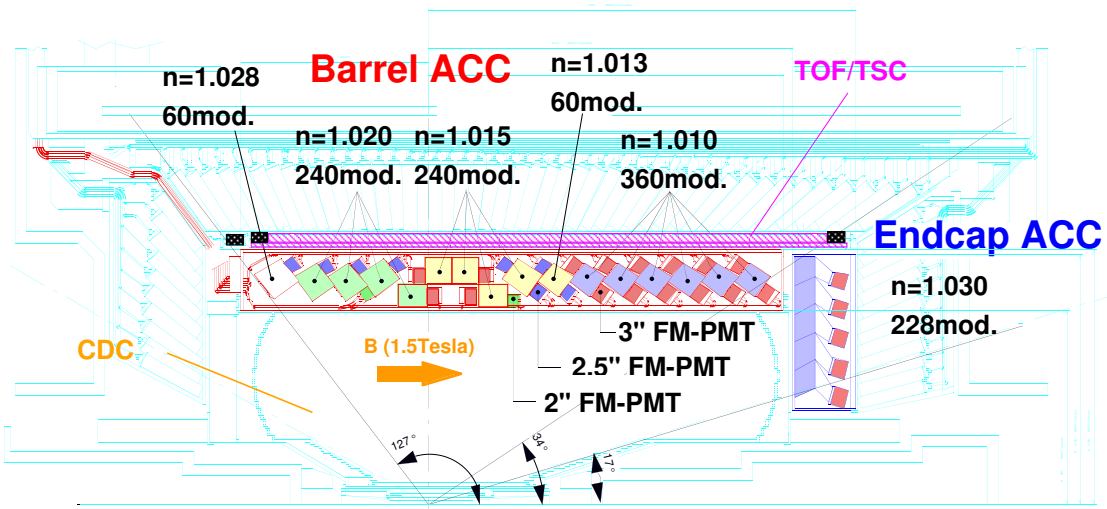

Figure 2.15: *The arrangement of ACC.*

Figure 2.15 shows the configuration of ACC. ACC consists of 960 counter modules segmented into 60 cells in the ϕ direction for the barrel part and 228 modules arranged in 5 concentric layers for the forward endcap part of the detector. Each counter module consists of a block of silica aerogel in an aluminum box of 0.2 mm thickness and one or two fine-mesh type photomultiplier tubes (FM-PMTs) which can work in the 1.5 T magnetic field. The silica aerogel with five different refractive indices, $n = 1.010, 1.013, 1.015, 1.020$ and 1.028 are used for the barrel modules depending on the polar angle. The refractive indices are selected to cover up to the maximum momentum of two body B decays. For the endcap module, the silica aerogel with $n = 1.030$ is used for low momentum particles, which is necessary for flavor tagging, to cover lack of TOF in the endcap. The number of readout channel is 1,560 for the barrel modules and 228 for the endcap modules.

Figure 2.16 shows measured pulse height distributions for barrel ACC for $e^{\pm}$ tracks in Bhabha events and $K^{\pm}$ candidates in hadronic events, where $K^{\pm}$ candidates are selected by TOF and dE/dx measurements, together with the expectations from Monte Carlo simulation. Clear separation between $K^{\pm}$ and $e^{\pm}$ is seen.

2.2.5 Time of Flight Counter(TOF)

Time of flight counter (TOF) detector system using plastic scintillation counters is used to distinguish $K^{\pm}$ from $\pi^{\pm}$ up to 1.2 GeV/c. TOF measures the elapsed time between a collision at the interaction point and the time when the particle hits the TOF layer. A

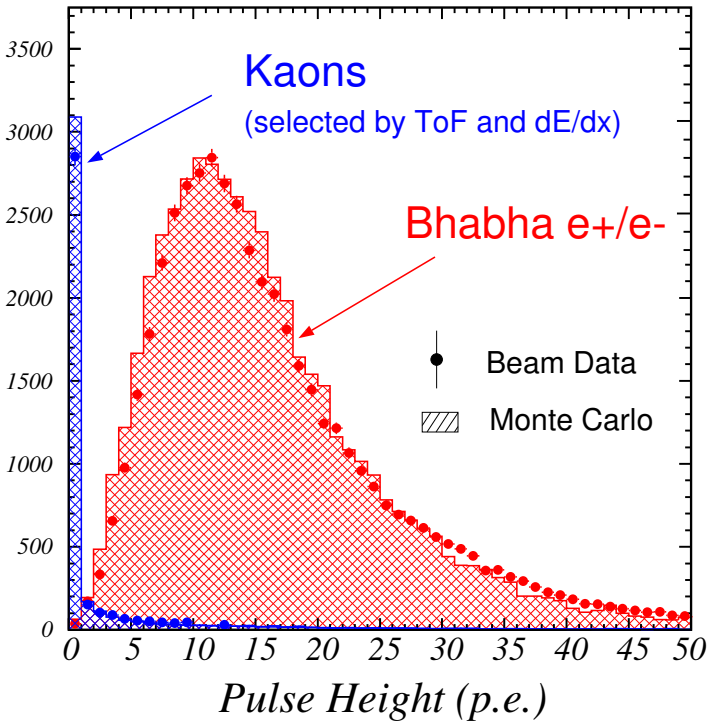

Figure 2.16: *Pulse-height spectra in units of photoelectrons observed by barrel ACC for electrons and kaons.*

relation between measured time T and the particle mass m is expressed as

$$m = p\sqrt{\frac{c^2T^2}{L^2} - 1}, \tag{2.3}$$

where p is the particle momentum and L is the flight path length. For $K^{\pm}$ and $\pi^{\pm}$ with a momentum of 1.2 GeV/c and a flight path length of 1.2 m, which is the distance between the interaction point and TOF, give T of 4.3 ns and 4.0 ns, respectively. TOF is designed to have 100 ps time resolution which separate these $K^{\pm}$ and $\pi^{\pm}$ by 3 σ significance. In addition to particle identification, TOF provide fast timing signals for the trigger system. To sustain the fast trigger rate in any beam background condition, the thin trigger scintillation counters (TSC) is appended just inside the TOF counter.

TOF system consists of 128 TOF counters and 64 TSCs. Two trapezoidally shaped TOF counters and one TSC counter form one module. Figure 2.17 shows the configuration of a TOF/TSC module. In total 64 TOF/TSC modules located at a radius of 1.2 m from the interaction point cover a polar angle ranged from 34° to 120°. Each TOF counter is read out by a FM-PMT at each end. Each TSC counter is read out by only one FM-PMT from the backward end. The total number of readout channels is 256 for TOF and 64 for TSC.

Figure 2.18 shows TOF time resolution for forward and backward PMTs and for the weighted average as a function of z position in TOF module measured by μ-pair events. The resolution for the weighted average time is about 100 ps with a small z dependence. Figure 2.19 shows the mass distribution obtained from TOF measurement. Clear peaks corresponding to $\pi^{\pm}$, $K^{\pm}$ and protons are seen. The data points are in good agreement

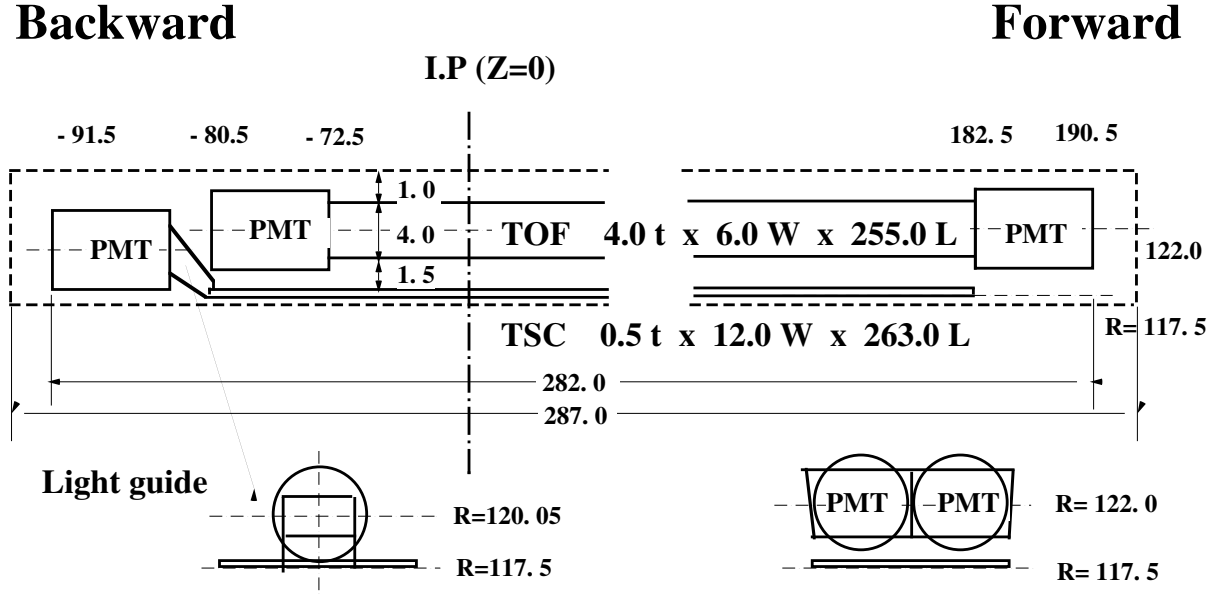

Figure 2.17: *Dimensions of a TOF/TSC module.*

with the Monte Carlo expectation assuming time resolution of 100 ps (histogram).

2.2.6 Electromagnetic Calorimeter(ECL)

The main purpose of the electromagnetic calorimeter (ECL) is the detection of electrons and photons from B meson decays with high efficiency and good energy and position resolutions. For our analysis, ECL plays important roles in π^0 and J/ψ reconstruction and flavor tagging. Electron identification relies primarily on a comparison of the charged particle track momentum and the its energy deposit in ECL, as described in Section 2.4.2. Electrons deposit most of its energy in the ECL by electromagnetic shower, while hadrons or $\mu^{\pm}$ deposit small fraction of their energies. Thus, good energy resolution of ECL is indispensable for hadron rejection. To additional to this, since approximately one third of the final-state particle in B meson decays are neutral pions, it is essential to have high quality photon detection. Most of these photons are end-products of decay cascade, and they have relatively low energy and, thus, good performance below 500 MeV is especially important. On the other hand, for interesting two-body decay mode such as $B^0 \to K^*\gamma$ and $B^0 \to \pi^0\pi^0$, photon's energy ranges up to 4 GeV. Furthermore, photons or electrons coming from Bhabha events have energies up to 8 GeV. Therefore, the ECL is designed to provide good sensitivity of photons in the range from 500 MeV up to 8 GeV. The ECL is also required the separation of two nearby photons and a precise determination of their opening angle for high momentum π^0.

The overall configuration of the ECL is shown in Figure 2.20. ECL consists of 8,736 thallium doped CsI crystal counters, and the total weight is 43 tons. The calorimeter covers the polar angle region of 17° and 150°, corresponding to a total solid-angle coverage of 91 % of 4π. The barrel part has 6,624 crystals segmented 46 in θ and 144 in ϕ. The forward (backward) endcap has 1,152 (960) crystals segmented 13 (10) in θ and 48-144 (64-144) in ϕ depending on θ. Small gaps between the barrel and endcap crystals provide

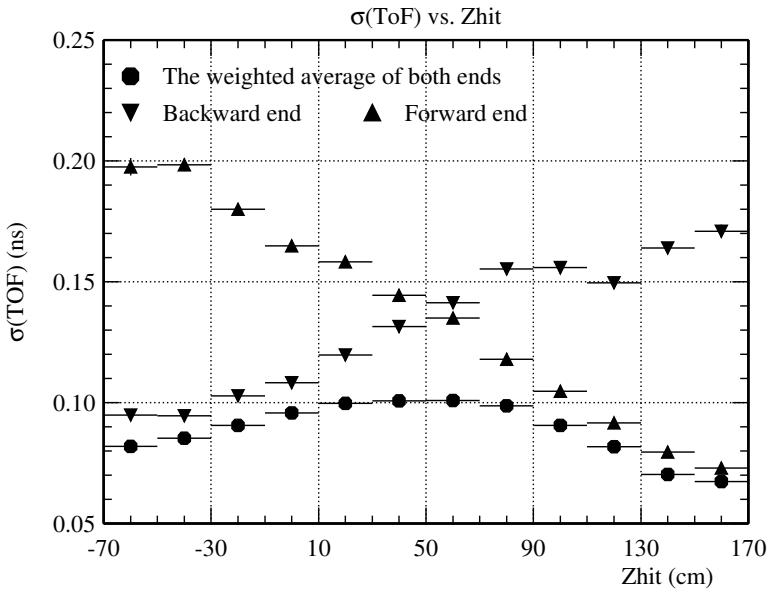

Figure 2.18: *Time resolution for μ-pair events.*

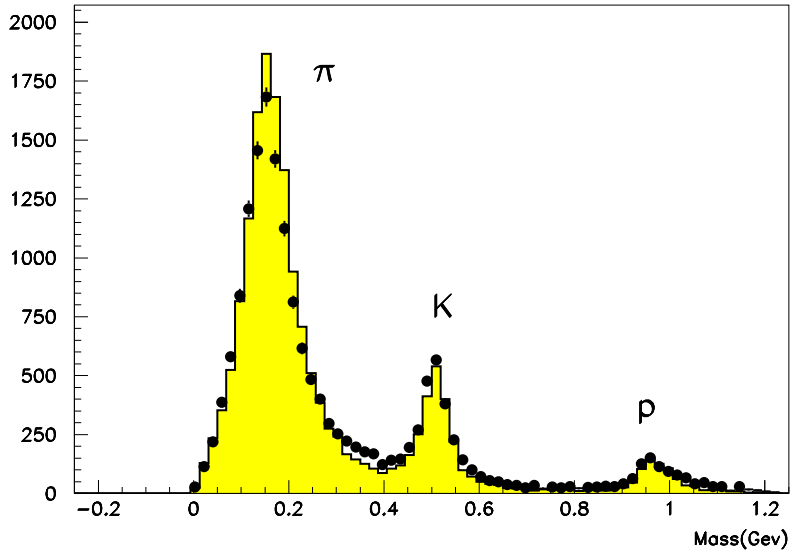

Figure 2.19: *Mass distribution from TOF measurement for particle momenta below 1.2GeV/c. Histogram shows the Monte Carlo expectation assuming time resolution of 100 ps. The points with error bars are data.*

a path way for cables. The loss of solid angle associated with these gaps is approximately 3% of the total acceptance.

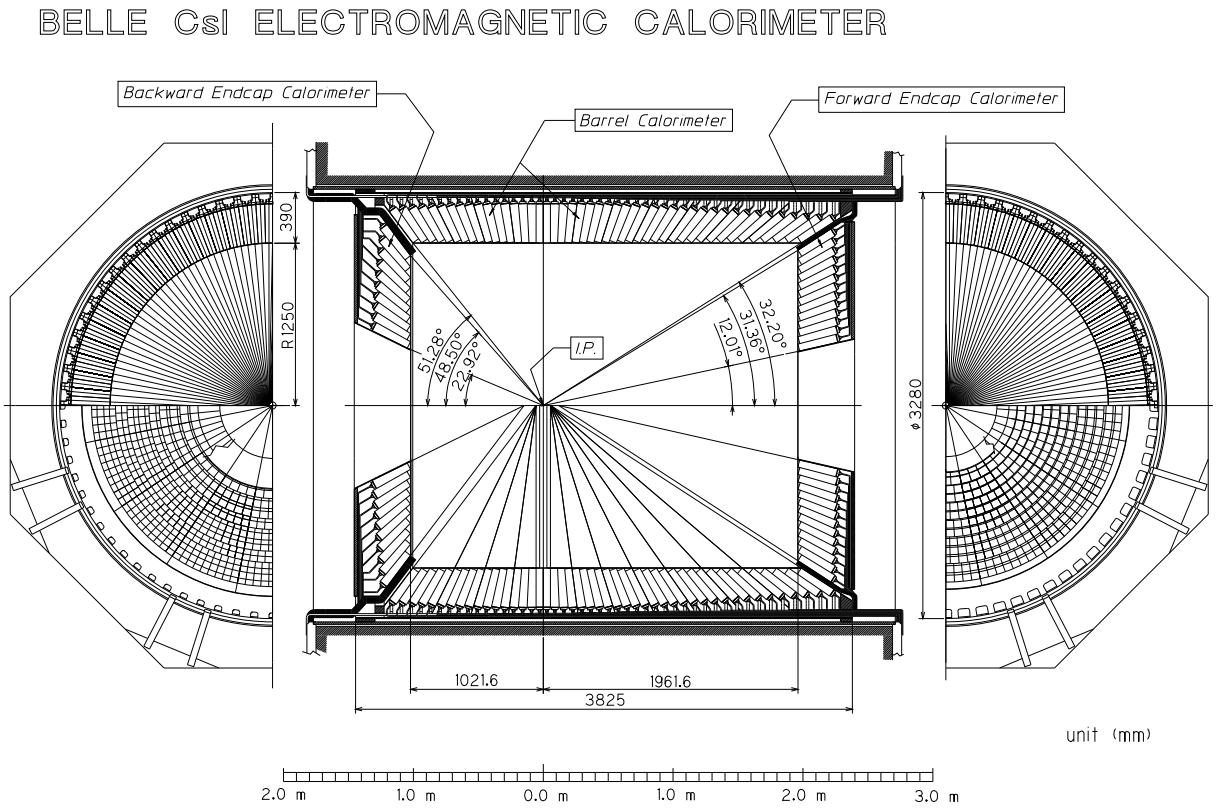

Figure 2.20: *Configuration of ECL.*

Each CsI(Tl) crystal has a tower-like shape as shown in Figure 2.21. Typical size of a crystal is 30 cm long, 5.5 cm × 5.5 cm in the front face, and 6.5 cm × 6.5 cm in the rear face, respectively. The length corresponds to 16.2 radiation lengths. According to Monte Calro simulation, approximately 80% of the total energy deposited by a photon injected at the center of the front face of the crystal is contained in that crystal. A single CsI(Tl) counter is assembled as indicated in Figure 2.22. All sides of the crystal except for the end face for light readout are covered by a single layer of 200 μm thick teflon. it is then coverd be a 25 μm thick layer of aluminaized mylar for light and electrical shielding. Two photodiodes, each having an active area of 10 mm × 20 mm, are glued at the center of crystal end surface via an acrylite plate of 1 mm thickness.

A block diagram of read out system is shown in Figure 2.23. Each counter has two photodiodes and preamplifiers attached at the end of the crystal in order to read out scintillation. The preamplifier output is transmitted to a shaping circuit where the two signals from the same crystal are summed. Then, the summed signal is split into two streams: one is for the signal to measure energy and the other is for the trigger signal with 200 ns shaping time.

The energy resolution is measured with the beam test before installation into the Belle structure to be $\sigma_E/E = 1.34 \oplus 0.066/E \oplus 0.81/E^{1/4}$ %, where E in GeV. The position resolution is $0.27 + 3.4/E^{1/2} + 1.8/E^{1/4}$ mm. Figure 2.24 show the energy resolution and

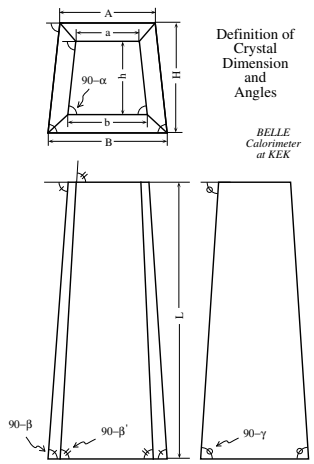

Figure 2.21: *The CsI(Tl) crystal shape.*

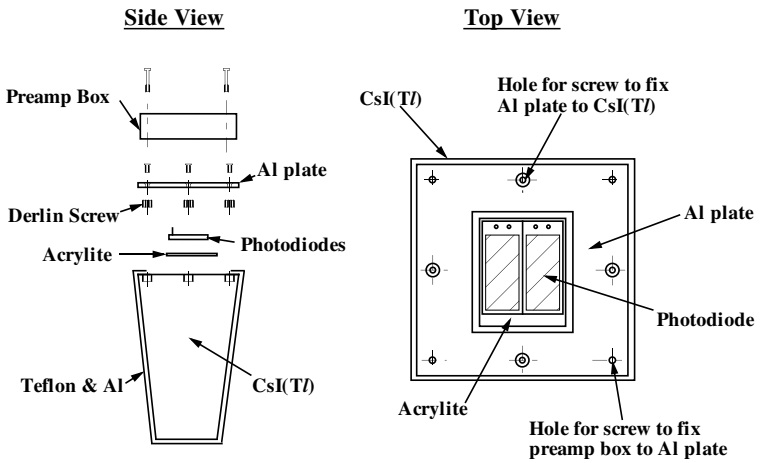

Figure 2.22: *The mechanical assembly of the CsI(Tl) counter.*

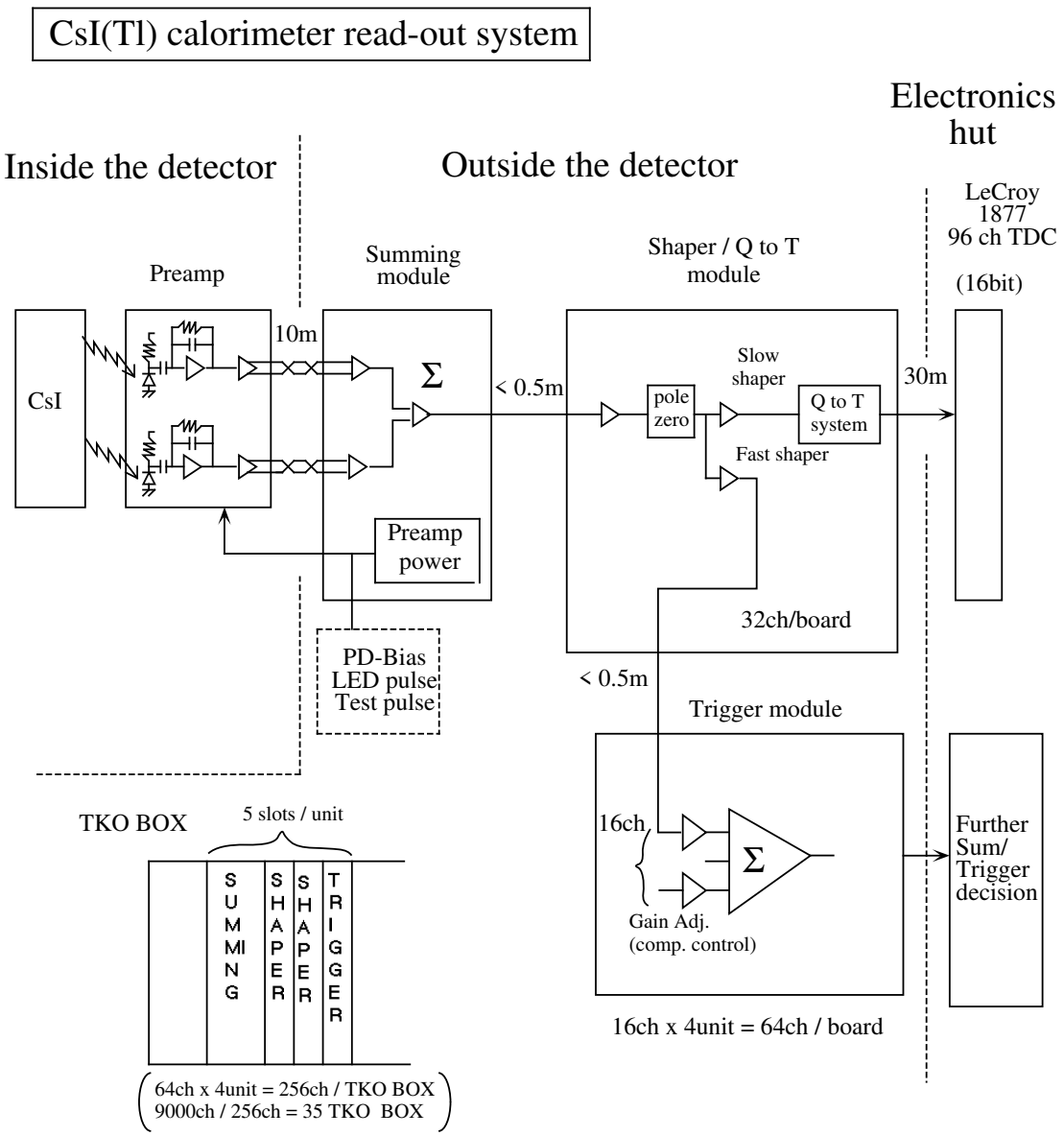

Figure 2.23: *Block diagram of the CsI(Tl) readout electronics.*

the position resolution.

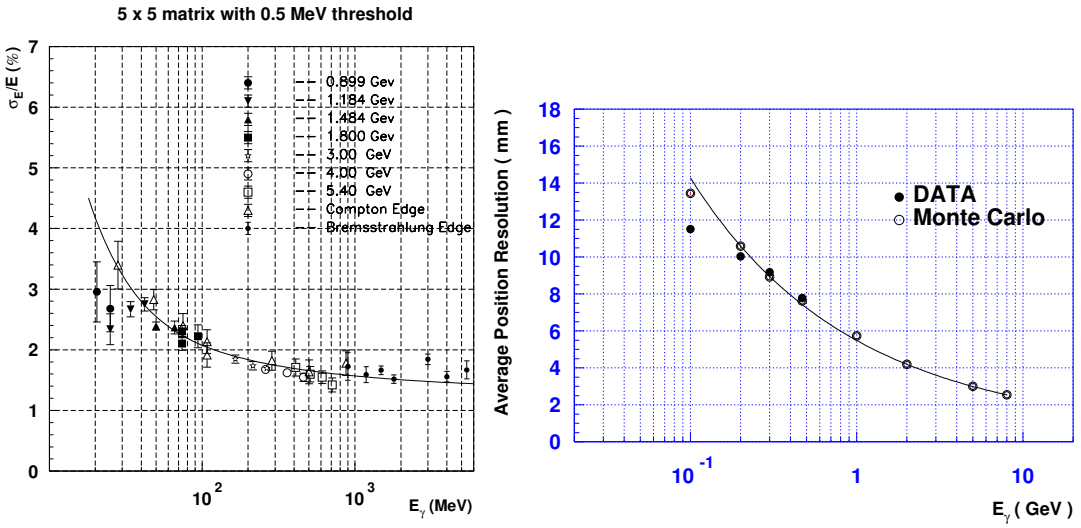

Figure 2.24: *The energy resolution (left) and the position resolution (right) of ECL as a function of incident photon energy.*

2.2.7 Solenoid Magnet

The super-conducting solenoid provides a magnetic field of 1.5 T over the tracking volume for measurement of charged particle momentum. The super-conducting coil consists of a single layer of niobium-titanium-copper alloy embedded in a high purity aluminum stabilizer. It is wound around the inner surface of an aluminum support cylinder with 3.4 m in diameter and 4.4 m length. Indirect cooling is provided by liquid helium circulating through a tube on the inner surface of the aluminum cylinder. Figure 2.25 shows the structure of the solenoid.

2.2.8 K_L and Muon Detector(KLM)

KLM detects K_L and muons. For our measurement, KLM provides muon detection for J/ψ reconstruction and flavor tagging.

KLM consists of alternating layers of charged particle detectors and 4.7 cm thick iron plates. There are 15 resistive plate counter (RPC) superlayers and 14 iron layers in the octagonal barrel region and 14 RPC superlayers in each of the forward and backward endcaps. The iron layers also serve as a return yoke of the magnetic flux provided by the super-conducting solenoid. Figure 2.26 shows the barrel part of the iron yoke. A cross section of a RPC superlayers is shown in Figure 2.27. Each RPC superlayer consists of two RPC modules and provides θ-ϕ two dimensional information. A charged particle traversing the gas gap ionizes the gas and initiates a streamer in the gas. The streamer results in a local discharge of the glass plates. This discharge is limited by the high resistivity of the plates and induces a signal on external pickup strips. The iron plates provide a total of 3.9 hadronic interaction lengths for a particle traveling normal to the

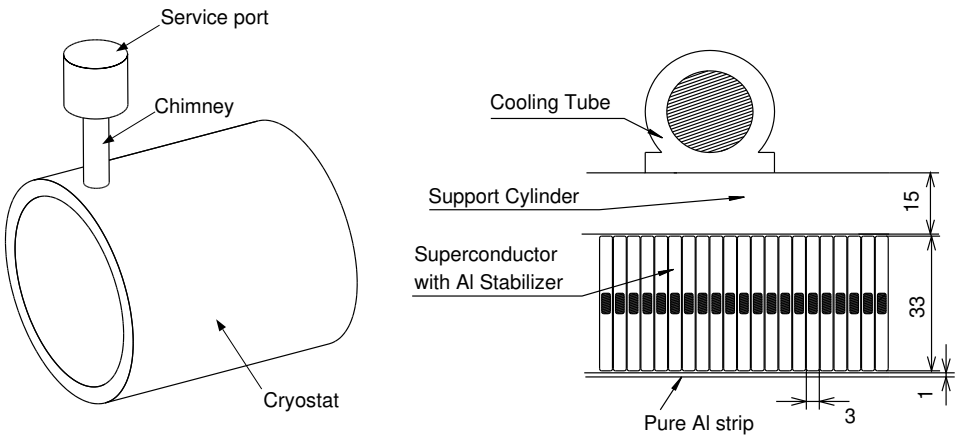

(a) Outlook of the magnet

(b) Cross sectional view of the coil

Figure 2.25: *An outlook of the solenoid and the cross-sectional view of the coil. The unit is mm.*

detector planes. K_L interacting with the iron produces a hadronis shower of ionizing particles and is detected by RPC layers.

2.2.9 Trigger and Data acquisition

The trigger system is required to catch $B\bar{B}$ event by ~ 100 % efficiency, while it is needed to suppress the trigger rate for uninteresting events. Because of the high beam current of KEKB, the trigger suffers from severe beam background. Since the beam background rates are very sensitive to actual accelerator conditions, it is difficult to make a reliable estimate. Therefore, the trigger system is required to be flexible so that background rates are kept within the tolerance of the data acquisition system and is also needed to have redundant triggers to keep the high trigger efficiency for physics events of interest.

Figure 2.29 shows a schematic view of the Belle Level 1 trigger system. It consists of the sub-detector trigger systems and the central trigger system called the global decision logic (GDL). The GDL combines the sub-detector trigger signals and make a final decision to initiate a Belle wide data acquisition within 2.2 μs from beam crossing. There are two major types of triggers prepared for the hadronic events. One is based on the charged track information from CDC. The other is provided by the energy information from ECL. These two redundant triggers provide more than 99.5 % trigger efficiency for $B\bar{B}$ events. The typical trigger rate is 300-350 Hz.

A schematic view of the Belle data acquisition system is shown in Figure 2.30. In order to keep DAQ dead time fraction less than 10 % up to a maximum trigger rate of 500Hz, the entire system is segmented into 7 subsystems running in parallel. The signals from sub-detectors are converted to timing signals by the Q-to-T converters (MQT300A) except for KLM and SVD and digitized by FASTBUS multi hit TDC (LRS1877S). KLM hits are processed by the multiplexer system and feed to LRS1877S. SVD signals digitized by the flush ADC system and processed by DSP (Digital Signal Processing) for noise reduction. The data of each subsystem are sent to the event builder. The event builder converts "detector-by-detector" parallel data streams to an "event-by-event" data river and sent

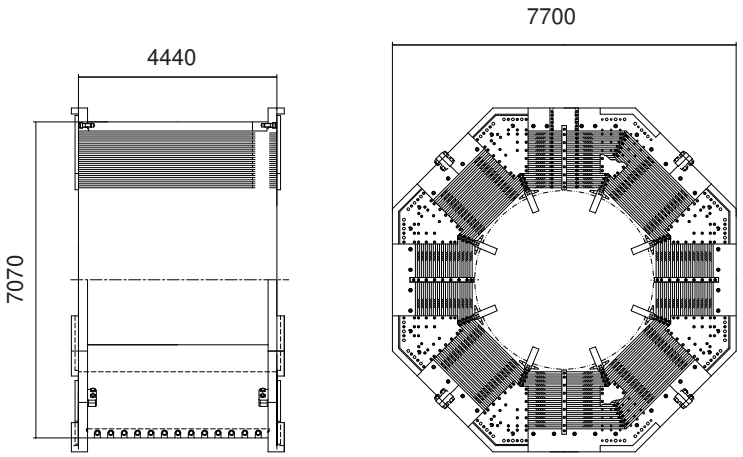

Figure 2.26: *Barrel part of the iron yoke. The unit is mm.*

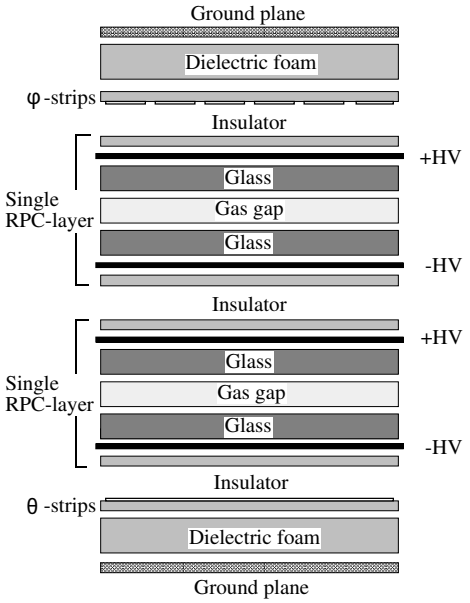

Figure 2.27: *Cross section of a KLM super-layer.*

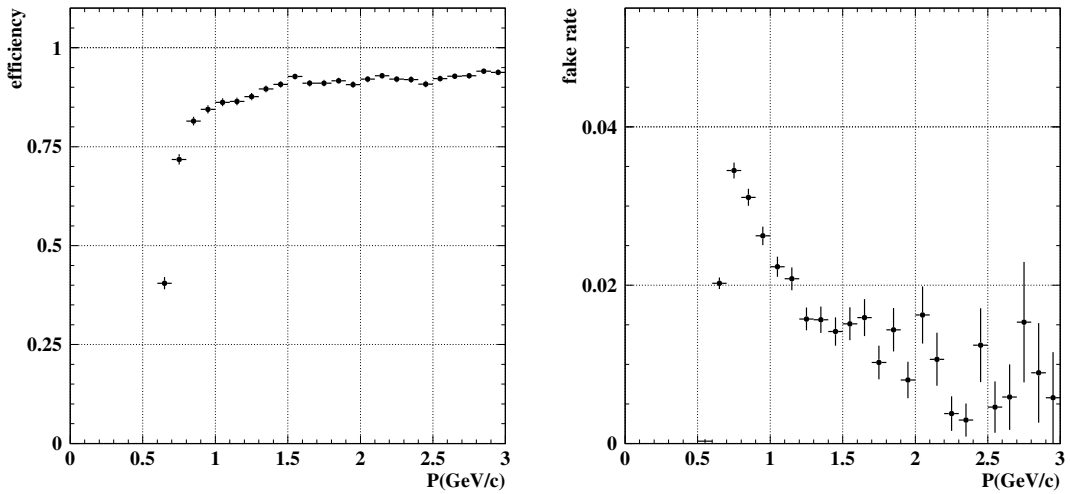

Figure 2.28: *Muon identification efficiency versus momentum in KLM (left). Fake rate for charged pions versus momentum in KLM (right).*

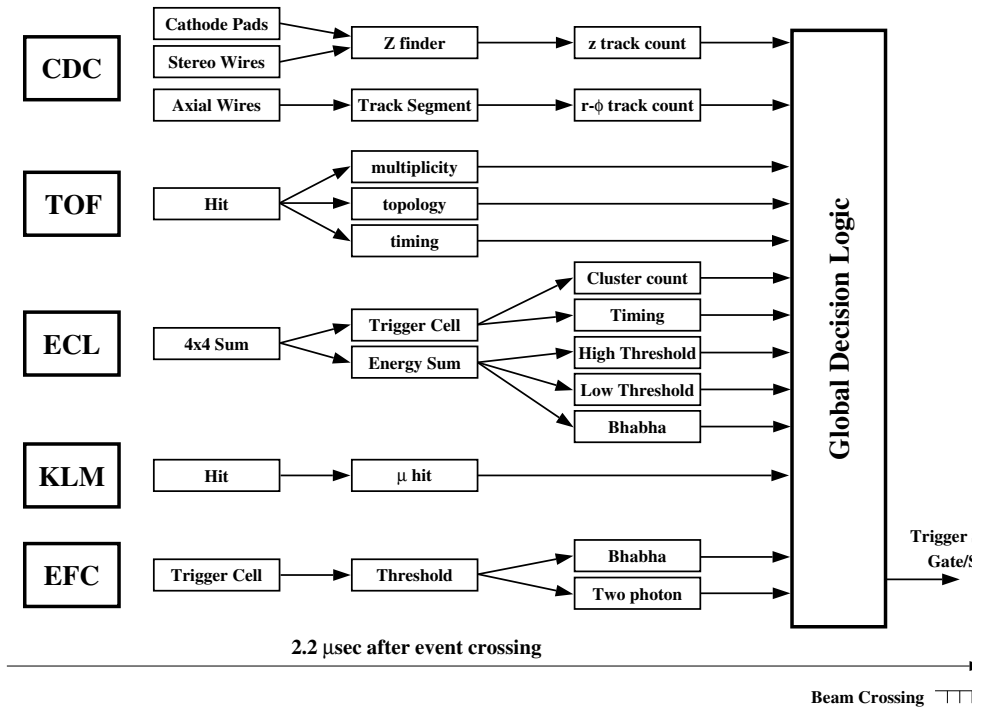

Figure 2.29: *The Level-1 trigger system for the Belle detector.*

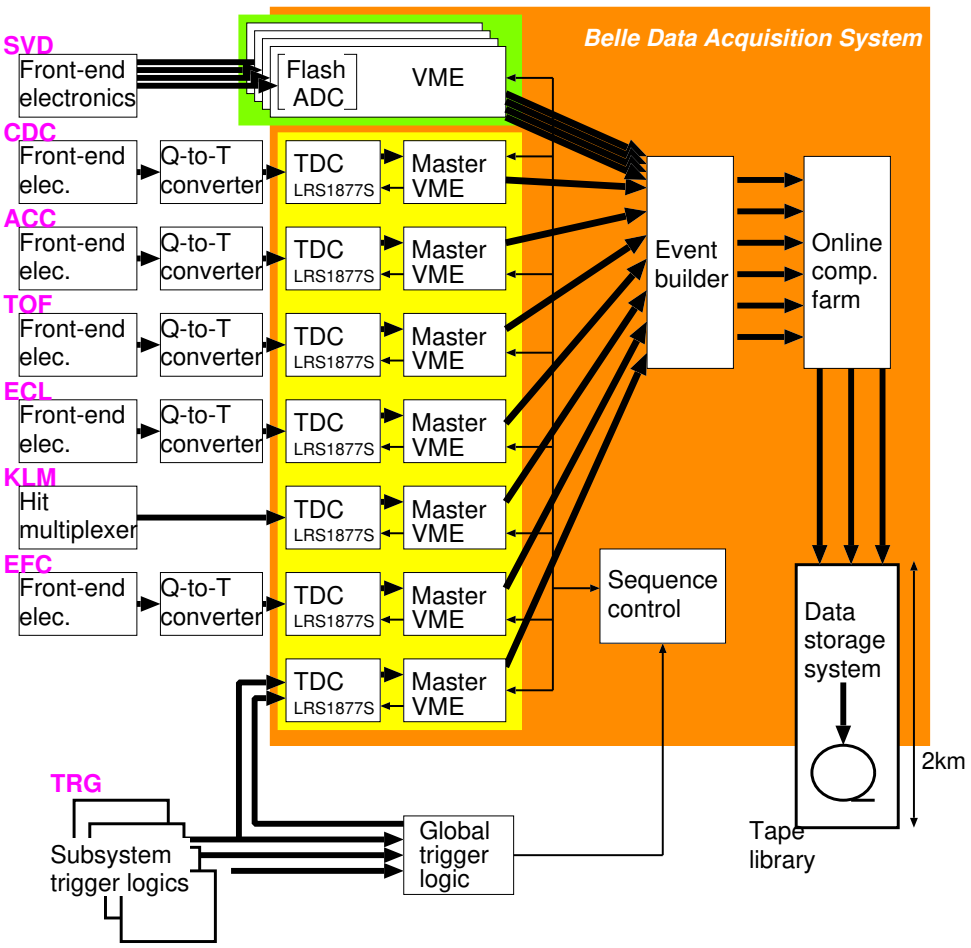

Figure 2.30: *Belle DAQ system overview.*

the data to an online computer farm. The online computer formats an event data into an offline event format and performs a background reduction (the Level 3 trigger) after a fast event reconstruction. The data are then sent to a mass storage system located at the computer center 2 km away via optical fibers. A typical event data size is about 30 kB, which corresponds to the maximum data rate of 15 MB/s.

2.2.10 Offline Software and Computing

Collected data by the Belle detector are analyzed at the offline computer farm. To cope with large data which accumulate at a rate of 400 GB a day, the parallel processing scheme by multi-CPU-servers is developed. Belle has a PC farm equivalent to 650 GHz Pentium III for data analysis. The PC farm is capable of processing $\sim 2\ fb^{-1}$ data a day.

All software for the data acquisition and the data analysis except for a few HEP specific and non HEP specific free software packages has been developed by the members of the Belle collaboration. In particular, the mechanisms to process events in parallel on large SMP (Symmetric Multiple Processor) computer servers have been developed locally using C and C++ programming languages. The users' reconstruction and analysis codes run on the event processing framework, called BASF (Belle AnalySis Framework), as modules

and are linked dynamically at the run time. The BASF takes care of input/output of event data, parallel processing and HBOOK[27] output.

The Monte Carlo simulation (MC) is also an important task of the computing. Using the MC sample, we study the detector response to the physics events and determine the analysis procedure. The physical process of production and decay is simulated by event generator softwares. We use two event generator softwares: QQ[28] and EvtGen[29, 30]. QQ event generator was originally developed by CLEO and modified for the use of the Belle analysis[31]. We use QQ to generate large number of $\Upsilon(4S)$ decays to study background for $B^0 \to J/\psi\pi^0$ decays. EvtGen is developed by CLEO and BaBar. It is designed so that the extension of the generator can be done easily by adding a new decay as a module. The B decay sample generated by EvtGen is used to study signal event selection criteria and the flavor tagging algorithm. The detector response is simulated with the Belle full detector simulator called GSIM based on GEANT[32]. GEANT is a library developed at CERN to simulate reactions between particles and matters. The simulator takes the data from the event generator and traces the behavior of each particle in the detector, generating detector response which simulates the real detector output.

2.3 Particle Reconstruction

The final state particles' energy, momentum and pieces have to be reconstructed from the recorded detector hits. In this chapter, the key reconstruction techniques for charged particles and photons are described.

2.3.1 Charged particle reconstruction

The first step of charged particle reconstruction is finding track-segment-hit-patterns in the CDC. The tracks projected onto the $r - \phi$ plane are searched for with axial wire hits, then hits of the stereo wires are used to determine z positions of the track. Track parameters (momentum and position) of the found track are obtained by the fitting based on the Kalman filter technique [33], which minimizes the effects of the multiple Coulomb scattering and non-uniformity of the magnetic field in the CDC in the determination of the track parameters. Then, all of the hit points are connected and fitted to a helix to obtain the particle momentum and position. Finally, the reconstructed charged particle trajectory is extrapolated toward the SVD to be connected to the SVD hits to improve the resolution of track parameters. Here, the track parameters are computed again with combination of the hits on the CDC and the SVD.

The track momenta are calibrated by a scaling constant so that reconstructed invariant masses of $J/\psi \to \mu^+\mu^-$ and $D^0 \to K^-\pi^+$ decays become consistent with the world averages. The calibrations are made for every run range typically a few month data taking. The major source of a change in the calibration constant comes from the fluctuation of a current supplied to the solenoid magnet and the amount of the correction is $\mathcal{O}(10^{-3})$. The estimated errors of track parameters are also calibrated by a scaling constant using the cosmic ray events in which a cosmic ray particle penetrates detector and is recognized by the track finding algorithm as two individual tracks. Since the "two" tracks must possess same track parameters, the difference between these "two" tracks is suitable to calibrate the estimated errors of the track parameters. Typical amounts of the corrections by the

scaling constants are 10 - 15 %.

2.3.2 Photon reconstruction

Photon or electron cause electromagnetic shower at the CsI(Tl) crystal in the ECL, then its energy is measured. A electromagnetic shower spreads over several crystals that are neighboring each other. Therefore, such a group of crystal hits, which is called cluster, has to be found to reconstruct a shower. First, a local maximum energy crystal, whose energy deposit exceeds 10 MeV, is picked up as a "seed crystal". The surrounding crystals of 5×5 matrix is the basis of the shower reconstruction. Figure 2.31 shows the cluster of 5×5 crystals.

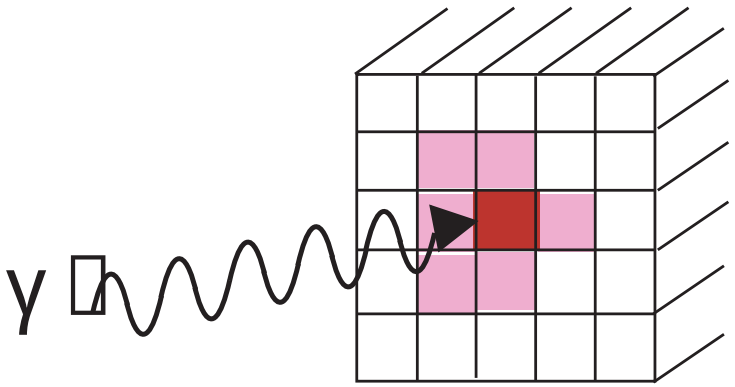

Figure 2.31: *The cluster of 5×5 crystals. Hatched crystal with most dark color is a seed crystal.*

The crystal hits less than 0.5 MeV are suppressed by the readout TDC(LRS 1877S). All the recorded hits(i.e. at least 0.5 MeV) in the 5×5 matrix are summed up to get the incident particle's energy. The incident position is calculated by the energy-weighted average position of the recorded crystal hits inside 5×5 matrix. Here, since naiive calculations of the energy and position have some systematic behavior due to electromagnetic shower development characteristics and finite crystal size(∼5.5×5.5 cm at the front face), we apply the appropriate corrections which are determined by Monte Carlo simulation.

To check matching among the reconstructed showers and tracks, a track is extrapolated up to the calorimeter crystal front face. When the extrapolated track go across a CsI crystal front face, the shower including the hit crystal, at which the extrapolated track arrived, is regarded as an associated shower with the charged track.

Among the showers that are not associated with any charged tracks, we accept all the reconstructed ones as photons if they exceed 0.5 GeV. Below 0.5 GeV, we require following criteria to be recognized as a photon; having at least 20 MeV, shower width is less than 6 cm and E9/E25 is greater than 0.75, where, shower width is the lateral spread of the shower calculated as the energy-weighted distance between crystal hits and the shower center, E9/E25 means the ratio of between the energies contained by 3×3 and 5×5 crystal matrices surrounding the seed crystal. The selected photon candidates are used to reconstruct π^0 mesons as described in Section 3.3.2.

2.4 Particle Identification

The particle identification play a role in flavor tagging and efficient reconstruction of particle. In this section, the method of particle identification is described.

2.4.1 $K^{\pm}/\pi^{\pm}$ Identification

The separation of kaons from pions is crucial for flavor tagging. The $K^{\pm}/\pi^{\pm}$ identification is carried out by combining information: dE/dx measurement by CDC, information from TOF, and measurement of the number of photoelectrons in the ACC. For each charged track, we calculate probability with kaon and pion hypothesis for each subdetector. The probabilities of each subdetector is combined to form a likelihood ratio defined as $PID(K) \equiv P_K/(P_K + P_\pi)$, where P_K and P_π are product of subdetectors' probabilities for $K^{\pm}$ and $\pi^{\pm}$, respectively. The $K^{\pm}/\pi^{\pm}$ identification is performed with the $PID(K)$. The $K^{\pm}$ identification efficiency and wrong identification probability of $\pi^{\pm}$ as $K^{\pm}$ measured with $D^{*\pm} \to D^0(\to K^{\mp}\pi^{\pm})\pi^{\pm}$ decays are shown in Figure 2.32. For most of the momentum region, the measured $K^{\pm}$ identification efficiency exceeds 80%, while the π fake rate is kept below 10%.

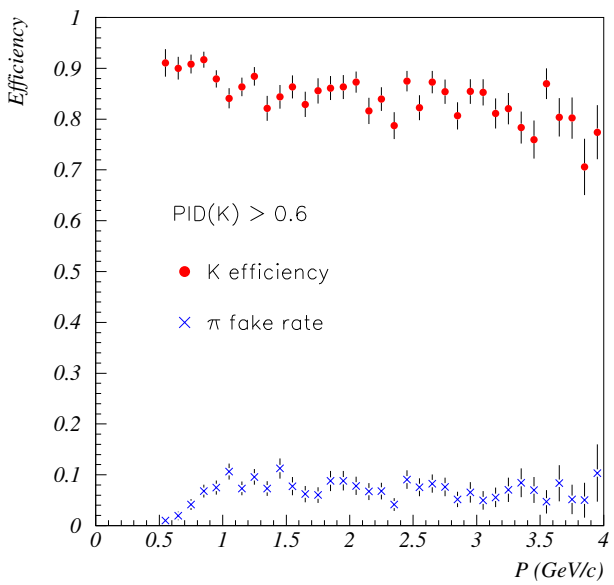

Figure 2.32: *K efficiency and π fake rate as a function of momentum.*

2.4.2 Electron Identification

For electron identification, we use the following discriminants that are based on the information from CDC and ECL.

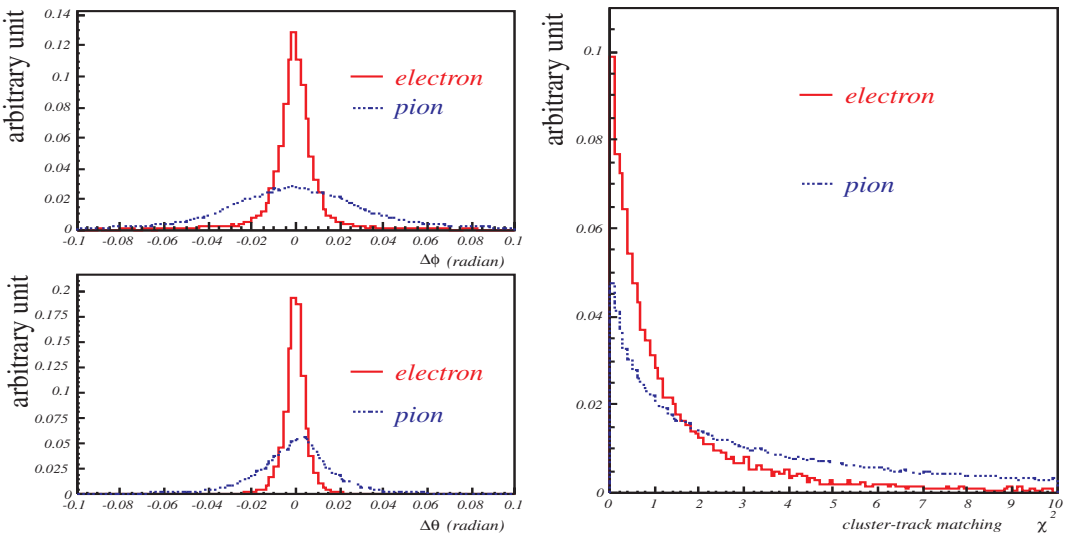

Figure 2.33: $\Delta\phi$ (left, top), $\Delta\theta$ (left, bottom), and cluster-track matching χ^2 (right) distributions for electrons and charged pions.

- Matching of an extrapolated track position and a cluster position in the ECL
  It is important for electron identification to find out a right combination of a cluster and track position. The ECL cluster position is determined by the center-of -gravity of the ECL hits in the cluster. Figure 2.33 shows the difference in ϕ ($\Delta\phi$) and θ ($\Delta\theta$) between a cluster position and a position of an extrapolated electron track. Since the lateral spread of electron is narrower than that of hadronic showers, the electron's cluster position matches with the extrapolated track position better than that of hadron's.

  Using the $\Delta\phi$ and $\Delta\theta$, we form the matching χ^2 to identify electrons as follows:

$$\chi^2 \equiv \left(\frac{\Delta\phi}{\sigma_{\Delta\phi}}\right)^2 + \left(\frac{\Delta\theta}{\sigma_{\Delta\theta}}\right)^2$$

  where $\sigma_{\Delta\phi}$ and $\sigma_{\Delta\theta}$ are the widths obtained by fitting the $\Delta\phi$ and $\Delta\theta$ distribution of electrons with Gaussian. The χ^2 distributions for electrons and charged pions are shown in Figure 2.33 For each charged track, a cluster that gives the minimum χ^2 and that have the χ^2 less than 50, is take for the matched cluster.

- Ratio of cluster energy measured by ECL (E) and charged track momentum (p) measured by CDC : E/p
  The E/p is use as a powerful discriminant to distinguish electrons from hadrons. Since electron deposit almost all energy in ECL, the electron's E/p expected to be unity. While, the deposit energy of hadrons in ECL is smaller than their momentum ($E < p$). Figure 2.34 shows E/p distribution for electrons and pions. The momentum range is 0.5 GeV/c < p_{lab} < 3.0 GeV/c in the laboratory frame. The tail in the lower E/p side of electrons comes from interaction of electrons with materials in front of ECL. As shown in Figure 2.34 which shows the momentum dependence of E/p, E/p is more efficient in high momentum region.

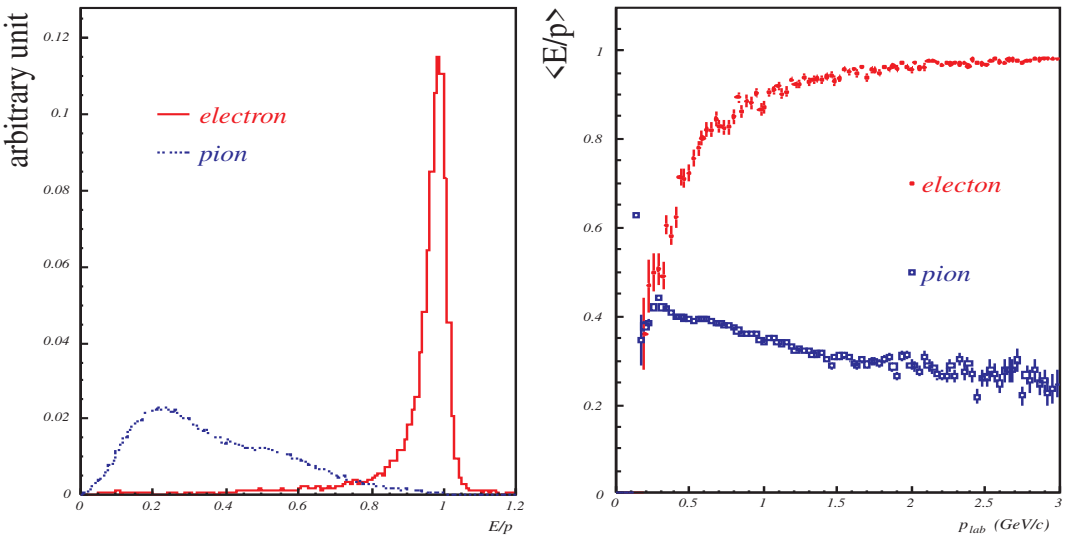

Figure 2.34: E/p distribution (left) and momentun dependence distribution of E/p (right) for electrons and charged pions.

- Shower shape
  Since electromagnetic shower and hadronic shower have different shape in both transverse and longitudinal direction, this difference can be used as a significant discriminant. The shower shape in the transverse direction can be evaluated with $E9/E25$, which is defined as a ratio of energy summed in 3 $\times$ 3 crystals to that in 5 $\times$ 5 crystals. Figure 2.35 shows $E9/E25$ for electrons and charged pions. Electrons have a peak at around 0.95 with relatively small low-side tail, while pions have more events in the lower $E9/E25$ region.

- dE/dx measurement by CDC
  Energy deposit in CDC is measured as dE/dx. As shown in Figure 2.36 which shows dE/dx of electrons and pions, the $dEdx$ enables us to distinguish electrons and hadrons effectively. The averaged dE/dx as a function of momentum is shown in Figure 2.36. From the distribution, the separating power is higher in the lower momentum region and this feature is supplementary to the ability of E/p.

In additional to above discriminants, light yield in ACC is also incorporated for the electron identification to eliminate kaons. The likelihood ratio $\mathcal{L}_e$ computed with combination of above quantities is defined as

$$\mathcal{L}_e = \frac{\prod_i P_e(i)}{\prod_i P_e(i) + \prod_i P_h(i)}$$

where $P_e(i)$ and $P_h(i)$ are the probabilities to identify electrons and hadrons respectively, which are calculated from i-th discriminator. Figure 2.37 shows the electron identification efficiency measured with $e^+e^- \to e^+e^-e^+e^-$ data and the fake rate for charged pions from $K_S \to \pi^+\pi^-$ decays as a function of momentum. The efficiency of electron identification is greater than 90 % and the hadron fake rate is less than 1% for $p_{lab} > 1$ GeV/c. The detailed description of electron identification are given in [34].

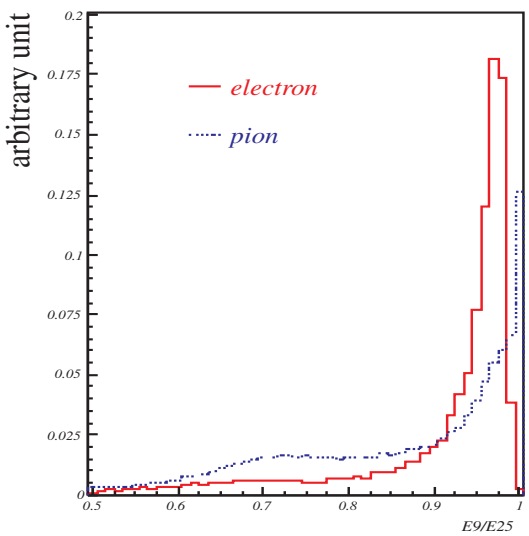

Figure 2.35: $E9/E25$ distribution for electrons and pions

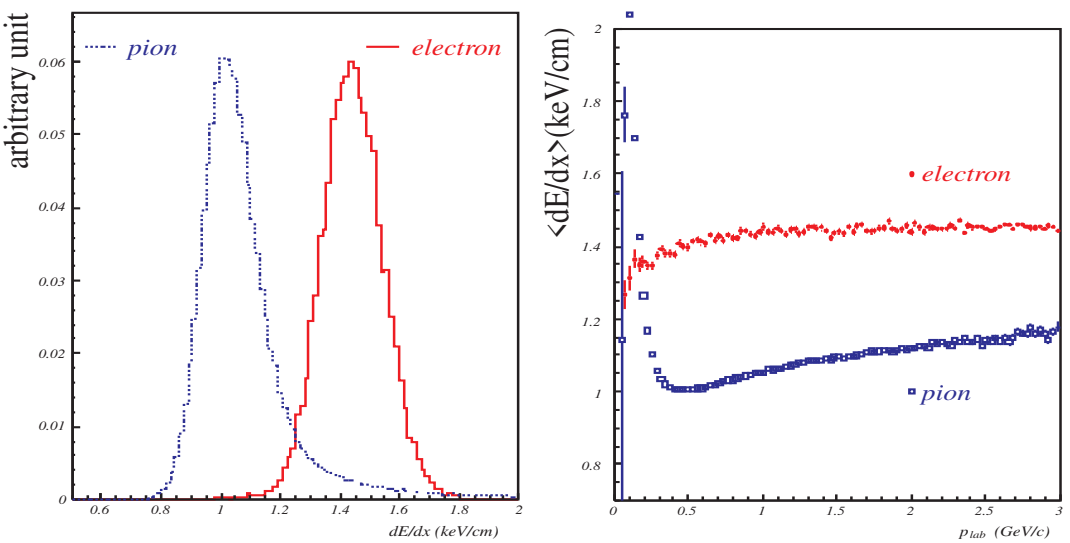

Figure 2.36: dE/dx distribution (left) and momentum dependence distribution of dE/dx (right) for electrons and charged pions.

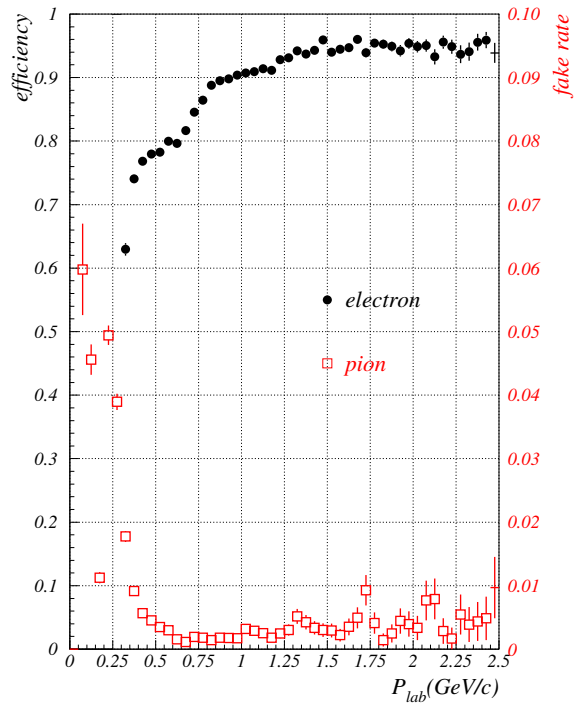

Figure 2.37: *Electron identification efficiency (circles) and fake rate for charged pions (squares). Note the different scales for the efficiency and fake rate.*

2.4.3 Muon Identification

KLM provides muon identification for charged particles with momenta greater than 0.6 GeV/c. Charged particles with momenta less than 0.6 GeV/c cannot reach KLM. The muon identification is performed based on the range and the transverse scattering in KLM. Muons pass through KLM with small deflections, while hadrons, which are dominated by pions, are deflected by the strong interaction with iron and then stop within less iron layers than muons. These information is parametrized by the number of penetrated iron plates and the reduced χ^2 calculated with the extrapolated charged track and the position of KLM hits. A likelihood ratio of the muon hypothesis and the pion hypothesis is made combining these two information and is used to separate muons from hadrons. Figure 2.38 shows the muon identification efficiency measured with cosmic muons as a function of momentum and the fake rate for $\pi^{\pm}$ measured with $K_S \to \pi^+\pi^-$ decays. Typical efficiency for momentum grater than 1 GeV/c is better than 90%, while fake rate for $\pi^{\pm}$ is smaller than 2 %. The details of muon identification are given in [35].

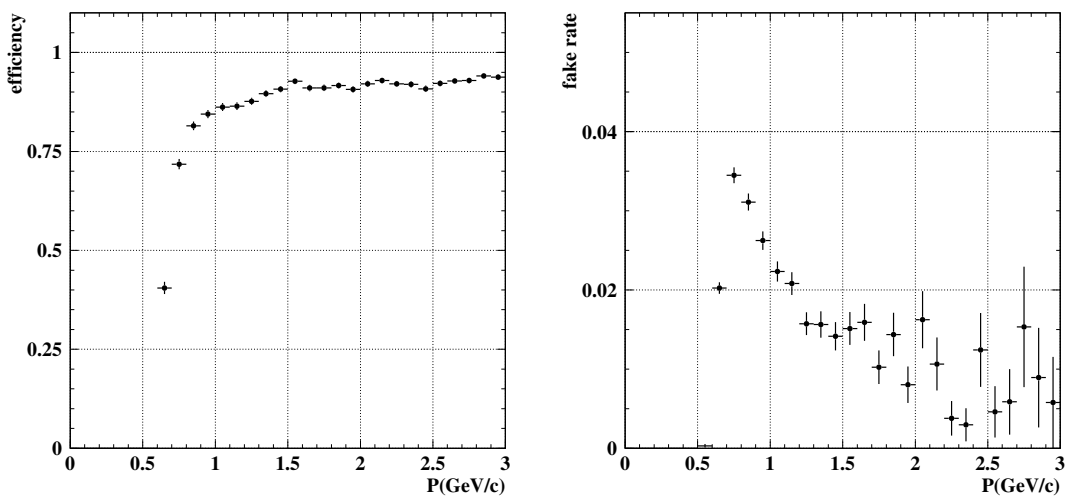

Figure 2.38: *Muon identification efficiency versus momentum in KLM (left). Fake rate for charged pions versus momentum in KLM (right).*

Chapter 3

Event Selection and Reconstruction

In this chapter, we describe the procedure of the event selection and reconstruction for $B^0 \to J/\psi\pi^0$ candidates. First, we select hadronic events from the data sample collected by the Belle detector. Then we reconstruct $J/\psi$and π^0, and fully reconstruct B meson candidates from them. For the reconstructed events, we apply flavor tagging procedure to determine the flavor of associated B meson. We also reconstruct the decay vertices of B^0 and $\overline{B}^0$ to measure proper-time difference.

3.1 Data Sample

The data sample used for this analysis is collected by the Belle detector from January 2000 to July 2003. The integrated luminosity at the $\Upsilon(4S)$ resonance is 140 fb^{-1}, corresponding to 15.2×10^7 $B^0\overline{B}^0$ pairs. The branching fractions of the decays related to this analysis are listed in Table 3.1. We expect 112 events as $B^0 \to J/\psi\ \pi^0$ candidates in the data sample.

Mode	Branching ratio
$\Upsilon(4S) \to B^0\overline{B}^0$	50 %*
$B^0 \to J/\psi\pi^0$	$(2.2 \pm 0.4) \times 10^{-5}$
$J/\psi \to l^+l^-$	(11.81 ± 0.14) %
$\pi^0 \to \gamma\gamma$	(98.8 ± 0.03) %

Table 3.1: *Branching fractions for each decay modes related to this analysis[46].*

3.2 Hadronic Event Selection

The data sample contains not only $\Upsilon(4S)$ production but also several processes such as continuum $e^+e^- \to q\bar{q}$ ($q = u, d, s, c$) processes, mu pair production, tau pair production, Bhabha (including radiative Bhabha)and two-photon events. The cross section of these processes are listed in Table 3.2. The data sample also contains as well as cosmic ray events, and beam background, which occur from spent electrons that go out the beam orbit due to the bremsstrahlung, and the interactions between the electron (or positron) and beam gas. To suppress these uninteresting events and select hadronic events that

Process	Cross section (nb)
$e^+e^- \to \Upsilon(4S)$	1.2
$e^+e^- \to q\bar{q}$ $(q = u, d, s, c)$	2.8
$e^+e^- \to l^+l^-$ $(l = \mu, \tau)$	1.6
Bhabha ($\theta_{lab} > 17^\circ$)	44.
two-photon ($\theta_{lab} > 17^\circ$, $p_t > 0.1$ GeV)	~ 15

Table 3.2: *Cross sections for each processes in e^+e^- collisions at the center of mass energy of $\sqrt{s} = 10.58$ GeV [37]. θ_{lab} and p_t are the polar angle in the laboratory frame and p_t is transverse momentum of the final state particle, respectively.*

consists of continuum and $\Upsilon(4S)$ production, we apply the following requirements:

- The number of good charged tracks ≥ 3.
  Where the good charged track is defined to satisfy (1) transverse momentum, $P_t > 0.1$ GeV/c, (2) the impact parameter to the nominal interaction point in the x-y plane, $|dr| < 2.0$ cm, (3) the impact parameter to the nominal interaction point along z-axis, $|dz| < 4.0$ cm.

  This requirement is effective to suppress Bhabha and μ pair production. It also reduces the cosmic ray and the beam background because the tracks from these events come from arbitrary points while the tracks from hadronic events come from the nominal interaction point.

- At least one "good" ECL cluster should be within the fiducial volume of $-0.7 < cos\theta < 0.9$. The good ECL cluster is defined as the cluster having the energy more than 100 MeV. This requirement reduces Bhabha events because most clusters for Bhabha events have a very shallow angle.

- The total visible energy $E_{vis} > 0.2\sqrt{s}$ where $\sqrt{s}$ represents the cms energy. The E_{vis} is calculated from the good tracks assuming the pion mass and good photons in an events, where the good photon is defined as the good ECL cluster within the CDC acceptance ($17^\circ < \theta < 150^\circ$ in the laboratory frame) with no associated tracks from the CDC.

- The energy sum of the good ECL clusters within the CDC acceptance, E_{sum} is required to satisfy

$$0.1 < E_{sum}/\sqrt{s} < 0.8.$$

- The average cluster energy defined as E_{sum}/(Number of good ECL cluster), including the ones outside the CDC acceptance, is required to be

$$E_{sum}/(\text{Number of good ECL cluster}) < 1.\ \text{GeV}.$$

  This requirement is to suppress the Bhabha process.

- The momenta sum of good tracks and good photons is required to be balanced in the z direction to eliminate the beam background.

$$|P_z| < 0.5\sqrt{s}.$$

- The position of the primary vertex is required to satisfy $|r_{vertex}| < 1.5$ cm and $|z_{vertex}| < 3.5$ cm, where primary vertex is obtained from all good charged tracks, r and z represent the position of the primary vertex in the r-ϕ plane and the z-axis, respectively.

- We separate the event into two hemispheres by a plane perpendicular to the event thrust axis. The invariant mass of tracks in each hemisphere is calculated assuming a pion mass. This invariant mass is basically equivalent to the invariant mass of τ in τ pair production process. In the event, we regard the lager invariant mass as heavy jet mass, M_{jet}. it is required to satisfy

$$\begin{aligned} M_{jet} > 1.8GeV/c^2 \quad &\text{or} \quad E_{sum}\sqrt{s} > 0.18 \\ M_{jet} > 1.8GeV/c^2 \quad &\text{or} \quad M_{jet}/E_{vis} > 0.25 \end{aligned}$$

  where E_{sum} includes the cluster outside the CDC acceptance. This requirement is to suppress tau pair, beam gas, and two-photon events and to regain continuum events which are inconsistent with tau pair events.

The efficiencies of the hadronic event selection is 99.1% for $B^0\overline{B}^0$ events and 79.5% for continuum process. While, reducing the contamination of the non-hadronic components to be less than 5% [38].

In addition, to suppress continuum process, we require the event shape variable R_2 to be less than 0.5, where R_2 is the ratio of the second to the zeroth Fox-Wolfram moment [39]. R_2 is defined as

$$R_2 \equiv \frac{\sum_i^N \sum_j^N [|\vec{p_i}||\vec{p_j}| \cdot (3\cos^2\phi_{ij} - 1)]}{2\sum_i^N \sum_j^N [|\vec{p_i}||\vec{p_j}|]} \tag{3.1}$$

where $\vec{p_i}$ is a momentum vector of i-th particle, ϕ_{ij} is an angle between $\vec{p_i}$ and $\vec{p_j}$ in the cms, and N is a total number of particles in the event. For jet-like event, such as continuum, most $\cos\phi_{ij}$ are likely to be $\sim \pm 1$ and the denominator in equation 3.1 becomes similar number. R_2 becomes 1 in the limits of narrowest two-jet event. While, in the case of spherical events like B decays, $R_2 \simeq 0$. The efficiency loss due to R_2 selection is estimated to be smaller than 0.5 % [38].

3.3 $B^0 \to J/\psi\pi^0$ Reconstruction

3.3.1 Reconstruction of J/ψ

J/ψ mesons are reconstructed via their decay into oppositely charged lepton pairs (e^+e^- or $\mu^+\mu^-$). Leptons are selected from charged tracks satisfying $|dz| < 5$ cm. For electron identification, the ratio between the charged track's momentum and the associated shower energy (E/p) is the most powerful discriminant. Other information including dE/dx, the distance between the ECL shower and the extrapolated track, and the shower shape are

also used. Muons are identified by requiring an association between KLM hits and an extrapolated track. Both lepton tracks must be positively identified as such.

In the e^+e^- mode, ECL clusters that are within 50 mrad of the track's initial momentum vector are included in the calculation of the invariant mass ($M_{e^+e^-(\gamma)}$), in order to include photons radiated from electrons/positrons. The invariant mass $M_{l^+l^-}$ ($l = e \text{or} \mu$) is calculated

$$M^2_{l^+l^-} = (\sqrt{M^2_{l^+} + |\vec{p_{l^+}}|^2} + \sqrt{M^2_{l^-} + |\vec{p_{l^-}}|^2})^2 - |\vec{p_{l^+}} + \vec{p_{l^-}}|^2, \tag{3.2}$$

where e^+e^- case, $\vec{p_{l^+}}$ and $\vec{p_{l^-}}$ are the corrected with the four-momentum of the included photons. Figure 3.1 shows the invariant mass distributions of $M_{e^+e^-}$. Although the radiative photon's effect is included, a broad tail in the lower mass region is seen in the distribution. It is due to absorption of photon by the material in front of the ECL. Thus, the invariant masses of e^+e^-, $M_{e^+e^-}$ is required to fall in the ranges -150 MeV/c^2 $< (M_{e^+e^-} - M_{J/\psi}) < 36$ MeV/c^2. Here $M_{J/\psi}$ denotes the world average of the J/ψ mass [46]. For the invariant mass of $\mu^+\mu^-$, $M_{\mu^+\mu^-}$, it is required to satisfy -60 MeV/c^2 $< (M_{\mu^+\mu^-} - M_{J/\psi}) < 36$ MeV/c^2. The invariant mass window is asymmetric due to missing energy carried out by radiative photon, though the effect is much smaller than e^+e^- case. Figure 3.2 shows the invariant mass distributions of $M_{\mu^+\mu^-}$, where arrows indicate the edges of the mass window.

For the J/ψ candidate events after the invariant mass selection, we apply the fit with vertex and mass constraint, which is we vary the momentum of lepton tracks within these error under the constraint that these tracks come from same decay vertex point, and the invariant mass of lepton pair becomes to be the world average J/ψ mass. It improves the reconstructed B^0 momentum resolution.

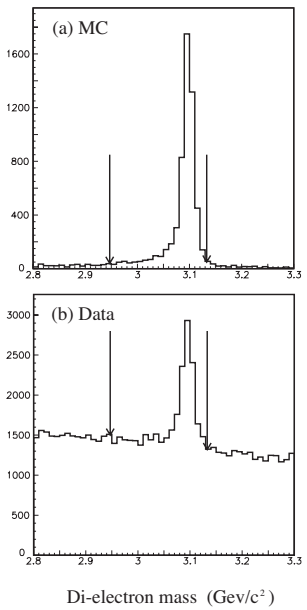

Figure 3.1: *The invariant mass distribution of $M_{e^+e^-}$ for (a) data and (b) signal Monte Carlo. Arrows indicate the invariant mass ranges.*

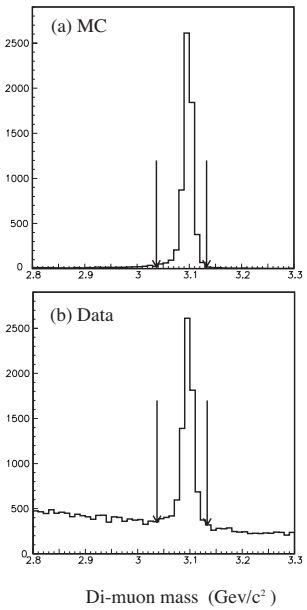

Figure 3.2: *The invariant mass distribution of $M_{\mu^+\mu^-}$ for (a) data and (b) signal Monte Carlo. Arrows indicate the invariant mass ranges.*

3.3.2 Reconstruction of π^0

π^0 is reconstructed from two photons. Photon candidates are selected as described in Section 2.3.2. To select $\pi^0 \to \gamma\gamma$ decay candidates for the $B^0 \to J/\psi\ \pi^0$ mode, the energy of each photon is required to exceed 50 MeV in the ECL barrel ($32^\circ < \theta < 129^\circ$) or 100 MeV in the forward ($17^\circ < \theta < 32^\circ$) or backward ($129^\circ < \theta < 150^\circ$) endcaps, where θ denotes the polar angle with respect to the z-axis. Neutral pion candidates are formed from photon pairs that have an invariant mass in the range 0.118 GeV/c^2 to 0.150 GeV/c^2. Figure 3.3 shows the invariant mass distribution of π^0 candidates. We apply the fit with mass constraint to those candidate photon pairs.

3.3.3 Reconstruction of B^0

J/ψ and π^0 candidates are combined to form B candidates. The B candidate selection is carried out using two observables in the $\Upsilon(4S)$ cms, the beam-energy constrained mass and the energy difference, are defined as follows:

$$M_{\rm bc} = \sqrt{(E^*_{beam})^2 - |\vec{p^*_i}|^2} \quad (3.3)$$

$$\Delta E = (E^*_i) - (E^*_{beam}) \quad (3.4)$$

where $E_{\rm beam} = \sqrt{s}/2$ is the cms beam energy, and $\vec{p_i}^*$ and E^*_i are the cms three-momenta and energies of the B meson decay products, respectively. The B meson signal region is defined as 5.27 GeV/c^2 $< M_{\rm bc} <$ 5.29 GeV/c^2 and -0.10 GeV $< \Delta E <$ 0.05 GeV. The lower bound of ΔE is chosen to accommodate the negative ΔE tail due to shower leakage associated with π^0, which appear even mass constrained fitting is performed to both J/ψ and π^0. Therefore the lower limit of ΔE requirement is relaxed than that for $B^0 \to J/\psi\ K_S(K_S \to \pi^+\pi^-)$ mode whose the decay products are all charged ones. Note that if

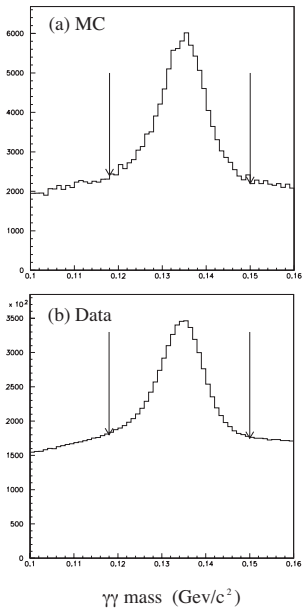

Figure 3.3: *The invariant mass distribution of photon pairs for (a) data and (b) signal Monte Carlo. Arrows indicate the invariant mass ranges.*

ΔE lower limit is relaxed, we pick up more background due to $B^0 \to J/\psi\, K_S(K_S \to \pi^0\pi^0)$, which are reconstructed as $B^0 \to J/\psi\pi^0$ by missing one π^0. Figure 3.4 shows scatter plot of $M_{\rm bc}$ and ΔE for data sample. The number of reconstructed $B^0 \to J/\psi\pi^0$ candidates is 103.

3.4 Inclusive J/ψ Background

Since the main background source is B meson candidates having J/ψ and accidentally included high momentum π^0 from other decay ($B \to J/\psi X$ background), we checked the background contents using the inclusive J/ψ Monte Carlo sample [40], which is simulated B decays into J/ψ and anything. The sample corresponds to 11.6 ab^{-1} for neutral B decays and 8.4 ab^{-1} for charged decays. According to this study, the $B \to J/\psi X$ background forms a small peak in the $M_{\rm bc}$ projection for neutral B decays Monte Carlo as shown in Figure 3.5. Table 3.3 shows breakdown of decays in the signal box. $B^0 \to J/\psi K_S$ and $B^0 \to J/\psi K_L$ are dominant and their contributions are almost equal each other, so that we treat as the background from J/ψ inclusive decay has no CP asymmetry. Uncertainty due to this assumption is taken into account systematic error. We also consider the different shape between this J/ψ inclusive background and combinatorial background to which random combinations of particles in $B\bar{B}$ decays and continuum events contribute. The number of the background events in the signal region is estimated by a two-dimensional fit on the $M_{\rm bc}$-ΔE distribution. The detailed estimation of the signal fraction is described in Section 4.3.

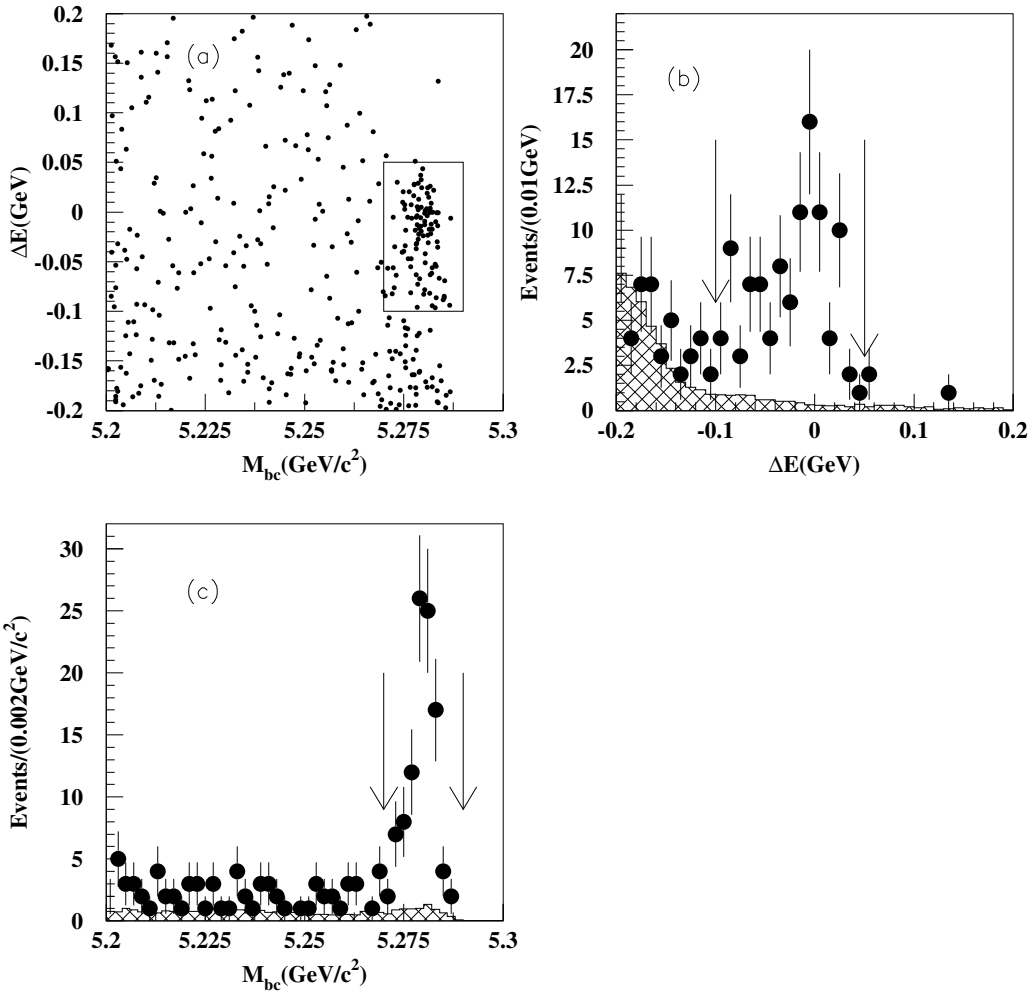

Figure 3.4: *The distribution of (a) ΔE versus $M_{\rm bc}$ for $B^0 \to J/\psi\ \pi^0$ candidates in data. The projection in (b) ΔE is shown with the requirement $5.270 < M_{\rm bc} < 5.290$ GeV/c^2 and the projection in (c) $M_{\rm bc}$ with the requirement $-0.1 < \Delta E < 0.05$ GeV. The arrows in (b) and (c) show the boundaries of the signal box. The hatched histograms show the expected background predicted by J/ψ inclusive Monte Carlo.*

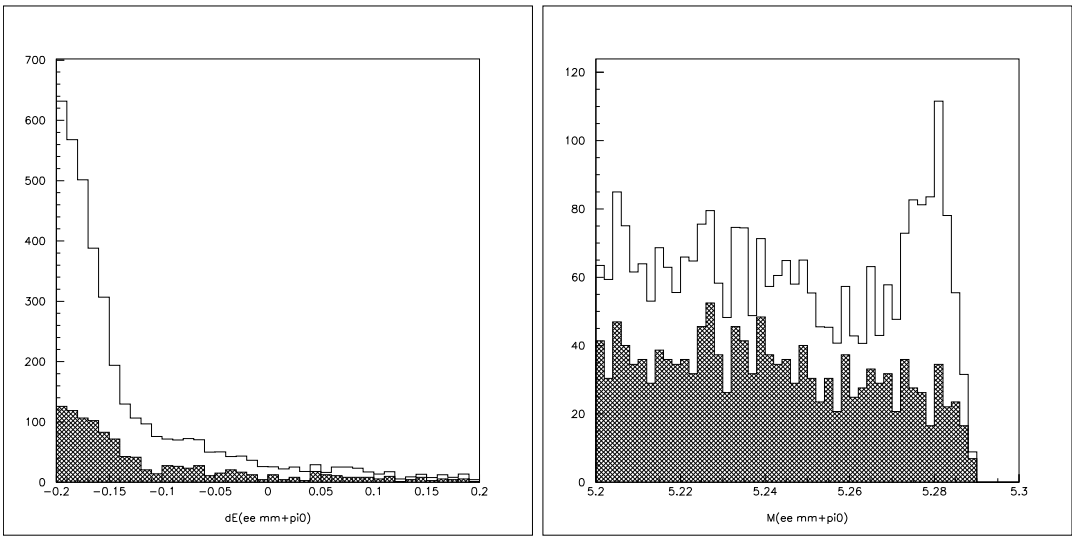

Figure 3.5: *$B \to J/\psi X$ background study: Distributions of ΔE(left) and $M_{\rm bc}$(right). Open histogram shows neutral B decay Monte Carlo, hatched histogram shows charged B Monte Carlo sample, which is normalized with the luminosity.*

Neutral B MC	
$B^0 \to J/\psi K_S$	180
$B^0 \to J/\psi K_L$	143
$B^0 \to J/\psi K^*(892)^0$	49
$B^0 \to J/\psi K_1(1270)^0$	27
$B^0 \to J/\psi K^0\pi^0\pi^0$	5
$B^0 \to J/\psi K^0\pi^+\pi^-$	5
$B^0 \to J/\psi \rho^0$	2
$B^0 \to J/\psi K^*(1430)^0$	2
χ_c feeddown	9
$\psi(2S)$ feeddown	1
total	423 (events)

Charged B MC	
$B^\pm \to J/\psi K^*(892)^\pm$	54
$B^\pm \to J/\psi K^\pm$	49
$B^\pm \to J/\psi K_1(1270)^\pm$	39
$B^\pm \to J/\psi K^*(1430)^\pm$	5
$B^\pm \to J/\psi \rho^\pm$	4
$B^\pm \to J/\psi K^\pm\pi^0\pi^0$	2
$B^\pm \to J/\psi K^\pm\pi^+\pi^-$	2
$B^\pm \to J/\psi K^0\pi^\pm\pi^0$	3
χ_c feeddown	8
total	166 (events)

Table 3.3: *Breakdown of decays in the signal box from 15.4 M events (equivalent to 11.6 ab^{-1}) for neutral B inclusive J/ψ Monte Carlo, and from 11.1 M events (equivalent to 8.4 ab^{-1}) charged B inclusive J/ψ Monte Carlo sample.*

3.5 Flavor Tagging

To measure CP asymmetry, the flavor of the B meson ($B_{\rm tag}$) has to be determined from the information of remaining tracks that are not used for $B^0 \to J/\psi\pi^0$ reconstruction. In this section, the procedure of flavor tagging is described.

3.5.1 Introduction of Flavor Tagging

To obtain the answer whether the flavor of $B_{\rm tag}$ decay is B^0 or $\overline{B}^0$, the flavor information in $B_{\rm tag}$ is extracted from the charges of tracks. The processes that are used to determine the the flavor of the $B_{\rm tag}$ are listed in Table 3.4.

Based on the measured properties of these tracks, two parameters, q and r, are assigned to each event. The first, q is corresponding to the flavor of $B_{\rm tag}$. When the $B_{\rm tag}$ is more likely to be a B^0, the q value is $+1$. Otherwise, if the $B_{\rm tag}$ is likely to be a $\overline{B}^0$, the q value is -1. The parameter r is flavor-tagging quality factor that ranges from $r = 0$ for no flavor discrimination to $r = 1$ for an unambiguous flavor assignment. It is used only to sort data into six intervals of r, according to the estimated flavor purity. In the next section, we describe how to determine the r event-by-event based on the study using a large statistics of Monte Carlo sample.

Process	Track information
Semi-leptonic decay : $\begin{cases} b \to c l^- \bar{\nu}_l \\ \bar{b} \to \bar{c} l^+ \nu_l \end{cases}$	The charge of the primary lepton with high momentum.
Cascade charm decay: $\begin{cases} b \to cX \to s(\to K^-/\bar{\Lambda})X \\ \bar{b} \to \bar{c}X \to \bar{s}(\to K^+/\Lambda)X \end{cases}$	The charge of kaons. TheflavorofΛs.
Cascade semi-leptonic decay : $\begin{cases} b \to cX \to s l^+ \nu_l X \\ \bar{b} \to \bar{c}X \to \bar{a} l^- \nu_l X \end{cases}$	The charge of the secondary lepton with low momentum.
π production: $\begin{cases} B^0/B^- \to D^{(*)+}/D^{(*)0} + \pi^- X \\ \bar{B}^0/B^+ \to D^{(*)-}/\bar{D}^{(*)0} + \pi^+ X \end{cases}$	The charge of the pion with high momentum.
D^* production: $\begin{cases} B^0/B^- \to D^{*+}X, D^{*+} \to D^0\pi^+ \\ \bar{B}^0/B^+ \to D^{*-}X, D^{*-} \to \bar{D}^0\pi^- \end{cases}$	The charge of the pion with low momentum.

Table 3.4: *The list of detector resolution function parameters.*

3.5.2 Flavor tagging Method

The flavor tagging is proceeded in two stages, track-level flavor tagging and event-level flavor tagging. The track-level flavor tagging has four categories in parallel with different purpose, leptons, slow pions, Λ baryons, kaons. Figure 3.6 shows the schematic view of the flavor tagging algorithm.

Each track from $B_{\rm tag}$ is classified into one of for categories, leptons, kaons, slow pions, Λ baryons. The tracks for each event is required to satisfy $dr < 2.0$ cm and $|dz| < 10.0$ cm, where dr and dz are the impact parameters in the r - ϕ plane and z direction, respectively. The tracks from K_S candidates are not used.

- Lepton category
  In the lepton category, the high momentum leptons from the semi-leptonic B decays and the medium momentum leptons from the cascaded semi-leptonic D decays are accepted. This category consists of tow sub-categories: electron-like category and muon-like category, The track that is classified into electron like category is required to have the cms momentum (p_l^*) lager than 0.4 GeV/c and the likelihood ratio to distinguish electrons from kaons lager than 0.8. The track of which p_l^* is lager than 0.8 GeV/c are assigned to the muon category if the likelihood ratio to distinguish muons from kaons is lager than 0.95. We construct the look-up table of the multi-dimensional likelihood with six variables, the p_l^*, the lepton likelihood, the polar angle of track ($cos\theta_{lab}$), lepton charge, the recoil mass ($M_{\rm recoil}$) and the missing cms momenta ($p_{\rm miss}$), where the recoil mass is defined as the invariant mass formed by all $B_{\rm tag}$ tracks except for the lepton. The numbers of bins for each discriminant are 11, 4, 6, 2, 10 and 6, respectively. In total, the number of bins of the look-up table is 31680. For each of 31680 bins, we assign the $r \cdot q$ value calculated as:

$$r \cdot q \equiv \frac{N_{B^0} - N_{\overline{B}^0}}{N_{B^0} + N_{\overline{B}^0}} \tag{3.5}$$

  where N_{B^0} and $N_{\overline{B}^0}$ are numbers of B^0 and $\overline{B}^0$ in the bin estimated from the Monte Carlo simulation. The look-up tables of other categories are constructed in the similar ways.

- Slow pion category
  The purpose of slow pion category is to distinguish the charged of D^* from $B_{\rm tag}$ decay. If the cms momenta (p_π^*) is smaller than 0.25 GeV/c and it is not positively identifies as kaon, it is classified into the slow pion category. The major contamination for this category is other pion than

- Λ category
  The tracks formed Λ baryons, which are reconstructed with $\Lambda \to p\pi$ decay, are classified into Λ category. In this category, the following discriminant is used for reconstruction of look-up tables: The invariant mass of reconstructed Λ , the flavor of Λ, the angle between the Λ momentum vector and the direction of the Λ decay vertex point from the interaction point, and the position difference of the two daughter tracks at the Λ decay vertex in the z direction.

- Kaon category
  The tracks that are not classified into any of above categories and required to have the likelihood ratio to distinguish proton from kaons less than 0.7, are assigned to the kaon category. This category is consists of tow sub-categories: the category for the event with K_S candidate and one for the event without K_S candidate. Because K_S can also carry out the strangeness from the cascade decay of $b \to c \to s$, the correlation of kaon charge and $B_{\rm tag}$ flavor becomes much weaker when K_S exists in a event. The dsicriminant are the charge of the track, cms momentum, the likelihood ratio to distinguish kaons from pions, and polar angle of the track.

In the second stage, event-level flavor tagging, the information obtained from each track category is gathered and the final $r \cdot q$ value is determined. The following discriminants are used: best $r \cdot q$ value from the lepton category ($(r \cdot q)_l$), best $r \cdot q$ value from the slow pion category ($(r \cdot q)_\pi$), and $r \cdot q$ value by the product of all outputs from the Λ and kaon categories ($(r \cdot q)_{\Lambda K}$). The third discriminant is defined as

$$(r \cdot q)_{\Lambda K} \equiv \frac{\prod_i (1 + q_i \cdot r_i) - \prod_i (1 - q_i \cdot r_i)}{\prod_i (1 + q_i \cdot r_i) + \prod_i (1 - q_i \cdot r_i)},$$

where the subscript i runs over the Λ candidates and the tracks in the kaon category. n this calculation, the correlation between Λ and kaon categories is considered because both are intend to observe the sum of the strangeness of $B_{\rm tag}$ decays. The number of bins for $(r \cdot q)_l$, $(r \cdot q)_\pi$ and $(r \cdot q)_{\Lambda K}$) are 25, 19 and 35 respectively. The look-up tables are constructed using the independent Monte Carlo sample of those used to construct the look-up tabkes for the track categories, in order to avoid any bias from a statistical correlation between the two stages. The efficiency that defined as the fraction of $r \neq 0$ events against total events is 99.6% in the Monte Carlo simulation.

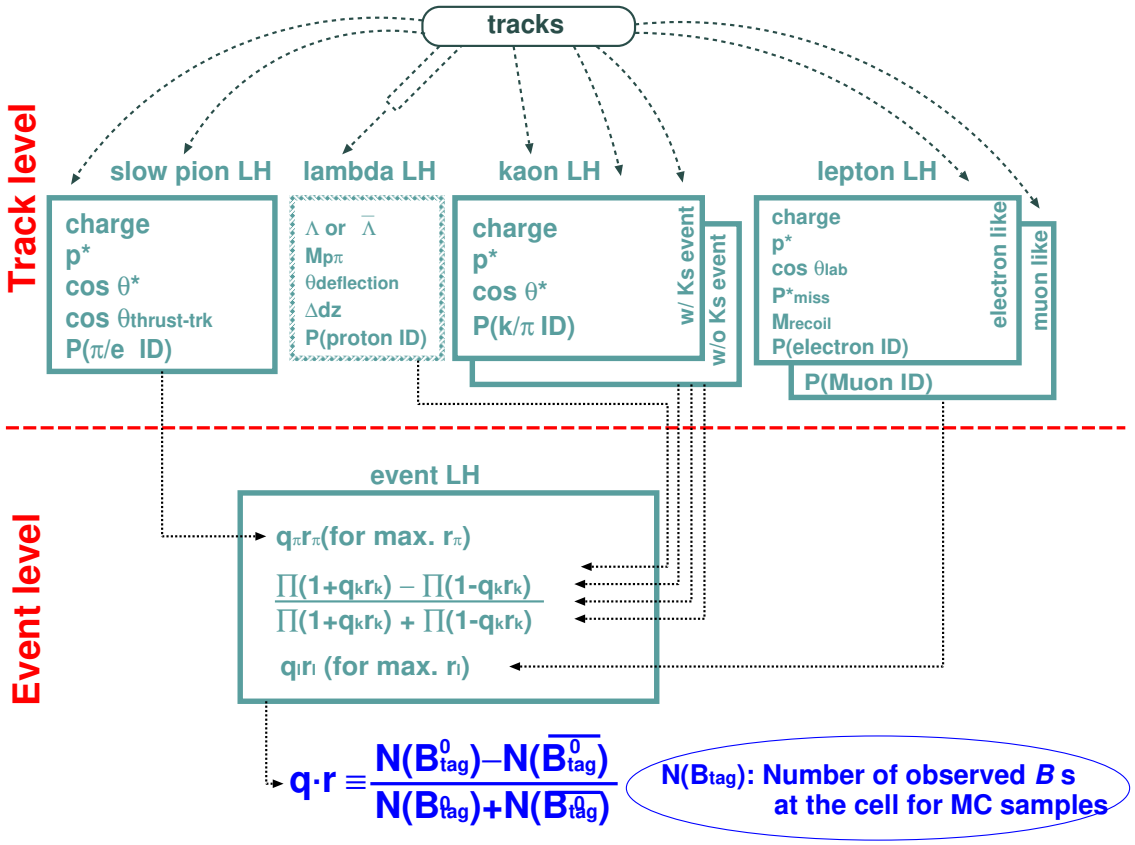

Figure 3.6: *The schematic view of the flavor tagging algorithm.*

3.5.3 Wrong tag fraction

Even high quality flavor tagging capability, mis-identifications of the flavor has to be considered. we define the probability to assign the wrong flavor as $w_{\rm tag}$ (wrong tag

fraction). A non-zero value of $w_{\rm tag}$ will dilute the result of CP asymmetry. For example, if the true numbers of B^0 and $\overline{B}^0$ are $N(B^0)$ and $N(\overline{B}^0)$, the true CP asymmetry is

$$\mathcal{A}_{CP}^{\rm true} \equiv \frac{N(B^0) - N(\overline{B}^0)}{N(B^0) + N(\overline{B}^0)}.$$

With realistic flavor tagging, the observed numbers of B^0 and $\overline{B}^0$ are

$$N(B^0)_{\rm obs} = \varepsilon_{\rm tag} \cdot [(1 - w_{\rm tag}) \cdot N(B^0) + w_{\rm tag} \cdot N(\overline{B}^0)],$$

and

$$N(B^0)_{\rm obs} = \varepsilon_{\rm tag} \cdot [w_{\rm tag} \cdot N(B^0) + (1 - w_{\rm tag}) \cdot N(\overline{B}^0)].$$

where $\varepsilon_{\rm tag}$ is flavor tagging efficiency. Therefore, the observed asymmetry is

$$\mathcal{A}_{CP}^{\rm obs} = \frac{N(B^0)_{\rm obs} - N(\overline{B}^0)_{\rm obs}}{N(B^0)_{\rm obs} + N(\overline{B}^0)_{\rm obs}} = (1 - 2w_{\rm tag}) \cdot \mathcal{A}_{CP}^{\rm true}.$$

The tagging quality factor r represent with wrong tag fraction of which value determined using Monte Carlo samples,

$$r \equiv 1 - 2w \tag{3.6}$$

Since this r is Monte Carlo dependent quantity, it is used only to sort data into six intervals of r: $0 < r \leq 0.25$, $0.25 < r \leq 0.5$, $0.5 < r \leq 0.625$, $0.625 < r \leq 0.75$, $0.75 < r \leq 0.875$, and $0.875 < r \leq 1$. The wrong-tag probabilities for each of these intervals, w_l $(l = 1, 6)$, are determined directly from the real data samples of B^0 decays to exclusively reconstructed self-tagging channels: $B^0 \to D^{*-} l^+ \nu$, $B^0 \to D^- \pi^+$, $B^0 \to D^{*-} \pi^+$, and $B^0 \to D^- \rho^+$, where $D^0 \to K^- \pi^+$, $D^0 \to K^- \pi^+ \pi^0$, and $D^0 \to K^- \pi^+ \pi^+ \pi^-$. Using these decay mode, we can know their flavors independently of the flavor tagging method.

When the flavors of both B mesons are known, we obtain w_l using time-dependent B^0-$\bar{B}^0$ mixing:

$$(N_{\rm OF} - N_{\rm SF})/(N_{\rm OF} + N_{\rm SF}) = (1 - 2w_l)\cos(\Delta m \Delta t), \tag{3.7}$$

where $N_{\rm OF}$ and $N_{\rm SF}$ are the numbers of opposite ($B^0\bar{B}^0 \to B^0\bar{B}^0$) and same ($B^0\bar{B}^0 \to B^0B^0, \bar{B}^0\bar{B}^0$) flavor events. We also have to consider the difference of the wrong tag fractions for between B^0 and $\overline{B}^0$, because our detector is made of particle so that detector response to particle/anti-particle is not same. Thus, the difference of the wrong-tag fractions is also determined from the same samples and implemented as $\Delta w_l (l = 1, 6)$. The obtained results are listed in Tabla 3.5.

3.6 Reconstruction of Proper Time Difference

In this section, we describe the reconstruction of proper time difference of $B^0 - \bar{B}^0$ pair. Since we can neither know the generation time of $B^0 - \bar{B}^0$ pair nor the flight length of them, we measure the decay vertex of B decayed into $J/\psi\pi^0$ (B_{CP}) and one of B decayed

l	r	w_l	Δw
1	0.000-0.250	$0.4637\ ^{+0.0046}_{-0.0056}$	$-0.0112\ ^{+0.0056}_{-0.0064}$
2	0.250-0.500	$0.3307\ ^{+0.0071}_{-0.0081}$	$0.0037^{+0.0097}_{-0.0088}$
3	0.500-0.625	$0.2305\ ^{+0.0089}_{-0.0087}$	$-0.0108^{+0.0100}_{-0.0097}$
4	0.625-0.750	$0.1631\ ^{+0.0079}_{-0.0066}$	$-0.0072\ ^{+0.0089}_{-0.0085}$
5	0.750-0.875	$0.1085\ ^{+0.0069}_{-0.0074}$	$0.0159^{+0.0090}_{-0.0090}$
6	0.875-1.000	$0.0202\ ^{+0.0043}_{-0.0048}$	$0.0035^{+0.0055}_{-0.0055}$

Table 3.5: *Wrong tag fraction parameters.*

into unspecified decay mode ($B_{\rm tag}$). The distance of two vertices in z direction, Δz is defined as follows:

$$\Delta z \equiv (z_{CP} - z_{\rm tag}) \tag{3.8}$$

where z_{CP} and $z_{\rm tag}$ is the z position of the B_{CP} and $B_{\rm tag}$ decay vertex, respectively. $B^0 - \bar{B}^0$ pair is produced nearly at rest in the $\Upsilon(4S)$ rest frame, because the mass of $\Upsilon(4S)$ is quite close to a sum of two B^0 mesons. Therefore, in the laboratory frame, both B^0 and $\bar{B}^0$ are given almost same momentum. In addition, $\Upsilon(4S)$ is boosted with $\beta\gamma = 0.425$ nearly along the z-axis defined as anti-parallel to the positron beam. Thus Δt can be determined from Δz as follows:

$$\Delta t \simeq \Delta z / \beta\gamma c \tag{3.9}$$

The decay vertices of B_{CP} and $B_{\rm tag}$ are reconstructed from the daughter charged tracks and interaction point profile (IP profile). The IP profile is the over wrap region of the HER and LER beam bunches. Since the accelerator condition varies injection by injection of the beam, and also shift even during the same run, we calculate the IP profile every 10,000 events. Typical width of the IP profile is 100 μm, 5 μm and 3-4 mm for x, y and z direction, respectively. To take into account the effect of B meson flight length, we express the "smearing" as a single Gaussian with the nominal flight length value, 21 μm, which is estimated from Monte Carlo simulation. The parameters of daughter tracks are obtained by the kinematic fit that is based on the least χ^2 method with Lagrange multiplier technique (IP constraint) [41]. The error of the decay point is calculated from the error of the track momentum and position, which are calibrated using cosmic ray tracks taking into account the difference between the tracks in hadronic events and cosmic ray tracks [42].

3.6.1 Vertex Reconstruction of B_{CP}

The vertex position for the $B^0 \to J/\psi\pi^0$ decay is reconstructed using lepton tracks from the J/ψ. It is required that the track is associated with at least one SVD hit in r-ϕ plane and at least two SVD hits in r-z plane. The IP profile constraint is applied to improve the vertex resolution. In addition to that, we are able to determine a vertex even in the case where only one track has enough associated SVD hits. Since vertex fit χ^2 correlate with the distance from IP to reconstructed vertex due to IP constraint in the r-z plane ,

we use ξ_{CP} as a parameter representing goodness of fit for vertex reconstruction [43]. It is based on z information only, defined as

$$\xi_{CP} = \frac{1}{2n}\sum_{i}^{n}(\frac{z_i^{after} - z_i^{before}}{\varepsilon_i^{before}})^2 \tag{3.10}$$

where n is the number of tracks, z_i^{before} and z_i^{after} are the position of each track in z direction, before and after vertex fit respectively. ε_i^{before} is error of z_i^{before}. We require $\xi_{CP} < 100$ to elminate poorly reconstructed vertices.

3.6.2 Vertex Reconstruction of $B_{\rm tag}$

The algorithm for the $f_{\rm tag}$ vertex reconstruction is chosen to minimize the effect of long-lived particles, secondary vertices from charmed hadrons and a small fraction of poorly reconstructed tracks [44]. We determine tag side ($B_{\rm tag}$) vertex from all the charged tracks except those used for CP side reconstruction. We require tracks having associated SVD hits, same as that for CP side, and also that error of z direction (σ_z) < 0.5 mm to reject poorly-reconstructed tracks. To suppress tracks from K_S, we remove tracks forming K_S mass and having dz greater than 0.5 mm, where dz is defined distance between vertex of B_{CP} and the track in r-ϕ plane. After these selection, we repeat vertex fitting with IP constraint until the reduced χ^2 (χ^2/ndf) gets less than 20, by removing the track that gives the largest contribution to χ^2, or remain only one track. However, we keep a lepton track if its momentum is greater than 1.1 GeV/c, because it comes from primary semi-leptonic B decay. Instead of the lepton track, we remove the track having second largest contribution to χ^2. We define $\xi_{\rm tag}$ in the same way as ξ_{CP} and require $\xi_{\rm tag} < 100$ to suppress poorly reconstructed vertices. After flavor tagging and vertex reconstruction, 91 of the 103 $B^0 \to J/\psi\pi^0$ candidates remain.

Chapter 4

Determination of CP Asymmetry

CP asymmetry parameters, $\mathcal{S}_{J/\psi\pi^0}$ and $\mathcal{A}_{J/\psi\pi^0}$ are determined by performing an unbinned maximum-likelihood fit to the Δt distribution for 91 $B^0 \to J/\psi\pi^0$ candidates. In this chapter, first, we describe the method of maximum-likelihood fit and probability density function. Then, the result and systematic uncertainties are described.

4.1 Maximum-likelihood fit Method

The maximum likelihood method is effective to find the values of unknown parameters. It is also useful for dealing with a small number of events and for taking event-by-event effect into account to the probability density function (PDF). To describe the principle of a maximum likelihood method, assume that we have a set of x_i values that we have observed from N independent measurements, where i is event suffix. For an unknown parameter α, the likelihood function $\mathcal{L}$ is expressed as

$$\mathcal{L}(\alpha) = \prod_{i=1}^{N} P_i(\alpha, x_i). \tag{4.1}$$

The $\mathcal{L}$ is the joint probability density for obtaining the PDF (P_i) to observe x_i values. Thus we finally maximize $\mathcal{L}$ as a function of α in order to fined the best value of α. In general, it is usually convenient to consider the logarithm of the likelihood function,

$$\ln \mathcal{L}(\alpha) = \sum_{i=1}^{N} \ln P_i(\alpha, x_i). \tag{4.2}$$

In the analysis, we obtain the most probable values of α by minimizing $-2\ln\mathcal{L}(\alpha)$ with MINUIT [45], which is a part of the numerical computing package distributed by CERN.

4.2 Probability Density Function

In this section, we construct the probability density function of the Δt distribution. The probability density function $\mathcal{P}(\mathcal{S}_{J/\psi\pi^0}, \mathcal{A}_{J/\psi\pi^0})$ consists of contributions from signal, background and outlier component. As for background, we separate into combinatorial back-

ground and $B \to J/\psi X$ background described in Section 3.4.

$$\begin{aligned}
&\mathcal{P}_i(\Delta t_i; \mathcal{S}_{J/\psi\pi^0}, \mathcal{A}_{J/\psi\pi^0}) \\
&= (1 - f_{\rm ol}) \int_{-\infty}^{\infty} \Big[(f_{\rm sig}\mathcal{P}_{\rm sig}(\Delta t_i; \mathcal{S}_{J/\psi\pi^0}, \mathcal{A}_{J/\psi\pi^0}) + f_{\rm bkg}^{J/\psi X}\mathcal{P}_{\rm bkg}^{J/\psi X}(\Delta t_i)) R_{\rm sig}(\Delta t_i - \Delta t') \\
&\quad + (f_{\rm comb})\mathcal{P}_{\rm bkg}^{\rm comb}(\Delta t_i) R_{\rm bkg}^{\rm comb}(\Delta t_i - \Delta t') \Big] d(\Delta t') + f_{\rm ol} P_{\rm ol}(\Delta t_i) \qquad (4.3)
\end{aligned}$$

where $f_{\rm sig}$, $f_{\rm bkg}^{J/\psi X}$, $f_{\rm bkg}^{\rm comb}$ are fraction of $B \to J/\psi\pi^0$ signal, $B \to J/\psi X$ background, combinatorial background respectively. Those fractions are normalized by $f_{\rm sig} + f_{\rm bkg}^{J/\psi X} + f_{\rm bkg}^{\rm comb} = 1$ and calculated from ΔE - $M_{\rm bc}$ distribution. The details is described in Section 4.3. $R_{\rm sig}$ and $R_{\rm bkg}^{J/\psi X}$ are resolution functions for signal and $B \to J/\psi X$ background events. $f_{\rm ol}$ is the fraction of outlier components. The outlier is a very long tail in the Δt distribution.

In the next subsection, we describe the probability density function for signal events, and the description of the signal resolution function is continued on the following subsection. Then, in the subsection 4.2.2, the probability density function for background events and corresponding resolution function are described.

4.2.1 PDF for Signal

We construct the probability density function for i-th signal event as

$$\begin{aligned}
\mathcal{P}_{\rm sig}(\Delta t_i; \mathcal{S}_{J/\psi\pi^0}, \mathcal{A}_{J/\psi\pi^0}) = \frac{e^{-|\Delta_{t_i}|/\tau_{B^0}}}{4\tau_{B^0}} \Big\{ 1 - q\Delta w_l \\
+ q \cdot (1 - 2w_l) \Big[\mathcal{S}_{J/\psi\pi^0} \sin(\Delta m \Delta t_i) + \mathcal{A}_{J/\psi\pi^0} \cos(\Delta m \Delta t_i) \Big] \Big\} \qquad (4.4)
\end{aligned}$$

where q is B flavor, and w_l is wrong tag fraction described in Section 3.5. We fix B^0 lifetime (τ_{B^0}) and mixing parameter (Δm) to the world averages [46].

Resolution function

$\mathcal{P}_{\rm sig}$ is convoluted with the resolution function for signal events, $R_{\rm sig}$. The $R_{\rm sig}$ consists of three components: the detector resolution ($R_{\rm det}$), smearing due to non-primary tracks ($R_{\rm np}$) on $B_{\rm tag}$ vertex, and smearing due to kinematic approximation. ($R_{\rm k}$). The overall resolution function is expressed as

$$R_{\rm sig}(\Delta t) = \int \int_{-\infty}^{+\infty} d(\Delta t') d(\Delta t'') R_{\rm det}(\Delta t - \Delta t') \times R_{\rm np}(\Delta t' - \Delta t'') R_{\rm k}(\Delta t''). \qquad (4.5)$$

Detector Resolution

The detector resolution is constructed from two part, full-reconstructed vertex of B_{CP} part ($R_{\rm ful}$) and associate B meson vertex of $B_{\rm tag}$ ($R_{\rm asc}$) expressed as

$$R_{\rm det}(\Delta t) = \int_{-\infty}^{+\infty} d(\Delta t') R_{\rm ful}(\Delta t - \Delta t') R_{\rm asc}(\Delta t') \qquad (4.6)$$

The $R_{\rm ful}$ and $R_{\rm asc}$ are parametrized as Gaussians of event-by-event determined Gaussian width. If a vertex is reconstructed with two or more tracks, the event-by-event Gaussian width is given by the errors of vertex calculated from track errors with the vertex quality variable of ξ. The ξ is defined like Equation 3.10, which is again expressed as

$$\xi = \frac{1}{2n}\sum_{i}^{n}(\frac{z_i^{after} - z_i^{before}}{\varepsilon_i^{before}})^2 \tag{4.7}$$

where n is the number of tracks, z_i^{before} and z_i^{after} are the position of each track in z direction, before and after vertex fit respectively. ε_i^{before} is error of z_i^{before}. It is represented by a reduced χ^2 project onto z axis. We require $\xi < 100$ to remove poorly reconstructed vertices. The correction factors of vertex errors, $s_{\rm ful}$ and $s_{\rm asc}$ are expressed as a first order polynomial of ξ,

$$s_{\rm ful} \equiv (s^0_{\rm ful} + s^1_{\rm ful}\xi),$$
$$s_{\rm asc} \equiv (s^0_{\rm asc} + s^1_{\rm asc}\xi).$$

Therefore, the detector resolution functions with multiple tracks is given by

$$R^{\rm multiple}_{\rm ful}(\delta z_{\rm ful}) = G(\delta z_{\rm ful}; s_{\rm ful}\sigma_{\rm ful}),$$
$$R^{\rm multiple}_{\rm asc}(\delta z_{\rm asc}) = G(\delta z_{\rm asc}; s_{\rm asc}\sigma_{\rm asc}),$$

where δz is defined as difference between a reconstructed z and the true z, $\delta z = z - z_{\rm true}$, and $\sigma_{\rm ful(asc)}$ is a vertex errors calculated from track errors for $B_{\rm ful(asc)}$ vertex. The G is a Gaussian function,

$$G(x;\sigma) \equiv \frac{1}{\sqrt{2\pi}\sigma}\exp\left(-\frac{x^2}{2\sigma^2}\right) \tag{4.8}$$

If a vertex is reconstructed with single track, the vertex quality cannot be defined. Thus, we define the resolution function as

$$R^{\rm single}(\delta z) = G(\delta z; s^{\rm single}\sigma), \tag{4.9}$$

where $s^{\rm single}$ is the global correction factor which are common to all the single track vertices. For single track case, vertex reconstruction for the fully reconstructed and associated B meson is expected to be same, so that we use the same resolution function for both vertices. The $R_{\rm det}$ parameters, $s^0_{\rm ful(asc)}$, $s^1_{\rm ful(asc)}$ and $s^{\rm single}$ are determined by the B meson lifetime measurement, which is studied using hadronic B meson decays such as $B^0 \to J/\psi K_S$, $B^0 \to J/\psi K^{*0}(K^{*0} \to K^-\pi^+)$, $B^0 \to D^{(*)-}\pi^+$, $B^0 \to D^{*-}\rho^+$, $B^+ \to J/\psi K^+$, and $B^+ \to \overline{D}^0\pi^+$ in the real data. The values for those parameters are listed in Table 4.1.

Smearing due to Non-primary Tracks

Most of associated B meson have a secondary vertex coming from $D(*)$ decays. Although we perform vertex fit to associated B vertex, we cannot removed completely the effect of those non-primary tracks. To take into account this effects, we construct the resolution function $R_{\rm np}$ which consists of prompt component expressed by Dirac's δ function

Parameter	value
$s^0_{\rm ful}$	$1.028\ ^{+0.053}_{-0.054}$
$s^1_{\rm ful}$	$0.073\ ^{+0.003}_{-0.003}$
$s^0_{\rm asc}$	$0.923\ ^{+0.032}_{-0.032}$
$s^1_{\rm asc}$	$0.024\ ^{+0.002}_{-0.002}$
$s^{\rm single}$	$1.000\ ^{+0.023}_{-0.023}$

Table 4.1: *The list of detector resolution function parameters.*

and exponential components for the smearing due to the contamination. The Dirac's δ function represents vertices without non-primary track effect.

The $R_{\rm np}$ is studied based on comparison of two different Monte Carlo samples. One is normal generic $B^0\overline{B}^0$ Monte carlo, the other one is special Monte carlo sample that all secondary short-lived ($\tau < 10^{-9}$ s) particles are forced to decay with zero lifetime. We reconstruct associated B vertices in two Monte carlo sample and compare difference of reconstructed z between them; $\delta z_{\rm asc} \equiv z_{\rm asc} - z^{noNP}_{\rm asc}$. The resolution function is defined as

$$\begin{aligned} R_{\rm np}(\delta z_{\rm asc}) &= f_\delta \times \delta(\delta z_{\rm asc}) + (1 - f_\delta) \\ &\times [f_p E_p(\delta z_{\rm asc}/c(\beta\gamma)_\Upsilon; \tau^p_{\rm np}) + (1 - f_p) E_n(\delta z_{\rm asc}/c(\beta\gamma)_\Upsilon; \tau^n_{\rm np})], \quad (4.10) \end{aligned}$$

where f_δ and f_p are the fraction of the prompt component and the $\delta z_{\rm asc} > 0$ component, respectively. $(\beta\gamma)_\Upsilon$ is the Lorentz boost factor for $\Upsilon(4S)$. E_p and E_n are defined as

$$E_p \equiv \frac{1}{\tau^p_{\rm np}} \exp\left(-\frac{x}{\tau^p_{\rm np}}\right) \text{ for } x > 0, \text{ otherwise } 0,$$
$$E_n \equiv \frac{1}{\tau^n_{\rm np}} \exp\left(-\frac{x}{\tau^n_{\rm np}}\right) \text{ for } x \leq 0, \text{ otherwise } 0.$$

If vertices are reconstructed with two or more tracks, $\tau^p_{\rm np}$ and $\tau^n_{\rm np}$ are parametrized as a function of vertex reconstruction quality ξ and vertex fit error in associated side B:

$$\tau^p_{\rm np} = S^3_{\rm asc}[\tau^0_p + \tau^1_p(1.0 + S^2_{\rm asc}\xi_{\rm asc})\sigma_{\rm asc}],$$
$$\tau^n_{\rm np} = S^3_{\rm asc}[\tau^0_n + \tau^1_n(1.0 + S^2_{\rm asc}\xi_{\rm asc})\sigma_{\rm asc}].$$

Where $S^2_{\rm asc}$ and $S^3_{\rm asc}$ are correction factors for While, for vertices reconstructed with single track, they are given by

$$\tau^p_{\rm np} = S^3_{\rm asc}[\tau^0_p + \tau^1_p\sigma_{\rm asc}],$$
$$\tau^n_{\rm np} = S^3_{\rm asc}[\tau^0_n + \tau^1_n\sigma_{\rm asc}],$$

because vertex quality cannot be defined with single track. Because of difference between neutral D lifetime (0.412 ps) and charged D lifetime (1.051 ps), the parameters for neutral B and charged B are determined separately. Table 4.2 shows the values for $R_{\rm np}$ parameters.

Smearing due to Kinematic Approximation

Parameters	Values	
	multiple tracks	single tracks
$S^2_{\rm asc}$	$0.060\ ^{+0.005}_{-0.004}$	
$S^2_{\rm asc}$	$1.044\ ^{+0.044}_{-0.043}$	
f_δ	$0.619\ ^{+0.023}_{-0.024}$	$0.773\ ^{+0.021}_{-0.022}$
f_p	$0.929\ ^{+0.003}_{-0.003}$	$0.453\ ^{+0.046}_{-0.046}$
τ_p^0 (ps)	$0.056\ ^{+0.006}_{-0.006}$	$0.453\ ^{+0.046}_{-0.046}$
τ_p^1	$0.725\ ^{+0.015}_{-0.014}$	$1.320\ ^{+0.064}_{-0.063}$
τ_n^0 (ps)	$0.025\ ^{+0.032}_{-0.032}$	$0.295\ ^{+0.086}_{-0.085}$
τ_n^1	$1.280\ ^{+0.064}_{-0.061}$	$1.476\ ^{+0.141}_{-0.134}$

Table 4.2: *List of $R_{\rm np}$ parameters determined with the Monte Carlo simulation.*

Since we calculate $\Delta t \simeq \Delta z/\beta\gamma c$ neglecting motion of B mesons in cms as we described in Section xx, smearing due to kinematic approximation, $R_{\rm k}$ is calculated analytically. The true time-difference between the fully reconstructed B meson and associate B meson is defined as $\Delta t_{\rm true} \equiv t_{\rm ful} - t_{\rm asc}$. Thus, the difference between the measured Δt and the true time-difference is expressed as

$$\begin{aligned} x \equiv \Delta t - \Delta t_{\rm true} &= \frac{\Delta z}{c(\beta\gamma)_\Upsilon} - (t_{\rm ful} - t_{\rm asc}) \\ &= \frac{c(\beta\gamma)_{\rm ful} t_{\rm ful} - c(\beta\gamma)_{\rm asc} t_{\rm asc}}{c(\beta\gamma)_\Upsilon} - (t_{\rm ful} - t_{\rm asc}) \\ &= [\frac{(\beta\gamma)_{\rm ful}}{(\beta\gamma)_\Upsilon} - 1] t_{\rm ful} - [\frac{(\beta\gamma)_{\rm asc}}{(\beta\gamma)_\Upsilon} - 1] t_{\rm asc}, \end{aligned} \tag{4.11}$$

where $(\beta\gamma)_{\rm ful}$ and $(\beta\gamma)_{\rm asc}$ are the Lorentz boost factor for the fully reconstructed B and associate B mesons, respectively. The ratio of $(\beta\gamma)_{\rm ful}/(\beta\gamma)_\Upsilon$ and $(\beta\gamma)_{\rm asc}/(\beta\gamma)_\Upsilon$ are given by

$$(\beta\gamma)_{\rm ful}/(\beta\gamma)_\Upsilon = \frac{E_B^{cms}}{m_B c^2} + \frac{p_B^{cms} cos\theta_B^{cms}}{m_B c \beta_\Upsilon}, \tag{4.12}$$

$$(\beta\gamma)_{\rm asc}/(\beta\gamma)_\Upsilon = \frac{E_B^{cms}}{m_B c^2} - \frac{p_B^{cms} cos\theta_B^{cms}}{m_B c \beta_\Upsilon}, \tag{4.13}$$

where E_B^{cms}, m_B, p_B^{cms} and $cos\theta_B^{cms}$ are the energy of B meson, the B meson mass, the B momentum and the polar angle of the fully reconstructed B meson in the cms frame, respectively. $\beta_\Upsilon = 0.391$ is the velocity of $\Upsilon(4S)$ in units of c. Defining $a_k \equiv E_B^{cms}/m_B c^2$ and $c_k \equiv p_B^{cms} cos\theta_B^{cms}/m_B c \beta_\Upsilon$, x can be expressed as

$$x = (a_k + c_k - 1) t_{\rm ful} - (a_k - c_k - 1) t_{\rm asc} \tag{4.14}$$

The probability density function for $t_{\rm ful}$ and $t_{\rm asc}$ are represented by the decay time as

$$E_p(t_{{\rm ful};\tau_B}) = \frac{1}{\tau_B} \exp\left(-\frac{t_{\rm ful}}{\tau_B}\right), \tag{4.15}$$

$$E_p(t_{{\rm asc};\tau_B}) = \frac{1}{\tau_B} \exp\left(-\frac{t_{\rm asc}}{\tau_B}\right). \tag{4.16}$$

Therefor the probability density function of obtaining x and true Δt is given by

$$F(x, \Delta t_{\rm true}) = \int\int_0^\infty dt_{\rm ful} dt_{\rm asc} E_p(t_{{\rm ful};\tau_B}) E_p(t_{{\rm asc};\tau_B}) \delta(\Delta t_{\rm true} - (t_{\rm ful} - t_{\rm asc})) \times \delta(x - [(a_k + c_k - 1)t_{\rm ful} - (a_k - c_k - 1)t_{\rm asc}]), \quad (4.17)$$

and the probability density function for $\Delta t_{\rm true}$ is given by

$$F(\Delta t_{\rm true}) = \int\int_0^\infty dt_{\rm ful} dt_{\rm asc} E_p(t_{ful;\tau_B}) E_p(t_{asc;\tau_B}) \delta(\Delta t_{\rm true} - (t_{\rm ful} - t_{\rm asc})). \quad (4.18)$$

The $R_k(x)$ is expressed as the conditional probability density function:

$$R_k(x) = \begin{cases} E_p(x - [\ (a_k - 1)\Delta t_{\rm true} + c_k|\Delta t_{\rm true}|\ ];\ |c_k|\tau_B)\ (c_k > 0) \\ \delta(x - 1(a_k - 1)\Delta t_{\rm true})(c_k = 0) \\ E_n(x - [\ (a_k - 1)\Delta t_{\rm true} + c_k|\Delta t_{\rm true}|\ ];\ |c_k|\tau_B)\ (c_k < 0) \end{cases}$$

Outlier

There still remains a very long tail that cannot be described by the resolution function above. The outlier term expresses this long tile with single Gaussian, which is given by

$$P_{\rm ol}(\Delta t) = G(\Delta t; \sigma_{\rm ol}) \quad (4.19)$$

Since the outlier has a very wide Gaussian width ($\sim$ 40 ps), the effects of the lifetime convolution and other resolution components are neglected.

This long tail is considered to be caused by the mis-reconstruction of tracks, and independent on whether the event is signal or background. Therefore the same fraction and shape of outlier is assigned to both signal and background events as shown in Eq. 4.3. The fraction of outlier $f_{\rm ol}$ is typically less than 10^{-3} for multiple track vertices and $\sim 10^{-2}$ for single track vertices.

4.2.2 Background Shape

The background is categorized into two components. One is B decays containing a real J/ψ ($B \to J/\psi X$) decay into dilepton, and the other is combinatorial background which comes from random combinations of particles in $B\overline{B}$ decays and continuum events contribute.

PDF for Inclusive J/ψ decay background

As we describe in Section 3.4, we assume that $B \to J/\psi X$ background has no contribution to CP asymmetry, because the contributions of $CP = -1$ and $+1$ components in the $B \to J/\psi X$ background in the signal region are found to be almost the same and the CP violation effect is largely cancelled. Therefor background function of inclusive J/ψ decays consists of lifetime component, which expressed as

$$\mathcal{P}_{\rm bkg}^{J/\psi X}(\Delta t) = \frac{e^{-|\Delta_t|/\tau_{\rm bkg}^{\rm J/\psi X}}}{4\tau_{\rm bkg}^{\rm J/\psi X}} \Big\{ 1 - q\Delta w_l \Big\}, \quad (4.20)$$

$\tau_{\rm bkg}^{\rm J/\psi X}$ is the lifetime of $B \to J/\psi X$ decays, which determined from inclusive J/ψ Monte Carlo study. $\mathcal{P}_{\rm bkg}^{J/\psi X}(\Delta t)$ is convoluted with resolution function for $B \to J/\psi X$ background events, $R_{\rm bkg}^{J/\psi X}$. We model $R_{\rm bkg}^{J/\psi X}$ using the signal resolution function because vertex reconstruction for both signal and $B \to J/\psi X$ background events is based on lepton tracks from J/ψ. Figure.4.1 shows result of the lifetime fit to Δt distribution. We obtain $\tau_{\rm bkg}^{\rm J/\psi X} = 1.277 \pm 0.071$ (psec).

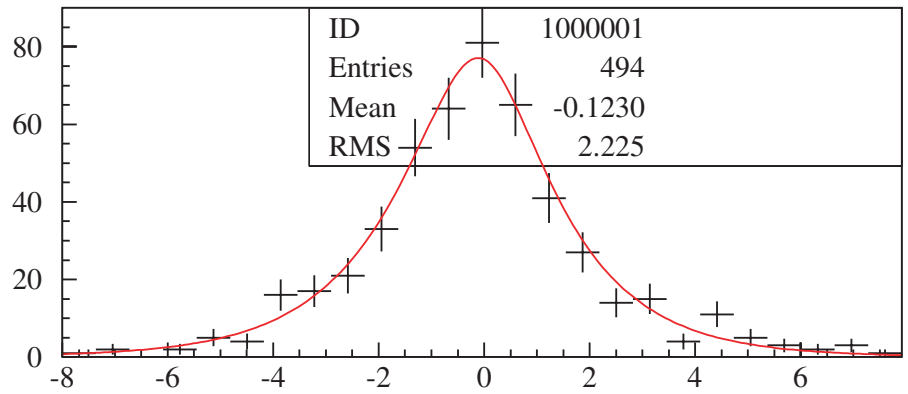

Figure 4.1: $\tau_{\rm bkg}^{\rm J/\psi X}$ *is detrmined by fit to* Δt *distribution for inclusive* J/ψ *Monte carlo sample.*

PDF for Combinatorial background

For combinatorial background, we consider two components. One is "prompt" background , that has narrower Δt as describing delta function, because B_{CP} is shifted toward to B_{tag} vertex by the background event reconstructed from contaminating track. The other is lifetime component. When vertices of B_{CP} and B_{tag} are reconstructed correctly, it tends to show lifetime distribution. PDF is defined as

$$\mathcal{P}_{\rm bkg}^{\rm comb}(\Delta t) = f_\delta \delta(\Delta t - \mu_d) + (1 - f_\delta) \exp(-\frac{|\Delta t - \mu_l|}{\tau_{\rm bkg}^{\rm comb}}), \tag{4.21}$$

where $\mu_d(\mu_l)$ is the mean shift of prompt(lifetime) component, and f_δ is the fraction of prompt component. $\tau_{\rm bkg}^{\rm comb}$ is lifetime for background. We convolute this PDF with the resolution function expressed as sum of two Gaussians.

$$R_{\rm bkg}^{\rm comb}(\Delta t) = (1 - f_{tail}) G(\Delta t; \mu_{main}, \sigma_{main}) + f_{tail} G(\Delta t; \mu_{tail}, \sigma_{tail}) \tag{4.22}$$

where,

$$\begin{aligned} \sigma_{main} &= S_{main} \cdot \sigma_{vtx} \\ \sigma_{tail} &= S_{tail} \cdot \sigma_{vtx} \\ \sigma_{vtx} &= \sqrt{\sigma_{\rm rec}^2 + \sigma_{\rm asc}^2} \end{aligned}$$

$S_{main}(S_{tail})$ is scale factor for main(tail) part of resolution function, Since it is not enough statistics of sideband data to determine parameters, $S_{main}, S_{tail}, f_\delta, f_{tail}, \tau_{\rm bkg}^{\rm comb}, \mu_d, \mu_l$, we use same parameters as ones for $B \to J/\psi K_S$. Table 4.3 shows each parameter value.

parameter	multiple tracks	single track
S_{main}	$1.524\ ^{+0.116}_{-0.124}$	$1.022\ ^{+0.110}_{-0.110}$
S_{tail}	6.0	3.0
f_{tail}	0.0	0.0
f_{δ}	$0.692\ ^{+0.073}_{-0.088}$	$0.498\ ^{+0.106}_{-0.115}$
$\tau^{\rm comb}_{\rm bkg}$	$1.745\ ^{+0.237}_{-0.193}$	
μ_l	$-0.036\ ^{+0.202}_{-0.183}$	
μ_d	$-0.036\ ^{+0.046}_{-0.046}$	

Table 4.3: *Combinatorial background PDF and resolution function parameters.*

4.3 Signal and Background Probabilities

To assign the probabilities for signal ($f_{\rm sig}$), $B \to J/\psi X$ background ($f^{J/\psi X}_{\rm bkg}$) and combinatorial background ($f^{\rm comb}_{\rm bkg}$) event by event, we perform fit to ΔE - $M_{\rm bc}$ limited region, -0.1 GeV $< \Delta E <$ 0.2 GeV and 5.2 GeV/c^2 $< M_{\rm bc} <$ 5.3 GeV/c^2 with unbinned-maximum likelihood fit. f_sig, $f^{J/\psi X}_{\rm bkg}$ and $f^{\rm comb}_{\rm bkg}$ are defined as a function of $M_{\rm bc}$ and ΔE:

$$f_{\rm sig}(M_{\rm bc},\Delta E) \equiv \frac{F_{\rm sig}(M_{\rm bc},\Delta E)}{F_{\rm sig}(M_{\rm bc},\Delta E)+F^{J/\psi X}_{\rm bkg}(M_{\rm bc},\Delta E)+F^{\rm comb}_{\rm bkg}(M_{\rm bc},\Delta E)}, \quad (4.23)$$

$$f^{J/\psi X}_{\rm bkg}(M_{\rm bc},\Delta E) \equiv \frac{F^{J/\psi X}_{\rm bkg}(M_{\rm bc},\Delta E)}{F_{\rm sig}(M_{\rm bc},\Delta E)+F^{J/\psi X}_{\rm bkg}(M_{\rm bc},\Delta E)+F^{\rm comb}_{\rm bkg}(M_{\rm bc},\Delta E)}, \quad (4.24)$$

$$f^{\rm comb}_{\rm bkg}(M_{\rm bc},\Delta E) \equiv \frac{F^{\rm comb}_{\rm bkg}(M_{\rm bc},\Delta E)}{F_{\rm sig}(M_{\rm bc},\Delta E)+F^{J/\psi X}_{\rm bkg}(M_{\rm bc},\Delta E)+F^{\rm comb}_{\rm bkg}(M_{\rm bc},\Delta E)}, \quad (4.25)$$

where $F_{\rm sig}(M_{\rm bc},\Delta E)$ is defined as:

$$F_{\rm sig}(M_{\rm bc},\Delta E) \equiv \frac{P_{\rm sig}(M_{\rm bc})P_{\rm sig}(\Delta E)}{\int\int_{\text{signal region}} d(M_{\rm bc})d(\Delta E)P_{\rm sig}(M_{\rm bc})P_{\rm sig}(\Delta E)}. \quad (4.26)$$

$P_{\rm sig}(M_{\rm bc})$ and $P_{\rm sig}(\Delta E)$ are signal probability density functions depending on $M_{\rm bc}$ and ΔE, respectively. $F^{J/\psi X}_{\rm bkg}(M_{\rm bc},\Delta E)$ and $F^{\rm comb}_{\rm bkg}(M_{\rm bc},\Delta E)$ are constructed in the same way. In the following, we describe each probability density function for signal, $B \to J/\psi X$ background and combinatorial background.

$M_{\rm bc}$ - ΔE PDF for Signal

The signal distribution is modeled with a two-dimensional function which is Gaussian in $M_{\rm bc}$ and a Crystal Ball line shape [47] in ΔE. Therefor, $P_{\rm sig}(M_{\rm bc})$ and $P_{\rm sig}(\Delta E)$ are expressed as:

$$P_{\rm sig}(M_{\rm bc}) = \frac{1}{\sqrt{2}\pi\sigma_{M_{\rm bc}}}\exp(-\frac{(M_{\rm bc}-\mu_{M_{\rm bc}})^2}{2\sigma^2_{M_{\rm bc}}}), \quad (4.27)$$

$$P_{\rm sig}(\Delta E) = \begin{cases} \exp\left[-\frac{1}{2}\left(\frac{\mu_{\Delta E}-\Delta E}{\sigma_{\Delta E}}\right)^2\right], \text{ for } \Delta E > \mu_{\Delta E}-\alpha\cdot\sigma_{\Delta E}, \\ \exp\left(\frac{\alpha^2}{2}\right)\left(\frac{\alpha}{n}\left(\frac{\mu_{\Delta E}-\Delta E}{\sigma_{\Delta E}}-\alpha\right)+1\right)^{-n}, \\ \qquad\qquad \text{for } \Delta E < \mu_{\Delta E}-\alpha\cdot\sigma_{\Delta E}, \end{cases}$$

where α and n is empirical parameters which is expressed asymmetric distribution. Since the number of candidate events is not sufficient to obtain precisely the shape parameters of these functions, the shape parameters are determined by the signal Monte Carlo and held fixed in the fit. The $M_{\rm bc}$ and ΔE distributions of signal Monte Calro sample is shown in Fig.4.2 and Fig.4.3. Table 4.4 shows the values of each parameters obtained from fit to these distribution.

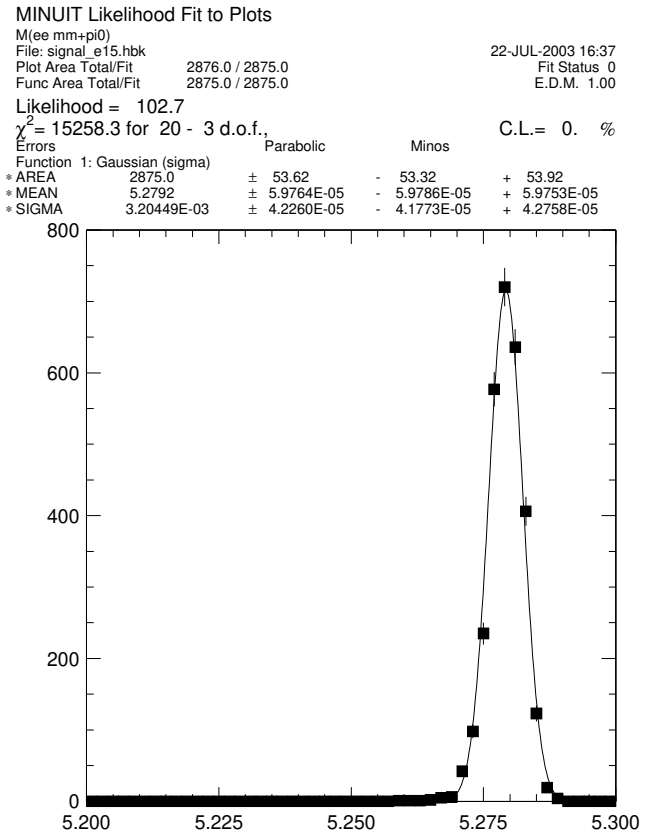

Figure 4.2: *The fit results on $M_{\rm bc}$ distribution of the signal Monte Carlo for $-0.10GeV < \Delta E < 0.05GeV$. The fitting function is Gaussian.*

$M_{\rm bc}$ - ΔE PDF for $B \to J/\psi X$ background

According to a Monte carlo study described in Section 3.4, the $B \to J/\psi X$ background forms a small peak in the $M_{\rm bc}$ projection. Therefore we parametrize this contribution with a sum of a Gaussian and a phase-space-like background function (ARGUS function) [48]

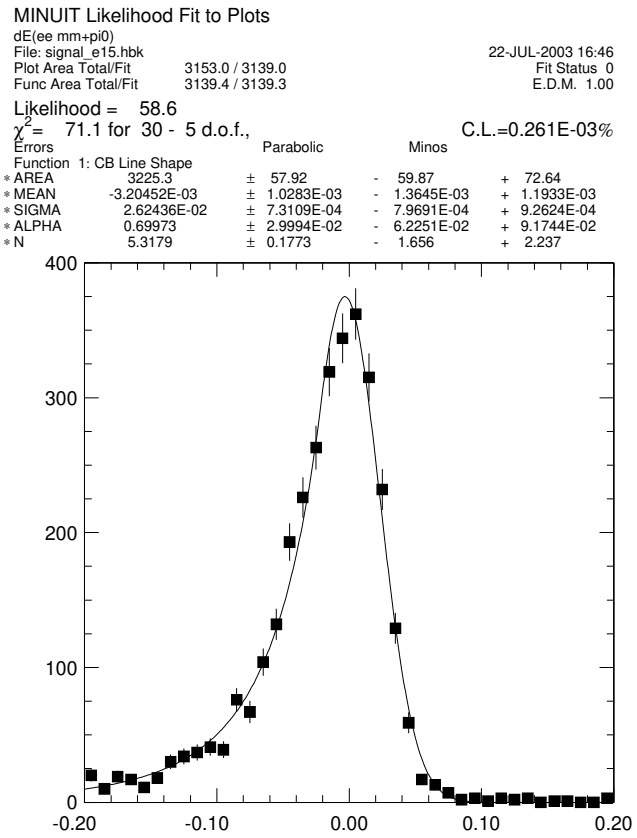

Figure 4.3: *The fit results on ΔE distribution of the signal Monte Carlo for* $5.27GeV/c^2 < M_{\rm bc} < 5.29GeV/c^2$. *The fitting function is Crystal Ball lineshape.*

	Parameter	Fit result
$M_{\rm bc}$	$\mu_{M_{\rm bc}}$	5.2792 (GeV)
(Gaussian)	$\sigma_{M_{\rm bc}}$	3.2045 (MeV)
	$\mu_{\Delta E}$	-3.2045 (MeV)
ΔE	$\sigma_{\Delta E}$	26.2436 (MeV)
(Crystal Ball)	α	0.6997
	n	5.3179

Table 4.4: *Parameters obtained from fit to $M_{\rm bc}$ and ΔE distribution of the signal Monte Carlo. These results are used for calculation of an event-by-event signal probability.*

in $M_{\rm bc}$ and an exponential function for ΔE:

$$P_{\rm bkg}^{J/\psi X}(M_{\rm bc}) = \frac{1}{\sqrt{2}\pi\sigma_{J/\psi X}}\exp(-\frac{(M_{\rm bc}-\mu_{J/\psi X})^2}{2\sigma^2_{J/\psi X}}) \quad (4.28)$$

$$+ M_{bc}\sqrt{1-\left(\frac{M_{bc}}{E_{beam}}\right)^2}\exp\left(N_{J/\psi X}\left[1-\left(\frac{M_{bc}}{E_{beam}}\right)^2\right]\right), \quad (4.29)$$

$$P_{\rm bkg}^{J/\psi X}(\Delta E) = \exp(C_{J/\psi X}\Delta E) \quad (4.30)$$

where $N_{J/\psi X}$ and $C_{J/\psi X}$ are scale factors for the exponential. E_{beam} is beam energy to be 5.29 GeV. These parameters determined from fit to the inclusive J/ψ Monte Carlo are listed in Table 4.5.

	Parameter	Fit result
$M_{\rm bc}$ (Gaussian)	$\mu_{J/\psi X}$	5.2790 (GeV)
	$\sigma_{J/\psi X}$	4.1936 (MeV)
(ARGUS)	$N_{J/\psi X}$	-11.265
ΔE (exponential)	$C_{J/\psi X}$	-8.7336

Table 4.5: *Parameters obtained from fit to $M_{\rm bc}$ and ΔE distribution of $B \to J/\psi X$ Monte Carlo. These results are used for calculation of an event-by-event signal probability.*

$M_{\rm bc}$ - ΔE PDF for combinatorial background

For combinatorial background, we use a Chebyshev polynomial function for ΔE and an ARGUS function for $M_{\rm bc}$.

$$P_{\rm bkg}^{\rm comb}(M_{\rm bc}) = M_{bc}\sqrt{1-\left(\frac{M_{bc}}{E_{beam}}\right)^2}\exp\left(N_{\rm comb}\left[1-\left(\frac{M_{bc}}{E_{beam}}\right)^2\right]\right) \quad (4.31)$$

$$P_{\rm bkg}^{\rm comb}(\Delta E) = 1.0 + C_{\rm comb}\left(\frac{2\Delta E}{\Delta E_{max}-\Delta E_{min}}-1\right), \quad (4.32)$$

where $C_{\rm comb}$ is a slope of ΔE. ΔE_{max} and ΔE_{min} are 0.2 GeV and -0.1 GeV, respectively. These values are determined from fit to the real data simultaneously, as described the following. Table 4.6 is the list of each parameters.

	Parameter	Fit result
$M_{\rm bc}$ (ARGUS)	$N_{\rm comb}$	-7.3906
ΔE (linear)	$C_{\rm comb}$	-0.3013

Table 4.6: *Parameters obtained from fit to $M_{\rm bc}$ and ΔE distribution of the real data.*

Above these functions using the determination of signal and background probabilities are listed in Table.4.7. As for inclusive J/ψ decay background, expected number of events in the signal box is 6.5 events, which is estimated from Monte carlo study (Section 3.4). We fix this number in the fit, while the overall signal yield is allowed to float. Figure 4.4 shows the result of fit to the M_{bc}-ΔE distribution. Estimated signal and background yield in the signal region are listed in Table 4.8. From the results, the purity of the $B^0 \to J/\psi\pi^0$ candidates is estimated to be (86±11)%.

	$M_{\rm bc}$	ΔE
Signal	Gaussian	Crystal Ball
Combinatrial BG	ARGUS	Chebyshev polynomial
$B \to J/\psi X$ BG	Gaussian + ARGUS	exponential

Table 4.7: *Functions for unbinned-maximum likelihood fit to ΔE - $M_{\rm bc}$.*

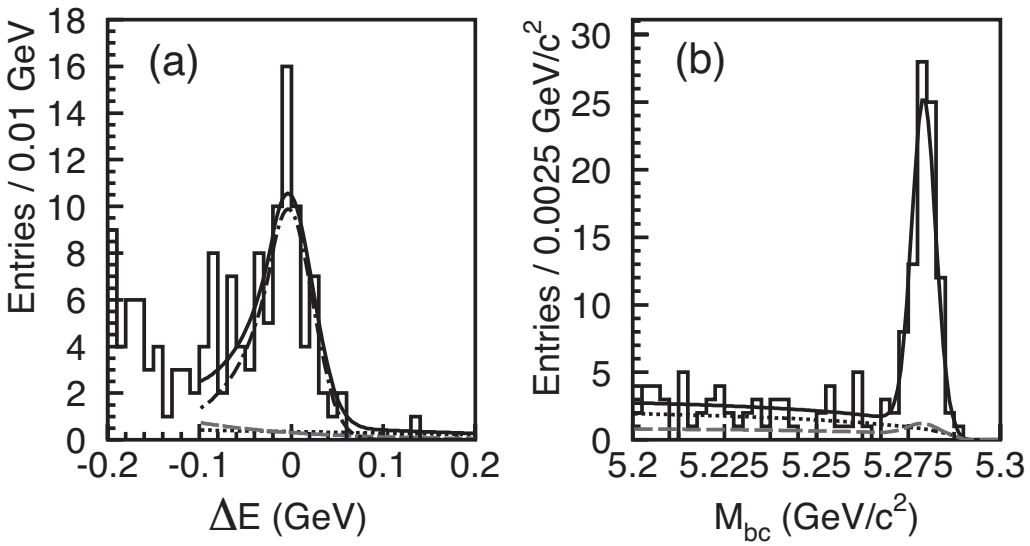

Figure 4.4: *(a) ΔE distribution for events in the $M_{\rm bc}$ signal region and (b) $M_{\rm bc}$ distribution for events in the ΔE signal region, for $B^0 \to J/\psi\pi^0$ candidates. The superimposed curves show fitted contributions from signal (dot-dashed line, plotted only in ΔE distribution), $B \to J/\psi X$ background (dotted line), combinatorial background (dashed line) and the sum of all the contributions (solid line).*

	Fit result (events)
N(signal)	78.69 ± 9.82
N(combinatorial background)	5.81 ± 2.90
N($B \to J/\psi X$ background)	6.50(fixed)

Table 4.8: *Signal fraction : Result of fit to* $M_{\rm bc}$ - ΔE *distribution.*

4.4 Results of Fit to the Δt Distribution

We determine the CP asymmetry parameters by performing the unbinned maximum likelihood fit to the reconstructed Δt distribution of 91 $B^0 \to J/\psi\pi^0$ candidate events. We use the probability density function described as Equation (4.3),

$$\begin{aligned}
&\mathcal{P}_i(\Delta t_i; \mathcal{S}_{J/\psi\pi^0}, \mathcal{A}_{J/\psi\pi^0}) \\
&= (1 - f_{\rm ol}) \int_{-\infty}^{\infty} \Big[(f_{\rm sig}\mathcal{P}_{\rm sig}(\Delta t_i; \mathcal{S}_{J/\psi\pi^0}, \mathcal{A}_{J/\psi\pi^0}) + f_{\rm bkg}^{J/\psi X}\mathcal{P}_{\rm bkg}^{J/\psi X}(\Delta t_i)) R_{\rm sig}(\Delta t_i - \Delta t') \\
&\quad + (f_{\rm comb})\mathcal{P}_{\rm bkg}^{\rm comb}(\Delta t_i) R_{\rm bkg}^{\rm comb}(\Delta t_i - \Delta t') \Big] d(\Delta t') + f_{\rm ol} P_{\rm ol}(\Delta t_i)
\end{aligned}$$

In the fit, free parameters are $\mathcal{S}_{J/\psi\pi^0}$ and $\mathcal{A}_{J/\psi\pi^0}$, and the other parameters fixed to be determined values as described in previous sections.

$\mathcal{S}_{J/\psi\pi^0}$ and $\mathcal{A}_{J/\psi\pi^0}$ are determined by maximizing the likelihood function

$$L = \prod_i P_i(\Delta t_i; \mathcal{S}_{J/\psi\pi^0}, \mathcal{A}_{J/\psi\pi^0}), \tag{4.33}$$

where the product runs over all events.

The fit results in the CP-violating parameters,

$$\begin{aligned}
\mathcal{S}_{J/\psi\pi^0} &= -0.72 \pm 0.42({\rm stat}) \\
\mathcal{A}_{J/\psi\pi^0} &= -0.01 \pm 0.29({\rm stat}),
\end{aligned} \tag{4.34}$$

Figure 4.5 (a) and (b) show the Δt distributions for $\overline{B}^0 \to J/\psi\pi^0$ ($q = +1$) and $B^0 \to J/\psi\pi^0$ ($q = -1$) event samples respectively. Figure 4.6 shows the raw asymmetry in each Δt bin without background subtraction, which is defined by

$$A \equiv \frac{N_{q=+1} - N_{q=-1}}{N_{q=+1} + N_{q=-1}}, \tag{4.35}$$

where $N_{q=+1}(N_{q=-1})$ is the number of observed candidates with $q = +1(-1)$. The curve shows the result of the unbinned maximum-likelihood fit to the Δt distributions.

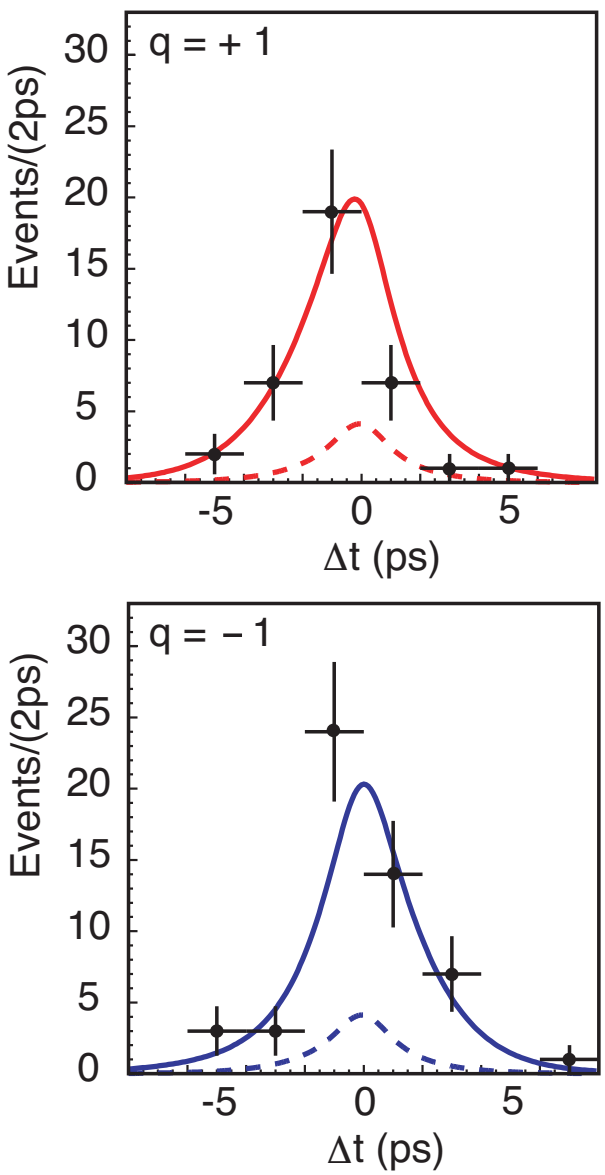

Figure 4.5: *The Δt distributions for $\overline{B}^0 \to J/\psi\pi^0$ ($q = +1$) and $B^0 \to J/\psi\pi^0$ ($q = -1$) candidates. The solid curves show the results of the fit, and dashed curves show the background distributions.*

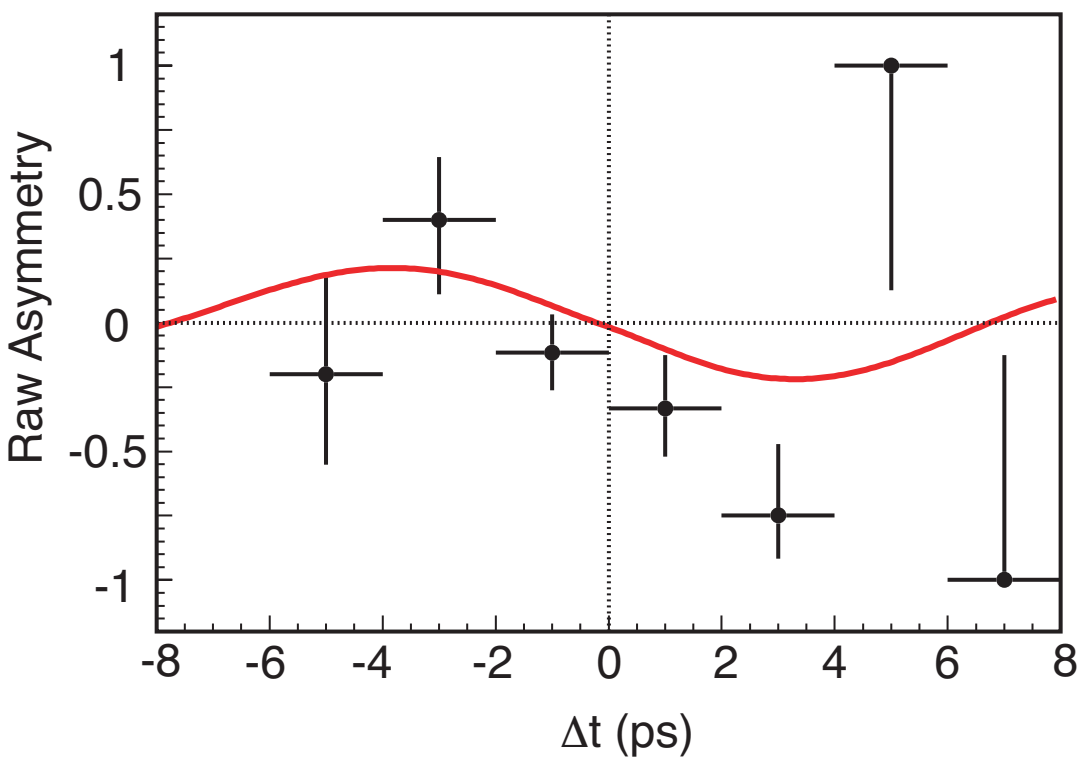

Figure 4.6: *The asymmetry, A, in each Δt bin for $B^0 \to J/\psi\ \pi^0$ candidates. The curve shows the result of the unbinned maximum-likelihood fit.*

4.5 Systematic Uncertainties

To estimate systematic uncertainties, we repeat CP fit varying each parameter. Parameters obtained from data are varied by $\pm 1\sigma$, and those from Monte Carlo are varied by $\pm 2\sigma$. Breakdown of systematic uncertainties are shown in Table 4.9. The following sources for systematic errors are considered.

- Wrong tag fraction
  We vary w_l and Δw by their errors for each r region as shown in Table 3.5. The results are 0.025 and 0.014 for $\mathcal{S}_{J/\psi\pi^0}$ and $\mathcal{A}_{J/\psi\pi^0}$.

- Signal fraction
  We vary signal fraction parameters for function of ΔE and $M_{\rm bc}$ distribution and repeat fit procedure.

- Background shape
  The parameters shown in table 4.3 are varied by $\pm 1\sigma$. Since those parameters determined from sideband data of $B \to J/\psi K_S$, this result are doubled to avoid underestimation.

- Physics Parameter
  We use PDG value for B meson lifetime and $B^0\bar{B}^0$-mixing parameter [46],

  $$\begin{aligned} \tau_{B^0} &= 1.537 \pm 0.015 ps, \\ \Delta m &= 0.502 \pm 0.007 ps^{-1}, \end{aligned}$$

  The systematic error is estimated by varying those parameters by their errors.

- Resolution function
  We estimate the uncertainty in resolution function by repeating CP fit with parameters varied by $\pm 1\sigma$

- Fit bias
  We perform CP fit using signal Monte Carlo. We estimate the error from the difference between input value and fitted value.

- Vertex reconstruction
  The sources are track and vertex selection, charge asymmetry of charged tracks, IP profile, scale error.

- CP asymmetry of Inclusive J/ψ background
  We perform CP fit with applying same probability density function as one for signal to inclusive J/ψ background.

4.6 Validity Check

In order to establish the validity of the analysis, several tests are performed.

parameter	$\mathcal{S}_{J/\psi\pi^0}$	$\mathcal{A}_{J/\psi\pi^0}$
Wrong tag fraction	0.025	0.014
Signal fraction	0.023	0.016
Background shape	0.014	0.0065
Physics (τ_B, Δm_B)	0.0019	0.0071
Resolution function	0.010	0.0061
Fit bias	0.033	0.0074
Vertexing	0.062	0.018
CP asymmetry of $B \to J/\psi X$	0.029	0.013
Total	0.085	0.034

Table 4.9: *Systematic uncertainties.*

4.6.1 Lifetime Fit

We perform lifetime fit to $B^0 \to J/\psi\pi^0$ candidates for checking the validity of the Δt reconstruction, the parametrization of the resolution function and background shapes. The result is

$$\tau_{B^0} = 1.362^{+0.219}_{-0.188} \text{ ps}$$

as shown in Figure 4.7, where errors are statistical only. It is consistent with the world average [46].

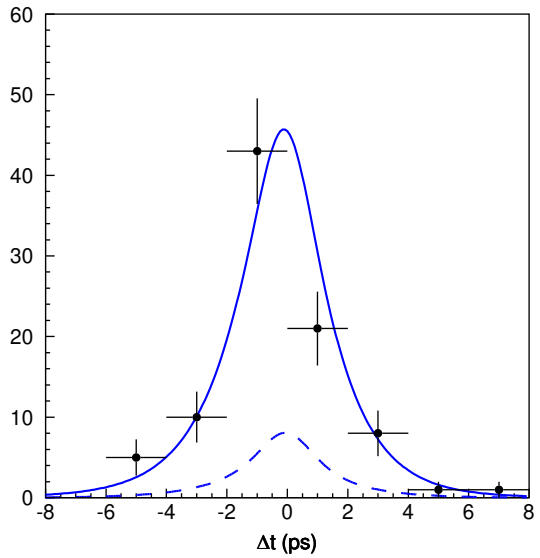

Figure 4.7: *Lifetime fit*

4.6.2 Toy Monte Carlo study

The validity of our fit procedure and obtained error are checked by the study of Monte carlo pseudo-experiment. We generate 1000 pseudo-experiment for varying input value

$\mathcal{S}_{J/\psi\pi^0}(\mathcal{A}_{J/\psi\pi^0})$ with fixed $\mathcal{A}_{J/\psi\pi^0}(\mathcal{S}_{J/\psi\pi^0}) = 0$. Each experiment contains 91 event which is the same number as real data. Figure 4.10 shows the mean value of fit results for $\mathcal{S}_{J/\psi\pi^0}$ and $\mathcal{A}_{J/\psi\pi^0}$. From this result, we obtain good linearity.

For checking validation of error, we generate 5000 pseudo-experiment with ($\mathcal{S}_{J/\psi\pi^0}$, $\mathcal{A}_{J/\psi\pi^0}$) = (0, 0). Figure 4.8 is the pull distribution for $\mathcal{S}_{J/\psi\pi^0}$ and $\mathcal{A}_{J/\psi\pi^0}$. The pull is defined $X_{fit} - X_{input}/\ (Error\ of\ fit)$, where X_{fit} and X_{input} are fit result and input value of pseudo-experiment, respectively. This result indicate that our fit procedure estimates error of $\mathcal{S}_{J/\psi\pi^0}$ and $\mathcal{A}_{J/\psi\pi^0}$ correctly. Figure 4.9 shows positive and negative MINOS error. In these plots, we take positive(negative) error when X_{fit} is lager(smaller) than X_{input}. MINOS error obtained from data is consistent with expectation of pseudo-experiment.

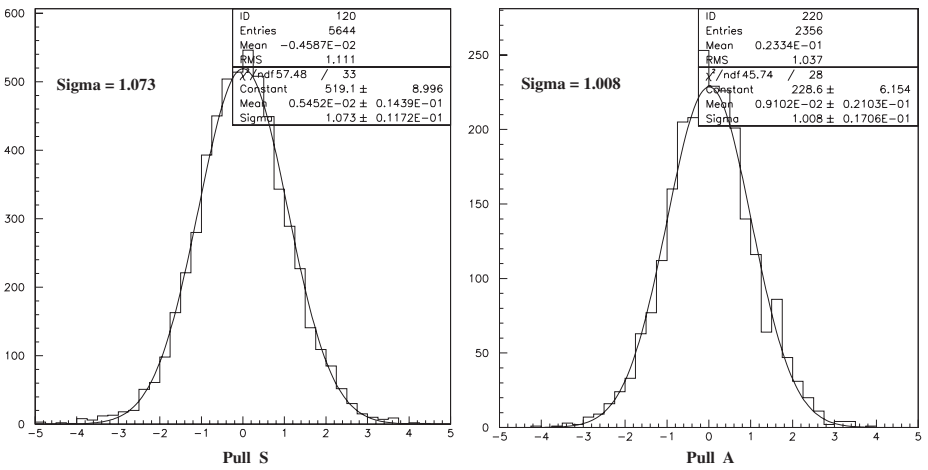

Figure 4.8: *Pull distribution for $\mathcal{S}_{J/\psi\pi^0}$ (left) and $\mathcal{A}_{J/\psi\pi^0}$ (right)*

4.6.3 Goodness of Fit

We calculate the goodness of fit for Δt distribution, which is shown in Figure 4.5, using the following equation [36]:

$$\chi^2 \;=\; 2\sum_i \left((N_i^{\rm th} - N_i^{\rm obs}) + N_i^{\rm obs} \ln \frac{\rm N_i^{obs}}{\rm N_i^{th}} \right)$$

where $N_i^{\rm obs}$ and $N_i^{\rm th}$ are observed and expected contents of i-th bin. We obtain $\chi^2 = 7.69/8$ DOF and 10.9/8 DOF for B^0 tag and $\bar{B}^0$ tag, respectively. These resultant numbers show that our CP fit is converging reasonably well.

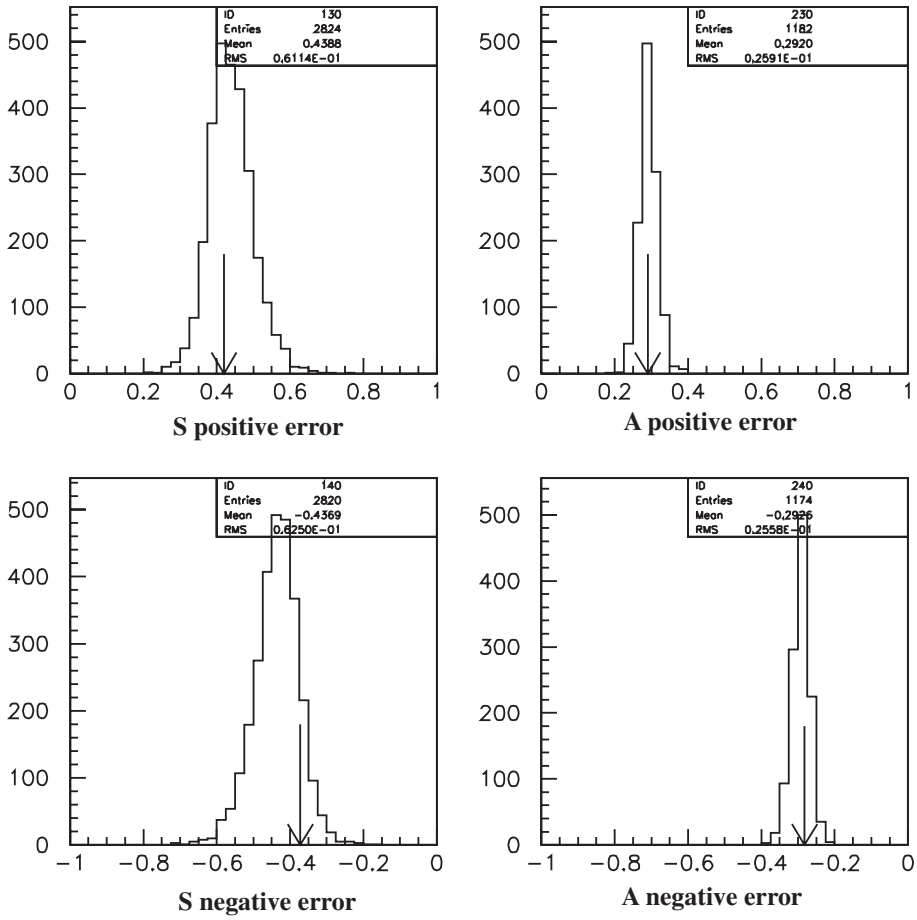

Figure 4.9: *Result of toy Monte carlo for $\mathcal{S}_{J/\psi\pi^0}$(left) and $\mathcal{A}_{J/\psi\pi^0}$(right). Positive error (top) and negative error(bottom) are shown. Each arrow points the MINOS error obtained from data.*

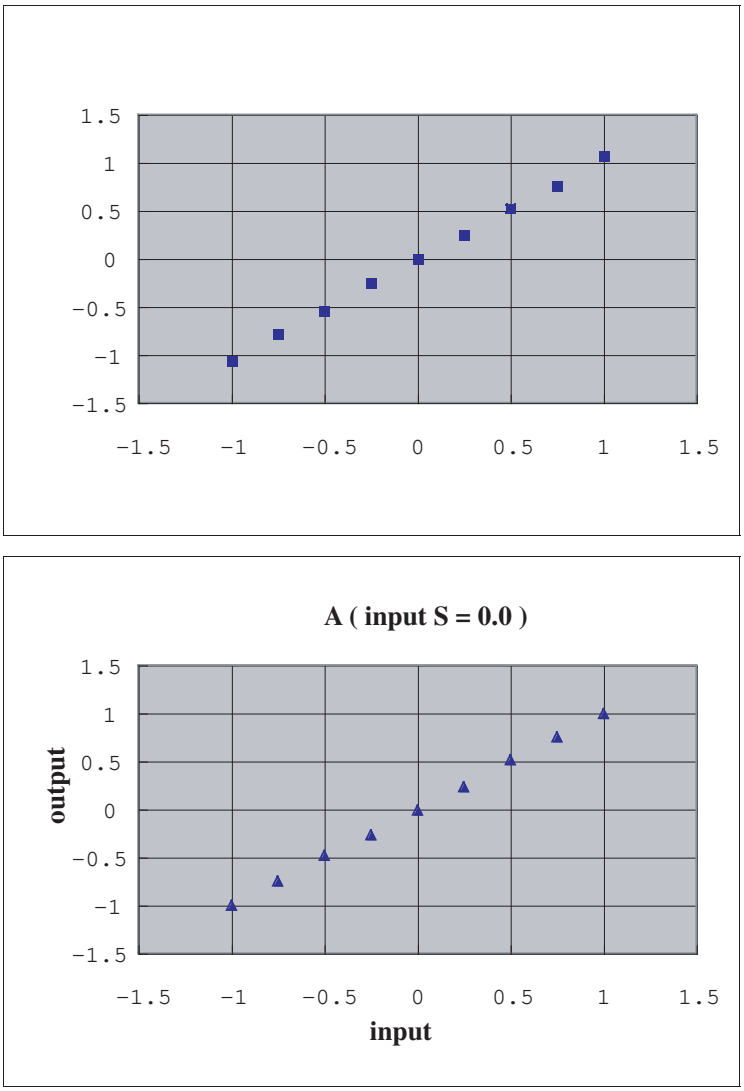

Figure 4.10: *Linearity test : Mean value of fit result vs. each input value for* $\mathcal{S}_{J/\psi\pi^0}$*(top) and* $\mathcal{A}_{J/\psi\pi^0}$*(bottom). we vary input value* $\mathcal{S}_{J/\psi\pi^0}(\mathcal{A}_{J/\psi\pi^0}) =$ { *-1.0, -0.75, -0.5, -0.25, 0.0, 0.25, 0.5, 0.75, 1.0* } *with* $\mathcal{A}_{J/\psi\pi^0}(\mathcal{S}_{J/\psi\pi^0}) = 0$.

Chapter 5

Conclusion

We have performed a measurement of the CP-violating parameters in the $B^0 \to J/\psi\pi^0$ decay based on 140 fb^{-1} data sample accumulated at the $\Upsilon(4S)$ resonance by the Belle detector. The resultant values are

$$\begin{aligned} \mathcal{S}_{J/\psi\pi^0} &= -0.72 \pm 0.42(\text{stat}) \pm 0.09(\text{syst}), \\ \mathcal{A}_{J/\psi\pi^0} &= -0.01 \pm 0.29(\text{stat}) \pm 0.03(\text{syst}). \end{aligned}$$

Figure 5.1 shows the values for $\mathcal{S}_{J/\psi\pi^0}$ and $\mathcal{A}_{J/\psi\pi^0}$ measured by Belle and BaBar experiment. Both of them are consistent each other within their errors. Although statistical error is large, our result is consistent with those obtained for $B^0 \to J/\psi\ K_S$ and other decays governed by $b \to c\bar{c}s$ transition, as expected from the Standard Model if the tree diagram dominates. Figure 5.2 shows the comparison of various measurements of $-\eta_f S_f$, which correspond to $\sin 2\phi_1$ when f is the CP eigenstate induced by $b \to c\bar{c}s$ transition, where η_f and S_f are the CP eigenvalue and the CP-violating parameter being proportional to $\sin \Delta m \Delta t$, respectively, for the final state f.

The measurement presented in this thesis revealed that we will be able to observe a significant CP violation in $b \to c\bar{c}d$ transition in a few years, which will lead to new physics effects.

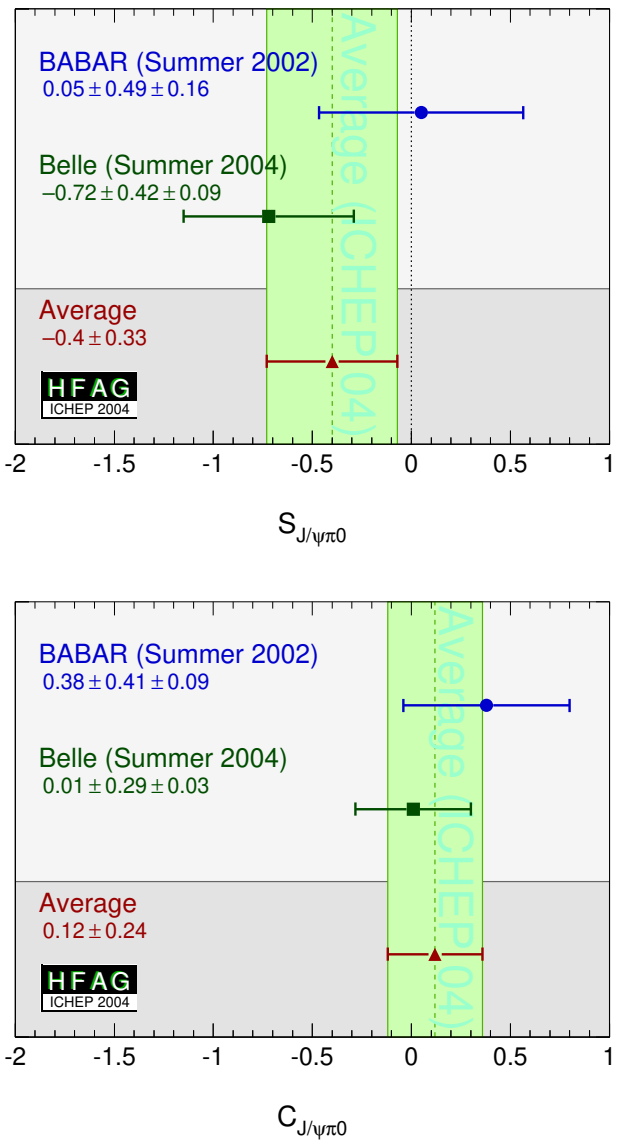

Figure 5.1: *Comparison of the measurements for* $\mathcal{S}_{J/\psi\pi^0}$ *(upper) and* $\mathcal{C}_{J/\psi\pi^0} = -\mathcal{A}_{J/\psi\pi^0}$ *(lower) between Belle and BaBar experiments.*

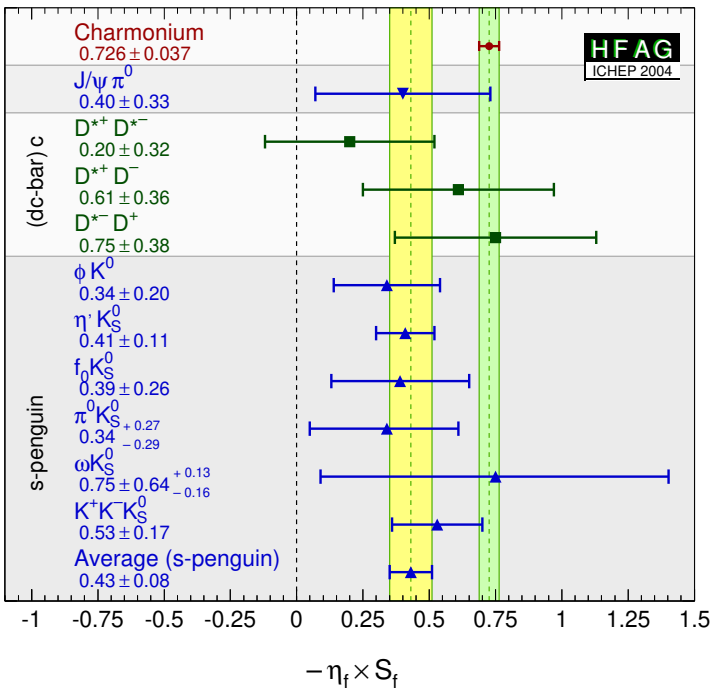

Figure 5.2: *Comparison of the various measurements of* $-\eta_f S_f$*, which corresponds to* $\sin 2\phi_1$ *when* f *is the* CP *eigenstate induced by* $b \to c\bar{c}s$ *transition, where* η_f *and* S_f *are the* CP *eigenvalue and the* CP*-violating parameter being proportional to* $\sin \Delta m \Delta t$*, respectively, for the final state* f*.*

Acknowledgment

First of all, I would like to thank my supervisor, Prof. S. Noguchi, for leading me to the field of high energy physics and his gentle support.

I am deeply thankful to Prof. K. Miyabayashi and Prof. H. Hayashii for thier great support and teaching me the basis of high energy physics.

I wish to express my appreciation to Prof. Y. Sakai, M. Hazumi and all the members of the Belle CP fit group for their help and valuable suggestions. I also would like to thank to Prof. T. Tsukamoto for his support in the work for ECL.

I would like to express my special thanks to Prof. T. Higuchi, Dr. K. Sumisawa and Dr. K. Hara. Without their great help and precious advise, this thesis work wouldn't have finished.

I also wish to thank to the members in our group at the Nara Women's University, Ms. A. Imoto, Ms. N. Kanagawa, Ms. M. Fujita, Ms. C. Hashimoto, Ms. M. Sotokoba and Ms. M. Fujikawa. I enjoyed the life at the university with them.

At last, I am especially indebted to all of my family. I appreciate my parents for giving me the opportunity to receive education. I thank my husband for his great help and support. Without his understanding, I could not finish my work.

Bibliography

[1] L. H. Christenson, J. W. Cronin, V. L. Fitch, and R. Turlay, Phys. Rev. Lett. **13**, 138 (1964).

[2] M. Kobayashi and T. Maskawa, Prog. Theor. Phys. **49**, 652 (1973).

[3] I. I. Bigi and A. I. Sanda, CP Violation, Cambridge University Press (2000).

[4] E.Fernandez *et al.*, Phys. Rev. Lett. **51**, 1022 (1983);
N.Lockyer *et al.*, Phys. Rev. Lett. **51**, 1316 (1983).

[5] H. Albrecht *et al.* (ARGUS Collaboration), Phys. Lett. **51**, 1316 (1983).

[6] S. Kurokawa and E. Kikutani, Nucl. Instr. and. Meth. A **499**, 1 (2003).

[7] A. Abashian *et al.* (Belle Collaboration), Nucl. Instr. and Meth. A **479**, 117 (2002).

[8] K. Abe *et al.* (Belle Collaboration), Phys. Rev. Lett. **87**, 091802 (2001);
K. Abe *et al.* (Belle Collaboration), Phys. Rev. **D66**, 032007 (2002);
K. Abe *et al.* (Belle Collaboration), Phys. Rev. **D66**, 071102(R) (2002).

[9] B. Aubert *et al.* (BaBar Collaboration), Phys. Rev. Lett. **87**, 091801 (2001);
B. Aubert *et al.* (BaBar Collaboration), Phys. Rev. **D66**, 032003 (2002);
B. Aubert *et al.* (BaBar Collaboration), Phys. Rev. Lett. **89**, 201802 (2002).

[10] B. Aubert *et al.* (BaBar Collaboration), Phys. Rev. Lett. **91**, 061802 (2003).

[11] T. D. Lee and C. N. Yang, Phys. Rev. **104**, 254 (1956).

[12] C. S. Wu, E. Amblrt, R. W. Hayward, D. D. Hoppes and R. P. Hudson, Phys. Rev. **105**, 1413 (1957).

[13] R. L. Garwin, L. M. Lederman and M. Weinrich, Phys. Rev. **105**, 1415 (1957).

[14] S. Bennett *et al.*, Phys. Rev. Lett. **19**, 993 (1967).

[15] D. Dorfan *et al.*, Phys. Lett. **19**, 983 (1967).

[16] L. Wolfenstein, Phys. Rev. Lett. **51**, 1945 (1983).

[17] T. Inami and C.S. Lim, Prog. Theor. Phys., **65**,297(1981).

[18] F. Gilman and M. Wise, Phys. Rev. **D27**,1128 (1983).

[19] M. Jamin A. J. Buras and P. H. Weisz, Nucl. Phys. **B347**, 491 (1990).

[20] J. S. Hagelin, Nucl. Phys. **B193**,123 (1981).

[21] Belle publications web page, http://belle.kek.jp/belle/publications.html.

[22] A. Abashian *et al.* (Belle Collaboration), Nucl. Instr. and Meth. **A 479** (2002) 117.

[23] V. Chabaud *et al.*, Nucl. Instr. and Meth. **A368**, 314 (1996).

[24] E. Nygård *et al.*, Nucl. Instr. and Meth. **A301**, 506 (1991).

[25] O. Toker *et al.*, Nucl. Instr. and Meth. **A340**, 572 (1994).

[26] G. Alimonti *et al.*, Nucl. Instr. and Meth. **A453**, 71 (2000).

[27] HBOOK, CERN Program Library Long Writeup Y250 (1993).

[28] QQ event generator, `http://www.lns.cornell.edu/public/CLEO/soft/QQ`.

[29] The EvtGen package home page,`http://hep.ucsb.edu/people/lange/EvtGen/`.

[30] D. J. Lange, Nucl. Instr. and Meth. **A462**, 152 (2001).

[31] R. Itoh, "QQ quick reference for Belle":
`http://belle.kek.jp/~software/qq/html/belle_qq.html` (1996).

[32] GEANT detector Description and Simulation Tool, CERN Program Library Long Writeup W5013 (1993).

[33] R. E. Kalman, Trans. ASME, J. Bas. Eng. **82D**, 35 (1960); R. E. Kalman and R. S. Bucy, Trans. ASME, J. Bas. Eng. **83D**, 95 (1961).

[34] K. Hanagaki *et al.*, Nucl. Instr. and Meth. **A485**, 490 (2002).

[35] A. Abashian *et al.*, Nucl. Instr. and Meth. **A491**, 69 (2002).

[36] S. Eidelman *et al.* (Particle Data Group). Phys. Lett. **B592**, 1 (2004)

[37] Belle Collaboration, Technical Report 1, KEK (1995).

[38] B. Casey, Belle note 296 and 390, unpublished.

[39] G. Fox and S. Wolfram, Phys. Rev. Lett. **41**, 1581 (1978).

[40] The dominant contribution comes from two-body B meson decays including a J/ψ meson, with well-measured branching fractions ($B \to J/\psi K^{(*)}$).

[41] J. Tanaka, Belle note 193 and 194, unpublished.

[42] J. Tanaka, Belle note 517, unpublished;
T. Higuchi, Belle note 307, unpublished.

[43] T. Higuchi, T. Tomura, and H. Tajima, Belle Note 470, unpublished.

[44] H. Tajima *et al.*, hep-ex/0301026 (2003).

[45] F. James and M. Roos, CERN Program Library Long Writeup D506, CERN.

[46] K. Hagiwara *et al.* (Particle Data Group), Phys. Rev. **D66**, 010001 (2002) and 2003 off-year partial update to the 2004 edition.

[47] T. Skwarnicki, Ph.D. Thesis, Institute for Nuclear Physics, Krakow 1986; DESY Internal Report, DESY F31-86-02 (1986).

[48] H. Albrecht *et al.* (ARGUS Collaboration), Phys. Lett. **B241**, 278 (1990).

[49] K. Abe *et al.* (Belle Collaboration), Phys. Rev. Lett. **88**, 171801 (2002).

[50] T. Tomura *et al.* (Belle Collaboration), Phys. Lett. **B542**, 207 (2002).

[51] K. Hara and M. Hazumi *et al.* (Belle Collaboration), Phys. Rev. Lett. **89**, 251803 (2002).